7926015

STEPH, NICK CHARLES
ELECTRON PHOTON ANGULAR CORRELATION MEASUREMENTS OF HELIUM(SINGLET-1S(0) - SINGLET-2P(1)) EXCITATION BY ELECTRON IMPACT AT 80 EV.

THE UNIVERSITY OF OKLAHOMA, PH.D., 1979

University Microfilms International 300 N. ZEEB ROAD, ANN ARBOR, MI 48106

THE UNIVERSITY OF OKLAHOMA

GRADUATE COLLEGE

ELECTRON PHOTON ANGULAR CORRELATION MEASUREMENTS OF $HE(1^1S_0-2^1P_1)$ EXCITATION BY ELECTRON IMPACT AT 80 EV

A DISSERTATION

SUBMITTED TO THE GRADUATE FACULTY

in partial fulfillment of the requirements for the

degree of

DOCTOR OF PHILOSOPHY

By

NICK CHARLES STEPH

NORMAN, OKLAHOMA

1979

ELECTRON PHOTON ANGULAR CORRELATION MEASUREMENTS OF

$HE(1^1S_0 - 2^1P_1)$ EXCITATION BY ELECTRON IMPACT AT 80 eV*

A DISSERTATION

APPROVED FOR THE DEPARTMENT OF PHYSICS AND ASTRONOMY

APPROVED BY

DISSERTATION COMMITTEE

For Linda

my wife and colleague

ACKNOWLEDGEMENT

I wish to express my sincere appreciation to Professor David Golden who suggested this research problem, gave me invaluable direction and taught me the meaning and importance of persistance.

Special thanks are due Professor Stanley Babb, Jr. for his help and support throughout my graduate studies.

The experiment could not have been completed without the excellent machine work and ingenious solutions to design problems provided by Mr. Gene Scott and Mr. Woody Porter. Thanks are also due Dr. Gerry Haddad and Dr. Vic Sutcliffe for their help and advice.

I extend my gratitude to the Department of Physics and Astronomy for financial support during my years of graduate study.

Financial support for this work was provided by grants from the Air Force Office of Scientific Research and the National Science Foundation.

NCS

ELECTRON PHOTON ANGULAR CORRELATION MEASUREMENTS OF

He ($1^1S_0-2^1P_1$) EXCITATION BY ELECTRON IMPACT AT 80 EV

Nick C. Steph

University of Oklahoma

Norman, Oklahoma

1979

MAJOR PROFESSOR: DAVID E. GOLDEN, PH.D.

Abstract

The electron-photon angular correlation function was measured between 80 eV electrons which excited the 2^1P_1 state of helium and 58.4 nm photons from the decay of that state for a range of electron scattering angles from 5° to 100°. The data have been analysed to yield values of the ratio of the differential cross section for exciting the m_J=0 sublevel to the total differential cross section, λ, and the magnitude of the phase difference between the m_J=0 and m_J=1 excitation amplitudes, $|\chi|$. The data agree with all previous measurements within one standard deviation with the exception of the large angle values of λ obtained by Hollywood, Crowe and Williams. The cause of these discrepancies is discussed and they are resolved in favor of the present results. The values of λ obtained in this work agree quite well with those given by the distorted wave calculation of Madison and Calhoun while the values of $|\chi|$ do not agree with any calculations over the entire angular range.

TABLE OF CONTENTS

Page

LIST OF TABLES

LIST OF FIGURES

FIGURE Page

CHAPTER I

INTRODUCTION

The study of the physical processes involving collisions between electrons and atoms has proceeded, via the complimentary approaches of theory and experiment, since the discovery of the electron by J. J. Thomson in 1897.[1] From the experimental results, Thomson proposed his first model of the atom: electrons imbedded in a uniform ball of positive charge.[2] Bolstered by the experimental results of Geiger and Marsden[3] in 1909, Rutherford proposed a nuclear model of the atom in 1911[4] which is the basis of present theories. Experimental investigation of the hydrogen spectra led Bohr[5] in 1913 to postulate the quantization of the electron orbits in Rutherford's atom and the theory of quantum mechanics began to be developed.

The measurement of scattering cross sections, which characterize electron-atom collisions, has been the subject of systematic investigations since the 1920's. The pioneering works of Ramsauer[6] and Brode[7] provided integrated cross sections describing the collisions of electrons with helium and other gases. But, as quantum mechanical calculations improved it became apparent that integrated cross sections did not provide sufficient sensitivity to guide further theoretical refinements. Thus, experimental determinations of differential cross sections, optical excitation functions and polarization of atomic line impact radiation were undertaken and have provided important tests for theoretical models of the scattering process.

The present day study of electron-atom scattering is generally separated into three regions by the energy, E, of the incident electron: The low energy region is $0 < E \leq 100$ eV, the intermediate region is $100 < E \leq 1000$ eV and the high energy region is $E > 1000$ eV. In the low and intermediate energy regions the quantum mechanical principles are usually assumed to be fully understood, but the technical difficulties involved in applying them in full to a complete atomic system have been insurmountable.[8] It is necessary to simplify the atomic system conceptually and develop mathematical approximations. These approximations tend to fail below $\sim$100 eV which is the energy region of most interest in the current study of hot gases such as stellar atmospheres and plasmas. The only method by which we can assess the accuracy of the various approximations is by comparing them with experimental data. The observed phenomena should be a good approximation to the single process usually studied by the theoretician.

Previous experimental work in electron-atom collisions has usually involved averages over significant parameters of the scattering. Differential cross sections do not distinguish the excitations to degenerate sublevels of excited atomic states. Measurements of line polarization separate the contributions of magnetic sublevels but obtain only integral cross sections. Neither measurement allows the relative phase of excitation amplitudes to be deduced. Yet the phases depend in a nontrivial way on the dynamics of the scattering and are related to the transfer of angular momentum to the atom. The measurement of complex excitation amplitudes could provide a new, sensitive test of electron-atom scattering theories, since these are all the quantum mechanical observables.

The experimental method which enables such a measurement is to study the angular correlation between electrons which have excited a particular atomic state and photons from the decay of that state. Correlation between outgoing components of an electron-atom scattering experiment implies coherent excitation of the sublevels of the excited atomic state. The subject of coherent excitation of atomic sublevels began with the beam foil measurements of Bashkin et al.[9] in 1966. These measurements were aimed at the determination of atomic lifetimes by looking at radiation from foils excited by ion impact. The amount of light emitted from an excited atom was measured as a function of time, and from these data lifetimes were extracted. In the absence of external fields, the light intensity was expected to decrease exponentially. However, some zero-field oscillations were seen in the results of Bashkin et al.[9] and also in the later results of Chupp et al.[10] shown in Fig. 1. These oscillations were attributed to Stark mixing due to an electric field in the ion beam itself by Bashkin et al.;[9] while Chupp et al.[10] concluded that the oscillations were due to reflections in their monochromator. The correct explanation, given in 1969 by Macek,[11] is that the oscillations were really beats due to interferences between various fine-structure or hyperfine-structure levels. This hypothesis implies oscillations in the intensity of polarized light but no oscillations would be present in the total emitted intensity. However, in both of these experiments,[9,10] the emitted light was frequency analysed with a grating which selectively reflected certain polarizations. Thus, Macek[11] postulated the coherent excitation of fine and hyperfine levels. This hypothesis was subject to much controversy initially, but it has since been demonstrated experimentally[12] and is now fully accepted.

The first consistent treatment relating the number of photons emitted after an atomic collision to excitation cross sections was given by Percival and Seaton in 1958.[13] They did not consider the detection of scattered particles and photons in coincidence and therefore used a time independent theory with the further condition of incoherent excitation of magnetic substates. In 1971, Macek and Jaecks[14] took the magnetic substates to be coherently excited and developed a time dependent theory and gave expressions for photon-particle coincidences for Ly-α transitions in hydrogen and $^1P \rightarrow {}^1S$ transitions in helium. These expressions relate the anisotropy of the emitted radiation to the complex amplitudes for the coherent excitation of the magnetic substates of the excited levels. The theory was then reformulated by Fano and Macek[15] to stress the interpretation of observed anisotropy in terms of the alignment and orientation of the emitting atoms. Other treatments have been given by Rubin et al.,[16] Wykes,[17] Blum and Kleinpoppen,[18] and Eichler and Fretsch.[19]

The first electron-photon angular correlation measurements reported were for the excitation of the 2^1P state of helium.[20] In these experiments, $2^1P \rightarrow 1^1S$ photons were detected as a function of angle θ_γ in the scattering plane in delayed coincidence with electrons which had excited the 2^1P state and been scattered to various scattering angles θ_e at various electron impact energies E. The wave function of the 2^1P state is completely determined within an arbitrary phase factor by the cross sections for exciting the magnetic sublevels of the 2^1P state, σ_0, $\sigma_1 = \sigma_{-1}$ and the relative phase χ between the corresponding scattering amplitudes. The standard parameters used to describe the scattering are: σ the differential cross section for exciting the 2^1P state ($\sigma = \sigma_0 + 2\sigma_1$), $\lambda = \sigma_0/\sigma$ and χ.

The measurements of Eminyan et al.[20] in 1974 which were the first to determine λ and $|\chi|$ for the 2^1P state of helium, covered the energy range from 40 to 80 eV for a range of θ_e from 16° to 40° and the energy range from 100 to 200 eV for a range of θ_e from 16° to 20°. The angular ranges at 80 eV and 120 eV were extended to 11° and 10° respectively by Ugbabe et al.[21] in 1976. Tan et al.[22] in 1977 used a linear polarization filter at 50 eV to cover the angular range from 5° to 42° and at a fixed scattering angle of 42° to cover the energy range from 32 to 80 eV. Sutcliffe et al.[23] in 1978 extended the measurements of λ at 80 eV to the range from 5° to 155° by restricting the photon detector to 90° and thus no determination of χ was made. All of these experiments are in excellent agreement for λ and $|\chi|$ at 80 eV in their common angular ranges. More recently, Hollywood et al.[24] measured both λ and $|\chi|$ at 80 eV for the angular range 10° to 130°. Their values of λ at 16° and 25° are lower by 9% and 12%, respectively, than those of Eminyan et al.[20] and their results disagree even if the uncertainties are increased to two standard deviations or 95% confidence limits. In the range from 50° to 70° they agree with the results of Sutcliffe et al.,[23] while their values in the range from 80° to 130°

are all substantially lower than the value of Sutcliffe et al.[23] Their values of $|\chi|$ are in good agreement with previous measurements in their common angular ranges.

Since the work of Macek and Jaecks,[14] there have been several calculations of both λ and χ using several different techniques.[25-32] An exposition of the various theoretical approximation methods and references to calculations prior to 1968 may be found in the excellent review article of Moiseiwitsch and Smith.[8]

The distorted wave calculations of Madison and Calhoun[25] give values of λ at 80 eV in excellent agreement with all of the data of Sutcliffe et al.,[23] while another distorted wave calculation by Baluja and McDowell[32] does not agree with any of the data. The recent R-matrix calculation of Fon et al.[31] is in fair agreement with the small angle data for λ at 80 eV, and although somewhat lower than the large angle data of Sutcliffe et al.,[23] it is substantially higher than the large angle results of Hollywood et al.[24]

The only measurements of $|\chi|$ at 80 eV which extend to large values of θ_e are those of Hollywood et al.[24] The R-matrix calculations of Fon et al.[31] and the distorted wave calculations of Scott and McDowell[28] and Baluja and McDowell[32] are the only calculations thus far that give results which resemble the measurements. However none of these calculations are in very good agreement with each other or the measurements of $|\chi|$ over the complete angular range.

CHAPTER II

THEORY

The technique of delayed coicidence in the study of scattering has only recently become widely used in atomic physics.[33] This technique requires a complex theoretical and experimental analysis of the observables. The situation is characterized[34] by the recent works dealing with the theory of the measurement of electron-atom collisions and impact radiation.[14-19,33-37] These works establish relations between observables and theoretical parameters. These theoretical parameters may be roughly divided into three groups: collision parameters of the excitation process, source parameters of the excited atom, and polarization parameters which characterize the angular correlation and momentum transfer. The relation of these parameters to the experimental measurements will be discussed in the three sections of this chapter. Theoretical works which detail approximate calculations of electron-atom collision processes[8,25-32] provide important predictions for comparison with experimental results, but they are seldom concerned with the theory of the measurement and will not be discussed here.

A. Collision Parameters

The fundamental difference between a coincidence measurement and a measurement of the angular distribution of impact radiation is the difference in symmetry. An experiment which measures only the angular distribution of impact radiation has cylindrical symmetry about the incident electron beam. In a coincidence experiment, the incident electron beam and the axis of the electron detector define a scattering plane. The experimental geometry then possesses only reflection symmetry in this plane, rather than rotational symmetry about the incident beam. As a consequence of this lower symmetry, the magnetic substates are coherently excited and interference between excitation amplitudes referring to different magnetic sublevels occurs. The underlying idea is that internal symmetries of the atomic target can be uncovered by properly fixing the external symmetry of an experiment or calculation.[33] The resulting angular ocrrelation between the electrons and photons detected in coincidence indicates a lack of internal independence in the atom.

The theory of Macek and Jaecks[14] relates the number of coincidences measured for a given orientation of electron and photon detectors to the excitation amplitudes describing the formation of the decaying states. The amplitudes are treated as parameters to be fitted to experimental data. The general theory of Macek and Jaecks[14] is applicable to any inelastic scattering event of the form

$$A + B \rightarrow A' + B' + \text{photon}$$

where A represents any target, B represents any incident particle and the primes indicate that the target and/or the particle may undergo changes, such as charge exchange, during the collision. In addition, the photon may be emitted from either A or B with only the restriction that the photons must be emitted by an atom. The theory that follows will be restricted to the specific experiment:

$$e + He(1^1S) \rightarrow e + He(2^1P) \rightarrow e + He(1^1S) + \text{photon} .$$

The standard way to treat the 2^1P state of helium is to describe it by a coherent superpostion of the degenerate magnetic sublevels and neglect spin-orbit and spin-spin interactions in the collision. In addition, the 2^1P state will be excited in a field-free region. The atom is excited into the 2^1P state of helium such that the amplitudes a_{m_J} for magnetic sublevel excitation govern the initial distribution of the sublevel excitation of the eigenstate, $\psi(2^1P_1)$, of the excited atom,

$$\psi(2^1P_1) = \sum_{m_J} a_{m_J} |Jm_J\rangle = a_0|10\rangle + a_1|11\rangle + a_{-1}|1{-1}\rangle . \tag{1}$$

Mirror symmetry of the electron-atom scattering process imposes the restriction that $a_1 = -a_{-1}$. If we take the direction of the incident beam along the z axis and the x-z plane as the scattering plane, the angular parts of the wave function may be written as:

$$\psi_z = |10\rangle , \qquad -\sqrt{2}\,\psi_x = |11\rangle - |1{-1}\rangle . \tag{2}$$

Thus,

$$\psi(2^1P_1) = a_0\psi_z - \sqrt{2}\,a_1\psi_x \tag{3}$$

and

$$\sigma = |a_0|^2 + 2|a_1|^2 = \sigma_0 + 2\sigma_1 \tag{4}$$

where σ is the inelastic differential cross section for excitation of the 2^1P state and σ_0 and σ_1 are the partial differential cross sections for exciting the magnetic sublevels $m_J = 0$ and $m_J = \pm 1$, respectively. The amplitudes a_{m_J} are in general complex numbers. The excitation process is determined by the incident energy, E, and the scattering angle, θ_e, of the inelastically scattered electron. The amplitudes a_0 and a_1 are expected to have a fixed phase relationship. Since the wave function may only be determined up to an arbitrary phase, we take $a_0 = |a_0|$ and $a_1 = |a_1|e^{i\chi}$. Thus $\psi(2^1P_1)$ at a given E and θ_e is completely described within an arbitrary phase factor by σ_0, σ_1 and χ.

The equation given by Macek and Jaecks[14] relating these parameters to $\dot{N}_c$, the rate at which coincidences are detected, is

$$\begin{aligned} d\dot{N}_c = vn_0n_A \frac{\gamma'}{\gamma} \frac{3}{8\pi}\Big\{&\lambda\sin^2\theta_\gamma + \left(\frac{1-\lambda}{2}\right)(\cos^2\theta_\gamma + 1) \\ &- \left(\frac{1-\lambda}{2}\right)\sin^2\theta_\gamma\cos 2(\phi_e-\phi_\gamma) + [\lambda(1-\lambda)]^{\frac{1}{2}}\cos\chi\sin 2\theta_\gamma\cos(\phi_e-\phi_\gamma) \\ &d\Omega_e d\Omega_\gamma\Big\} \end{aligned} \tag{5}$$

where v is the velocity of the incident particles, n_0 is the number density of incident particles, n_A is the number density of target atoms, γ'/γ is the branching ratio for the observed transition, $d\Omega_e$ and $d\Omega_\gamma$ are the differential solid angles subtended by the electron and photon detectors, respectively, and the angles θ_e, ϕ_e, θ_γ and ϕ_γ refer to the detector geometry in the collision frame as shown in Fig. 2. (Note that the implicit dependence on E and θ_e is in λ and χ.)

When the photon detector is constrained to be in the scattering plane such that $\phi_\gamma = 0$ while $\phi_e = \pi$, Eq. (5) can be rewritten as:

$$\frac{d\dot{N}_c}{d\Omega_e d\Omega_\gamma} = \frac{3}{8\pi}\frac{I_e}{e}\rho(z)\frac{\gamma'}{\gamma}\varepsilon_e\varepsilon_\gamma \sigma f(\lambda,\chi,\theta_\gamma) \tag{6}$$

where I_e is the incident electron current, e is the electron charge, $\rho(z)$ is the density of helium atoms in the interaction volume, ε_e and ε_γ are the efficiencies of the electron and photon detectors, respectively, Macek and Jaecks[14] assumed ideal detectors in Eq. (5) , and

$$f(\lambda,\chi,\theta_\gamma) = \lambda\sin^2\theta_\gamma + (1-\lambda)\cos^2\theta_\gamma - \sqrt{\lambda(1-\lambda)}\cos\chi\sin 2\theta_\gamma \tag{7}$$

is the angular correlation function.

B. Source Parameters

The excitation of an atom by collision generally leaves it in an anisotropic state which can be characterized by the expectation values of orbital angular momentum. These expectation values (in units of $\hbar$) can be related to the collision parameters λ and χ as shown by Kleinpoppen,[34]

$$\begin{aligned} \langle J_x\rangle &= 0 & \langle J_x^2\rangle &= \lambda \\ \langle J_y\rangle &= -2\sqrt{\lambda(1-\lambda)}\sin\chi & \langle J_y^2\rangle &= 1 \\ \langle J_z\rangle &= 0 & \langle J_z^2\rangle &= 1-\lambda \end{aligned} \tag{8}$$

where the reference frame is the collision frame shown in Fig. 2, and $\vec{J}^2 = J_x^2 + J_y^2 + J_z^2 = J(J+1) = 2$ for the 2^1P_1 state of helium. Usually the source parameters are given as an orientation vector, $\vec{O}$, whose components are proportional to the average angular momentum of the source atom, and an alignment tensor, $\overleftrightarrow{A}$, whose components are proportional to the mean values of quadratic expressions in J_x, J_y, J_z and $\vec{J}$. Expressions for the nonvanishing components of $\vec{O}$ and $\overleftrightarrow{A}$ were originally developed by Fano and Macek[15] in 1973. In 1978, Morgan and McDowell[37] pointed out that some confusion had arisen in the literature due to misprints and differing choices of reference frames. They rederive expressions for $\vec{O}$ and $\overleftrightarrow{A}$ and correct several errors in the literature (including references 15, 20, 34 and 38).

The nonvanishing components of $\vec{O}$ and $\overleftrightarrow{A}$ in the collision frame given by Morgan and McDowell[37] are:

$$O_{-1}^{col} = \frac{\langle J_y \rangle}{J(J+1)} = -[\lambda(1-\lambda)]^{\frac{1}{2}}\sin\chi \tag{9}$$

$$A_0^{col} = \frac{\langle 3J_z^2 - \vec{J}^2 \rangle}{J(J+1)} = \frac{(1-3\lambda)}{2} \tag{10}$$

$$A_{1+}^{col} = \frac{\langle J_x^2 - J_y^2 \rangle}{J(J+1)} = [\lambda(1-\lambda)]^{\frac{1}{2}}\cos\chi \tag{11}$$

$$A_{2+}^{col} = \frac{\langle J_xJ_z + J_zJ_x \rangle}{J(J+1)} = \frac{(\lambda-1)}{2} \tag{12}$$

where the subscripts denote transformation properties (see Ref. 15). Using these source parameters one can rewrite the angular correlation function, Eq. (7), as

$$f(\lambda,\chi,\theta_\gamma) = \frac{2}{3} + \frac{1}{2} A_0^{col}(3\cos^2\theta_\gamma - 1) - A_{1+}^{col}\sin 2\theta_\gamma + A_{2+}^{col}\sin^2\theta_\gamma \tag{13}$$

C. Polarization Parameters

The anisotropy of the excited atom is manifested in the impact radiation through its angular distribution and polarization. The radiation from the de-excitation process $^1P \rightarrow {}^1S$ has polarized components which are proportional to the moduli squared of the excitation amplitudes of $\psi(2^1P_1)$ given in Eq. (3). The intensities of emission linearly polarized along the x, y, or z directions are thus

$$I_x \propto 2|a_1|^2 \, , \quad I_y = 0 \, , \quad I_z \propto |a_0|^2 \quad . \tag{14}$$

With these intensities, the Stokes parameters may be calculated. These parameters (S_0,S_1,S_2,S_3) have been extensively discussed in the literature.[38,39] When normalized to the total intensity S_0, the remaining three Stokes parameters are associated with the linear and circular polarization as follows:

$$\begin{aligned} S_1 &= I(0^\circ) - I(90^\circ) \\ S_2 &= I(45^\circ) - I(135^\circ) \\ S_3 &= I(RHC) - I(LHC) \end{aligned} \tag{15}$$

where RHC and LHC denote right and left hand circular polarizations, respectively and the angles are referenced to the axes which define the plane perpendicular to the direction of emission.

The normalized parameters S_1, S_2 and S_3 may be regarded as the components of a three dimensional vector polarization $\vec{P}$, which has the magnitude $|\vec{P}| = (S_1^2 + S_2^2 + S_3^2)^{\frac{1}{2}}$ where $0 \leq |\vec{P}| \leq 1$. When $|\vec{P}| = 1$, the radiation is completely polarized; thus $|\vec{P}|$ is referred to as the degree of polarization. An additional parameter which characterizes the state of the coincidence radiation is the correlation factor μ,[38]

$$\mu = \frac{S_2 - iS_3}{(1 - S_1^2)^{\frac{1}{2}}} \tag{16}$$

The modulus, $|\mu|$, is called the degree of coherence between the linearly polarized orthogonal components of the radiation. It can be shown that $|\mu| \leq |\vec{P}| \leq 1.$[39] The significance of a degree of coherence and a degree of polarization equal to unity is that this can occur if and only if every detected photon is in the same polarization state.

For radiation emitted in the scattering plane along the z-axis the normalized components of $\vec{P}$ are,[40]

$$S_1^z = \frac{I_z - I_y}{I_x + I_y} = \frac{2|a_1|^2}{2|a_1|^2} = 1 \tag{17a}$$

$$S_2^z = \frac{2I_xI_y}{I_x + I_y} \cos\chi = 0 \tag{17b}$$

$$S_3^z = \frac{-2I_xI_y}{I_x + I_y} \sin\chi = 0 \tag{17c}$$

where the superscripts on S_1, S_2 and S_3 indicate the axis along which the radiation is viewed. For radiation emitted along the x-axis,

$$S_1^x = \frac{I_z - I_y}{I_z + I_y} = \frac{|a_0|^2}{|a_0|^2} = 1 \tag{18a}$$

$$S_2^x = S_3^x = 0 \tag{18b}$$

and for radiation emitted perpendicular to the scattering plane,

$$S_1^y = \frac{I_z - I_x}{I_z + I_x} = \frac{|a_0|^2 - 2|a_1|^2}{|a_0|^2 + 2|a_1|^2} = 2\lambda - 1 \tag{19a}$$

$$S_2^y = \frac{I_z I_x}{I_z + I_x}\cos\chi = \frac{2|a_0|^2|a_1|^2}{|a_0|^2 + 2|a_1|^2}\cos\chi = 2[\lambda(1-\lambda)]^{\frac{1}{2}}\cos\chi \quad (19b)$$

$$S_3^y = -\frac{2I_z I_x}{I_z + I_x}\sin\chi = \frac{2|a_0|^2|a_1|^2}{|a_o|^2 + 2|a_1|^2}\sin\chi = -2[\lambda(1-\lambda)]^{\frac{1}{2}}\sin\chi \quad (19c)$$

As seen from Eqs. (17) and (18), the radiation observed in the scattering plane is 100% linearly polarized parallel to the scattering plane while circular polarization vanishes. The absence of circular polarization within the scattering plane is equivalent to the fact that orbital angular momentum transfer only occurs along the y-axis.[34] In the literature, the parameter S_1^y is usually referred to as the linear polarization and is given the symbol P_{1in}, and S_3^y is referred to as the circular polarization and is given the symbol P_{circ}. Comparing Eq. (19c) with Eq. (9), it is seen that $P_{circ} = 2\ O_{-1}^{col}$. Comparing Eq. (19b) with Eq. (11), it is seen that $S_2^y = 2A_{1+}^{col}$. The results of Eqs. (17)-(19) predict that $|\vec{P}| = |\mu| = 1$ for ${}^1P \rightarrow {}^1S$ transitions. This was shown to be true, within experimental error, by Standage and Kleinpoppen.[38] The appearance of χ in Eq. (19) represents the fundamental result that a quantum mechanical phase between two excitation amplitudes appears as a directly observable phase between two observable radiation vectors. This result was also first demonstrated by Standage and Kleinpoppen[38] and considered in some detail theoretically by Kleinpoppen.[36]

The results of this chapter may be related to a simple physical picture of the production of impact radiation. Macek and Jaecks[14] show that the angular distribution of the radiation can be described by constructing a classical source with the angular distribution given by Eq. (7). One such source is two dipoles d_z and d_x aligned along the z and x axes, respectively, with amplitudes $d_z = |a_0|$ and $d_x = \sqrt{2}\,|a_1|$, and with a relative phase of χ. An equivalent source that is somewhat more revealing is obtained by rotating this pair of dipoles through an angle α so that they lie along the axes z' and x' where $z' = z\cos\alpha + x\sin\alpha$ and $x' = -z\sin\alpha + x\sin\alpha$. These dipoles have amplitudes $d_{z'} = |a_0\cos\alpha + \sqrt{2}\,a_1\sin\alpha|$ and $d_{x'} = |a_0\sin\alpha - \sqrt{2}\,a_1\sin\alpha|$. The angle α is chosen such that the radiation from the dipoles $d_{x'}$ and $d_{z'}$ differ in phase by 90°:

$$\tan 2\alpha = \frac{2\sqrt{2}\ \mathrm{Re}(a_0 a_1^*)}{|a_0|^2 - 2|a_1|^2} \tag{20}$$

When α has the value specified by Eq. (20) it is called θ_{min} because it is the angle where the angular correlation function has its minimum value. Written in terms of λ and χ the value of θ_{min} is specified by

$$\tan 2\theta_{min} = \frac{2[\lambda(1-\lambda)]^{\frac{1}{2}}}{2\lambda-1}\cos\chi \quad . \tag{21}$$

This formulation of the $^1P\rightarrow{}^1S$ transition was of great interest in the initial measurements, since experimental results could be readily compared with the predictions of the Born approximation. In the Born approximation, $\chi \equiv 0$ everywhere so that $d_{z'}^{Born}$ is $|a_0|$, $d_{x'}^{Born}$ is zero and θ_{min}^{Born} equals θ_k, the direction of momentum transfer. The experimental results have since shown the Born approximation to have only limited validity; but this formulation remains a useful picture and values of θ_{min} are usually included in the results of calculations and experiments. A detailed discussion of the Born approximation is given in Macek and Jaecks,[14] and a comparison to experimental results is given by Eminyan et al.[20]

One final parameter of interest is the polarization fraction, $\mathcal{P}$. This parameter is used to characterize impact radiation observed without regard to scattered electrons. The angular distribution of impact radiation in terms of $\mathcal{P}$ is given by

$$I(\theta_\gamma) = I(90^\circ)(1 - \mathcal{P}\cos^2\theta_\gamma) \tag{22}$$

where I is the intensity of radiation in any plane containing the incident beam. However, this parameter is difficult to measure for the 2^1P state of helium due to cascades from higher lying ^1S and ^1D states. These cascades alter the angular distribution of the radiation since they populate the 2^1P state incoherently. For this reason it is of interest that $\mathcal{P}$ can be calculated from the values of λ and σ. The polarization fraction can be defined in terms of the intensities, $I_{||}$ and $I_\perp$, of radiation polarized parallel and perpendicular to the incident beam axis,

$$= \frac{I_{||} - I_\perp}{I_{||} + I_\perp} . \tag{23}$$

Equivalently, $\mathcal{P}$ may be defined in terms of the integrated partial cross sections Q_{m_J}, where

$$Q_{m_J} = \int_{4\pi} |a_{m_J}|^2 d\Omega_e \tag{24}$$

and, in terms of λ and σ,

$$Q_0 = \int_{4\pi} \lambda\sigma d\Omega_e , \quad Q_1 = \int_{4\pi} \frac{(1-\lambda)}{2} \sigma d\Omega_e \tag{25}$$

$\wp$ is then given by

$$\wp = \frac{\mathcal{Q}_0 - \mathcal{Q}_1}{\mathcal{Q}_0 + \mathcal{Q}_1} \tag{26}$$

and $\wp$ can be determined free of cascade effects.

CHAPTER III

APPARATUS

The experimental apparatus, shown schematically in Fig. 3, is a highly versatile electron impact spectrometer. It is capable of the measurement of electron-atom cross sections in the energy range $15 \leq E \leq 1500$ eV and the measurement of impact radiation in the scattering plane for wavelengths $\lesssim 150$ nm. The interaction region is formed by crossed electron and atomic beams. The apparatus consists of a rotatable electron gun (EG), a double walled Faraday cup (FC), a rotatable hemispherical electron energy analyser (EEA), a fixed photon detector (PD), an atomic beam source, electrostatic and magnetic shielding, and a quadrupole mass spectrometer for residual gas analysis. These components are contained within an ultra-high vacuum system capable of a base pressure $< 1 \times 10^{-8}$ Torr. These components as well as the gas handling system, the construction materials, power distribution, and the cleaning, alignment and bake out procedures are discussed in the following sections. The associated electronics will be discussed, in detail, in Chapter IV. The apparatus is basically that described by Sutcliffe,[42] although the components have been redesigned to varying extents for the present experiment. A complete description of the experimental apparatus is given in the present work even though there is some duplication of the work of Sutcliffe.[42]

A. Electron Gun

The EG has four distinct parts: (1) the source region, (2) the beam forming optics, (3) the output optics and (4) the rotation mechanism. A schematic diagram of the EG including the electrical operation is shown in Fig. 4.

The AC power for the EG lenses is floated at the cathode common by a high voltage isolation transformer. This technique allows the operation of the lens elements to be independent of the beam energy defined by the cathode voltage. The EG physical dimensions and a typical set of operating voltages are given in Table I.

1. Source Region

The EG uses an indirectly heated triple-oxide-coated cathode in a Pierce configuration. The source region is designed for a cathode operated in a fully space charge limited condition and a convergent beam in the anode-cathode region. The angle of the Pierce element was chosen to be 58.5° in order to produce a 3° convergent beam emerging from the anode aperture. The independent control of the Pierce element voltage provides control of the electrode potential to adjust for variation in the physical position of the cathode surface. This is important because it is difficult, if not impossible, to center the cathode emitting surface in the Pierce element.

The cathode activation process which reduces the oxide coating and allows the migration of the electron emitter to the surface of the cathode is normally accomplished in about three hours. The filament power supply is operated in a constant current mode and the anode-cathode potential is set at 5 volts to reduce ion bombardment of the cathode emitting surface. It was found in the present work that setting the filament current at 0.1 Amp for a period of 12 hours prior to activation drove off much of the water from the oxide coating. When this was done, the activation power was reduced from $\sim$4.8 watts to $\sim$4.0 watts.

The activation is accomplished by increasing the filament current in steps of about 0.05 Amp at 10 to 15 minute intervals. A typical activation schedule is given in Table II. During activation, the background pressure is monitored and care is taken that it does not exceed 0.5 μTorr. Activation is accompanied by a sharp decrease in background pressure and the emission of electrons detected by monitoring the current to the anode. The filament power is then increased by $\sim$25% for $\sim$15 minutes to ensure that the oxide coating is completely reduced. The filament power is then reduced to its activation value and the anode-cathode voltage is increased to 100 volts. At this time the anode current is typically 8 to 10 mAmp and the gun is left in this configuration for 24 hours to stabilize electrically and thermally.

2. Beam Forming Optics

The beam forming optics are comprised of the Pierce, anode, 2, 3 and 4 elements which provide three focusing regions (A-2, 2-3, 3-4). The anode aperture defines the beam diameter and another aperture is placed in the field free region of the 2 element to remove divergent electrons without further limiting the beam diameter. The three focusing regions provide flexibility in the control of the object size and position for the output optics.

3. Output Optics

The output optics are comprised of the 4, 5, 6 and 7 elements, the snout and the quadrupole steering lens. The optics were designed to provide a beam at the scattering center with an energy independent focus for a moderate range of output energies. Minor misalignment of the beam can be compensated by an electrostatic quadrupole steering lens which contains two independent sets of elements (top right-bottom left and top left-bottom right). These sets are contained within the 4 element. The elements of a set operate at the same voltage but different polarities. The mean potential of a set is referenced to the 4 element so that the center line potential through the 4 element is constant. All the lens voltages are fixed relative to the cathode, with the exception of the 7 element and snout, which are grounded.

The snout is designed with a fixed front aperture and a replaceable rear aperture which define the maximum possible angular divergence of the beam. Since the design object of the source region is a 3° convergent beam, the apertures were designed to geometrically limit the output divergence to 3°.

4. Electron Gun Operation

Since no energy selection is used in the EG, the full Maxwellian energy distribution characterized by the cathode temperature and space charge is delivered to the interaction region. The width of the energy distribution varies directly with the anode extraction voltage. With the cathode temperature set at its activation value, the energy distribution of the electron beam increases from about 150 meV full-width-half-maximum (FWHM) to about 250 meV FWHM as the anode extraction voltage is increased from 5 to 50 volts. Since the energy resolution width is not critical in the present work (see Chapter VII) the anode extraction voltage was used to control the amount of current delivered to the scattering center. For extraction voltages in the range from 5 to 50 eV usable beam currents of from 1 to 20 μA were achieved.

The design of the EG snout greatly simplified the tuning of the EG lenses. Sutcliffe[42] found that it was possible to tune his EG such that the electron beam angular profile was asymmetric or had very broad wings and secondary maxima. This problem was assumed to be due to electrons bouncing down the tube lenses and affecting the angular profile of the primary beam. This problem was completely eliminated in the present work by decreasing the diameter of the snout apertures from 2.5 mm to 1.27 mm. In addition, the inner diameter of the snout itself was increased so that electrons that still manage to bounce through the first aperture have a greater probability of being collected by the snout. With these changes, the full angular spread of the beam was consistently 2.8° (1.2° FWHM). The measurement of the electron beam angular profile is detailed in Sec. III.B.5 and a typical beam profile is shown in Fig. 6b.

5. Energy Calibration

The electrons which exit the gun snout have an energy E_G [$E_G = e(V_C - IR)$ where V_C is the cathode common voltage and IR represents the potential drop across the cathode surface]. The value of IR can be determined by measuring a physical process which occurs at a well defined energy. In helium, the 2^2S resonance at 19.35 ± 0.02 eV[43] is the usual calibration point and has been used here. The value of

IR for the cathode used in the present work was found to be 2.32 ± 0.3 volts. Consequently, the measurements of electron scattering at 80 eV, the cathode common voltage was held to 82.32 volts.

6. Rotation Mechanism

The frame of the EG is bolted to the copper baseplate. An aluminum gear wheel is bolted to the underside of this baseplate. The gear wheel has teeth on its inner diameter which engage the gear of a Varian 1-to-1 direct drive feed through rotation mechanism. The base plate rotates on ¼" diameter ceramic balls held in vee grooves cut in the gear wheel and in an aluminum plate beneath it. A race is provided to ensure that the ceramic balls remain equally spaced for easy rotation. The angular position of the electron gun is determined to within 0.1° by a vernier scale on the edge of the copper base plate visible through a window in the vacuum wall.

B. Electron Energy Analyser

The EEA has five distinct parts: (1) the input optics, (2) the injection optics, (3) the energy dispersing element, (4) the detector and (5) the rotation mechanism. A schematic diagram of the EEA including the electrical operation is shown in Fig. 5. In an arrangement identical to the EG operation, the AC power for the EEA elements is floated at the analyser common by a high voltage isolation transformer. The EEA physical dimensions and a typical set of operating voltages are given in Table III.

1. Input Optics

The input optics are formed by a four element lens system (7, 6, 5 and 4) which is identical to the output optics of the EG. A snout designed with a fixed front aperture and a replaceable rear aperture is attached to the 7 element. These apertures geometrically limit the angular divergence of electrons entering the focusing electrodes. This point is discussed further in Sec. III.B.5.

2. Injection Optics

The injection optics are formed by the 4, R and SR elements which decelerate the electrons and focus them onto the entrance aperture of the radial electrostatic field of the hemispheres. An electrostatic quadrupole steering lens is included in the 4 element and is identical in operation and purpose to that in the EG 4 element. The action of the two lenses (4-R and R-SR) provide additional flexibility in the location and size of the image at the entrance plane of the energy dispersing spheres.

3. Energy Analyser and Energy Resolution

The energy analysis is accomplished with a Herzog corrected 180° hemispherical dispersing element with a mean radius of r, (r = 5.08 cm). The input and output apertures are held within the field free region of the sphere reference electrode. A detailed analysis of the hemispherical analyser and a derivation of its resolution can be found in the work of Sutcliffe,[42] and only the results are given here.

The sphere reference electrode is held at a potential V_{SR} which defines the mean energy of the transmitted electrons, E_S ($E_S = e\, V_{SR}$)

and sets the potential along the mean radius of the analyser. The $1/r^2$ field is generated in the analyser by holding the outer sphere to the potential V_{OS},

$$V_{OS} = V_{SR} \frac{r_{IS}}{r_{OS}} \tag{27a}$$

and holding the inner sphere to the potential V_{IS},

$$V_{IS} = V_{SR} \frac{r_{OS}}{r_{IS}} \tag{27b}$$

where r_{OS} and r_{IS} are the radii of the outer and inner spheres, respectively. The full base resolution, $\Delta^B E_S$, for an ideal hemispherical analyser with input and output apertures of equal diameter, $2\Delta r$, is given by

$$\Delta^B E_S = E_S(2 \frac{\Delta r}{r} + \alpha^2) \tag{28}$$

where α is the maximum divergence angle for electrons emerging through the spheres input aperture. Read et al.[44] have developed an expression for the FWHM energy resolution, ΔE_S, which takes into account the dependence on the type of analyser, the type of defining aperture and the ratio of α to $\Delta r/r$, and for this EEA, the expression is:

$$\Delta E_S = 2E_S(0.81 \frac{\Delta r}{r} + 0.25\ \alpha^2)\ . \tag{29}$$

Using the values of $\alpha = 3°$ and $\Delta r = 0.501$ mm which describe the EEA, the design resolution is $\Delta E_S = (0.0174) \cdot E_S$ FWHM. A discussion of the measured resolution is given in Sec. V.A.4.

4. Electron Detector.

The energy selected electrons are collected by a Galileo type 4039 continuous dynode channel electron multiplier (CEM), which is mounted in a grounded housing. The operation of the detector requires one lead to carry the high voltage to the rear end of the CEM and another lead to ground the front end of the CEM. The pulse output of the CEM is carried on the high voltage lead. Both leads are carried within the vacuum chamber as coax cables compatible with ultra-high vacuum operation. The shielded leads are made with #24 gauge copper wire for the center conductor, ceramic fish spine beads for the insulator and braided shield stripped from commercial RG-8 cable. The characteristic impedance of the vacuum coax is calculated to be 46 ohms. Since all signal lines use RG-58 A/U coax cable (50 ohm impedance), an attempt was made to match impedances as closely as possible. Several different configurations of vacuum coax were tested and the most important properties were found to be: 1) The copper braid of the coaxial shield should be sufficiently dense to properly shield the center conductor (i.e., when the braided shield is pulled tightly onto the beads, there should be no gaps where the beads can be clearly seen). 2) The shield should be continuous and unbroken along the entire length of the vacuum coax. Even relatively minor breaks can lead to "feathers" of copper braid which can give intermittent shorts. The shield was terminated at both ends by crimping it with copper wire into a special slotted bead. This copper wire was then connected to the system ground.

The detection efficiency of the CEM is rated by the manufacturer as >90%, for incident electrons with energies less than 1 KeV. The electron gain begins to fall off from its maximum value of 10^8 when the count rate exceeds 10^4 sec^{-1}. This point is discussed further in Sec. V. The operating voltage is 2800 volts, and the dark counts at 23° C are <0.5 sec^{-1}.

5. Angular Calibration and Angular Resolution.

The design of the EEA snout greatly simplified the determination of the angular resolution, $\Delta\theta_e$, of the EEA. The standard method of determining $\Delta\theta_e$ is to measure the angular profile of the electron beam with EEA lenses grounded. The result is then compared with the angular profile measured with the lenses at their operating potential. A discussion of this method is included in the work of Sutcliffe, along with the results for his energy analyser. In this work, the diameters of the EEA snout apertures were decreased from 2.36 mm to 1.33 mm. Measurements of the electron beam profile with the lens elements grounded and with the lens elements at their operating voltages are shown in Figs. 6a and 6b respectively. Although the magnitudes of the detected currents differ by a factor of ~1000, the angular profiles are virtually identical. There is a small change in the position of the center of the profile due to the effect of the electrostatic quadrupole steering lens. These measurements show that the EEA acceptance profile is determined solely by geometry. Thus, $\Delta\theta_e$ is determined by the diameter of the rear snout aperture and its distance from the collision center. The EEA lenses serve only to focus the electrons emerging from the EEA snout rear aperture onto the input aperture of the spheres.

6. EEA Operation.

The EEA operation is determined by the sphere reference potential, V_{SR}. After V_{SR} is chosen, the analyser common voltage, V_A, is set equal to the cathode common voltage, V_C. Then, the lens voltages and the voltage difference between the inner and outer hemispheres, V_{IO}, are adjusted for maximum transmission. Of course the elastically scattered electrons that are detected have the energy E_G $[E_G = e(V_C - IR)]$ as discussed in Sec. III.A.5. Therefore the "true" mean energy of the transmitted electrons is $\bar{E}$ $[\bar{E} = e(V_{SR} - IR)]$. In the present work V_{SR} is held to 20.0 volts, and therefore $\bar{E} = 17.68$ volts.

The electrons to be detected are then chosen by the energy they have lost, ΔE, by adjusting the EEA common voltage V_A until it differs from the EG cathode common voltage V_C by ΔE $[\Delta E = e(V_C - V_A)]$. This arrangement allows the operation of the EEA lens elements and energy dispersing element to be independent of ΔE. Thus, an energy loss spectrum may be obtained by simply inserting a staircase ramp generator in the positive side of the analyser common power supply. For measurements at fixed ΔE, the positive side of the analyser common is grounded.

The lens voltages typically have a 2 to 5 mVolt, 60 Hz component. High frequency traps are inserted in the lines carrying DC voltage for the sphere reference (SR), inner sphere (IS) and outer sphere (OS) elements. The traps eliminate high frequency spikes.

7. Rotation Mechanism.

The frame of the EEA rests of 1/8" sapphire balls contained in two concentric grooves cut into the copper base plate. Since it was not possible to include a race to keep the sapphire balls in position, the copper base plate was adjusted to be as level as possible. In addition, rotation of the EEA was effected very carefully so that the sapphire balls would not be pushed or rolled out from under the EEA. The rotation center is a beryllium-copper post supported by the frame of the EG. The details of the alignment of this post are discussed in Sec. III.L. The EEA frame has a removable arm which slides over the rotation center post and screws into the EEA frame. The EEA is aligned with this arm by three off-line pins. At the rotation center a dog clutch is attached to the arm and engages an identical dog clutch connected to the rotary motion feed through of a Varian model 1365 harmonic drive. A 1/16" copper plate in the shape of a torus is screwed to the top of the EEA frame. The angular position of the EEA is determined within $\pm 0.1^\circ$ by a vernier scale inscribed on the copper plate and visible through a window in the vacuum wall.

C. Photon Detector

The vacuum ultra-violet (VUV) photons are detected with a CEM identical to that used in the EEA. The CEM is mounted in a cylindrical grounded copper housing equipped with a snout with a fixed aperture. The physical dimensions of the PD are given in Table IV. Three grids made from 80% transparent copper mesh are mounted in the PD housing in front of the CEM. The first grid is grounded to prevent electrostatic field penetration into the scattering region. The second grid is held at -200 volts to prevent electrons and negative ions from being detected. The third grid is held to 20 volts to prevent positive ions from being detected. Experimental tests were made to determine the efficacy of these grids. The negative grid was absolutely necessary;

while the positive grid voltage did not measurably affect the PD count rate. This indicates that any positive ions formed in the collision have insufficient energy to create pulses in the CEM. This would seem to be the case since the manufacturer does not give efficiencies for ion detection below 1 KeV. In addition, tests were made to ensure that the voltages on the second and third grids did not affect the electron count rate. This was found to be the case for all values of θ_e.

The snout aperture and the face of the CEM are the limiting apertures defining the viewing geometry of the PD. The diameter of the snout aperture was chosen such that the entire detector face can be seen from the collision center. Thus, the angular resolution of the PD, $\Delta\theta_\gamma$, is determined by the diameter of the CEM face and its distance from the collision center.

The electrical operation of the CEM in the PD is identical to that described in Sec. III.B.4. The VUV photons from the helium $2^1P \rightarrow 1^1S$ transition have a wavelength of 58.4 nm. The detection efficiency for 58.4 nm photons is rated at $\sim$15% by the manufacturer. This efficiency falls logarithmically to 0.1% for 150 nm photons so that the CEM provides discrimination against photons with wavelengths $\gtrsim$150 nm.

The PD is supported in the scattering plane by a frame with a C-clamp that is attached to the differential pumping manifold described in Sec. III.E. Thus, the PD was held in a fixed position and the photon emission angle, θ_γ, was determined by rotating the EG.

D. Faraday Cup.

The unscattered electrons are collected by a double-walled Faraday cup. A schematic diagram of the FC is given in Fig. 7. The outer wall is grounded and its aperture diameter is 9.525 mm. This insures that the full beam enters the cup, even for low beam energies where space charge spreading is greatest. The inner cup is insulated and its aperture diameter is 12.7 mm. Thus the full beam also enters the FC inner cup.

The maximization of the collection efficiency (see for example, Kuyatt[45]) is accomplished by the geometry of the FC, given the limitations of space and materials. The main problem is the emission of secondary electrons from copper, which has been discussed by Kuyatt[45] and Myers.[46] The ratio of secondary emission to incident primaries for 80 eV electrons at normal incidence to a copper surface is ∿0.5. The energy distribution of the secondaries is such that ∿7% are elastically scattered primaries, ∿3% are inelastically scattered primaries with energies between 10 and 80 eV, and ∿90% are "true" secondaries with energies of ∿10 eV. The secondary electrons are emitted from the surface in a cosine distribution relative to the surface normal and suffer additional collisions with the FC walls. As the energy of the electrons decreases from 10 to 5 eV the secondary emission ratio for copper decreases from 0.2 to 0.07. For a further decrease in primary energy the ratio remains constant at ∿0.065, but at energies below ∿1 eV, the ratio increases slightly, indicating a value of 0.1 as the primary energy approaches zero.[45]

With these facts in mind the FC was designed to maximize the collection efficiency. The cup was made as deep as possible and the solid angle subtended by the entrance aperture at the collecting surface is 1.5×10^{-2} sr. In order to direct the cosine distribution of the secondaries away from the entrance aperture, a target, which is inclined at 50°, is placed at the back of the cup. Although the secondary yield increases with a decrease in the angle of incidence, the secondary flux over the entrance aperture is reduced by ∿30%.[41] Finally, the FC is designed so that the collecting surface area is 100 times greater than the aperture area. Thus, an average electron would require 100 collisions before exiting the FC; and the collection efficiency of the FC is estimated to be >0.98. The currents from the FC inner wall and target are connected in parallel to a current integrating ammeter.

The FC is bolted to a rotation table which is captured between two plates and rides on 1/8" sapphire balls held in vee grooves. When scattering angles of less than 25° are studied, the FC is displaced by the EEA. A spring lever returns the FC to its stable position when the EEA is returned to angles greater than 25°.

E. Atomic Beam Source.

The atomic beam source is shown schematically in Fig. 8b. The atomic beam is generated by a single capillary with an inside diameter of 0.51 mm and an aspect ratio, R_A, of 100 (R_A = length/diameter). The capillary is silver-soldered into a 1/4" copper tube which delivers the gas. The capillary is held in place by two bushings within a copper differential pumping manifold (DPM). The capillary is positioned at the center of the DPM and 1 mm below a 0.50 mm aperture in the top of the DPM. This aperture serves as a differentially pumped skimmer which reduces the wings of the beam profile of the gas which effuses through the capillary. The edges of the skimmer were sharpened to reduce the number of gas atoms which scatter from the edges towards the scattering plane which would increase the wings of the beam profile. Measurements by Naumov[47] have shown that the angular width, $\Delta\theta_B$, of the directivity pattern of a capillary with aspect ratio R_A is given by

$$\Delta\theta_B = 2\cot^{-1}(R_A) \tag{30}$$

For the present work, $\Delta\theta_B = 1.14°$. Thus, the combination of a large aspect ratio and differential skimming is expected to produce a beam of target atoms $\sim$0.51 mm in diameter in the scattering plane which is 5 mm above the skimmer. The density of the gas beam is determined experimentally and is discussed in Sec. VII.A.

F. Gas Handling System.

The gas handling system is shown schematically in Fig. 8a. High purity (99.995%) helium from a high pressure cylinder is introduced via a regulator and a Granville Phillips variable leak valve. Three bellows-operated metal sealed gate valves (GV) are present to direct gas flow. During a coincidence experiment GV#1 is open and GV#2 and GV#3 are closed. A high pressure ionization gauge is provided to measure the capillary driving pressure. GV#1 can be closed to isolate the ultra-high vacuum system from the variable leak valve. GV#2 can be opened to provide a bypass line to pump out the tubulation of the gas handling system. GV#3 can be opened to flood the chamber with helium.

G. Electrostatic and Magnetic Shielding.

The EG and EEA were each provided with integral grounded shields made from sheets of copper 0.04" thick. The shields were bent into proper shape and screwed directly to the grounded frames of the EG and EEA. Although the PD housing was grounded, another copper shield was provided to insure that fields from the CEM high voltage connection could not be seen from the interaction region. Care was taken that all leads were shielded from the interaction region. This was simple for the PD, which does not move, and for the EEA where the leads are behind the integral shield and follow the rotation arm to the rotation center. These leads do not move with respect to the EEA. The leads to the rotating EG presented more of a problem. This was solved by inserting the EG leads into a 0.75" diameter copper tube 9" long. This tube was attached at one end to a universal pivot joint on the EG frame and the other end was fed through a 1" diameter hole in the magnetic shield. As the EG was rotated with respect to the hole, the copper tube slid in and out of the hole. The leads were made long enough to accommodate this motion. The leads to the FC moved when the FC rotated and they were shielded accordingly.

The EG, EEA, PD, FC, atomic beam source and copper base plate are all contained within a magnetic shield. The magnetic shield is contained within the vacuum system and is constructed of 1 mm thick molypermalloy. It is formed into a cylinder 16" in diameter and 9" in height. It is closed with top and bottom caps which are tightly fitted onto the cylinder.

The magnetic shield is penetrated by several holes to facilitate the leads, the rotation gears, and to allow efficient pumping. In all cases these holes are positioned more than two hole diameters away from the electron beam and all detected electron trajectories. The magnetic shield was degaussed with a toroidal coil with a mean diameter of 61 cm containing 100 turns of #14 gauge copper wire. After degaussing, the maximum field strength in the interaction region was <8 mG measured with a Rawson-Lush rotating coil Gauss meter.

H. Vacuum System.

The vacuum chamber and associated pumps are shown in Fig. 9. The ultra-high vacuum chamber is constructed entirely of 300 series stainless steel and is bakable to 250° C. All demountable members are tungsten-inert-gas welded (TIG). All welds are inside, where physically possible. The electrical vacuum feed throughs are Ceramaseal MHV type connectors which are TIG welded into demountable flanges.

The main chamber is a 23 cm high collar with a 43 cm inside diameter. The collar has four access ports (P1 - P4) positioned 90° apart and equipped with 23 cm standard ASA flanges. These ports are allocated as follows: P1 contains the EG and FC leads; P2 contains the PD leads; P3 connects the main chamber to a diffusion pump; and P4 contains the residual gas analyser.

Three types of metal gaskets are used to seal the demountable flanges. The top and bottom flanges of the main chamber collar and the access ports P1 - P4 are sealed with an aluminum wire gasket. These gaskets are made from #20 gauge dead soft aluminum wire. A wire of sufficient length is cut and cleaned (see Sec. III.J). The center of the wire is then twisted in a pigtail fashion to create an "ear" about 3" long. The wire is then positioned on the sealing surface and the ear taped down, away from the sealing surface, to hold the wire in place. The wire is then shaped into a circle to conform with the sealing surface and the free ends are twisted to create another ear which is taped to hold the completed gasket in place. To complete a successful seal, care must be taken to apply uniform torque to the bolts holding the mating flanges; and a strict order of rotation between bolts must be used. This ensures that torque is applied uniformly about the entire circumference of the mating flanges. The top flange was the most difficult to seal and the method is given here in detail. The 24 bolts are numbered sequentially and the torque is applied in the rotation order of 1-13-7-19-4-16-10-22 etc. The torque is applied in 6 steps: 10, 20, 25, 30, 35 and 40 ft-lbs. The order of rotation is then reversed and 43 ft-lbs is applied. Because the top flange is so large, aluminum shims with a thickness just less than the combined height of the raised sealing surfaces are placed between every third pair of bolts. This keeps the flange from warping and helps to keep the torque uniform. When this procedure was followed, a good seal was always achieved.

The flange which holds the rotary feed through of the harmonic drive has a very narrow sealing surface. Therefore, aluminum foil is used to make this gasket. The foil is stretched tightly across the sealing surface and the edges of the foil are crimped around the edge of the flange to keep the foil in place. An Exacto knife is used to cut out the center of the foil leaving a smooth layer of foil on the sealing surface. The mating flange is carefully positioned and torqued on as described earlier. All other flanges use conventional knife-edge sealed copper gaskets, and a good seal is easily obtained. The chamber pressure is measured with a Varian nude ionization gauge mounted on the top flange.

Two Varian VHS-4 expanded oil diffusion pumps are used to evacuate the system. One of them pumps the main chamber through an elbow, and the other is used to differentially pump the atomic beam source. The exhausts of the two diffusion pumps are pumped in parallel by a Sargent-Welch 1397 mechanical rotary pump. A foreline valve is located between the mechanical pump and the diffusion pumps, which is electrically operated in parallel with the mechanical pump. When power to the mechanical pump is shut off, the valve seals the diffusion pump exhausts and opens the mechanical pump to the atmosphere.

The foreline pressure is measured with a thermocouple gauge. The gauge is connected to a Varian model #810 thermocouple controller. The controller contains an adjustable set point, optically activated meter relay. The meter relay is used to interlock the diffusion pump operation to an adjustable preset maximum foreline pressure. If the preset maximum foreline pressure is exceeded, the power to the diffusion pump is shut off and the quick cool water lines are opened to cool the diffusion pump heaters.

Sorbent traps are located between the chamber and each diffusion pump to eliminate both backstreaming and creep of oil from the pumps into the chamber. The trap interior consists of a center basket and a wall liner constructed of stainless steel mesh. This mesh holds the sorbent material. The center basket forms an optically dense baffle which provides the major protection against backstreaming oil. The wall liner restricts the creep of oil. The sorbent material (Zeolite) is a molecular sieve with a pore diameter of $\sim$10 Å. The throughput of the traps is $\sim$50%.

I. Power Distribution.

The power distribution is shown schematically in Fig. 10. Two separate three-phase high-leg power lines are committed to the experiment. Each of these lines can carry 60 Amps of three phase current. One three phase power line is committed to the vacuum system pumps and the other is committed to the electronics.

The voltage between two of the three possible pairs of legs is 120 volts. The voltage between the remaining pair is 200 volts and requires a step down transformer. Nevertheless, all the lines are taken through transformers to provide isolation from the power line common ground. Additional isolation transformers are used in the line supplying power to the electrodes and the line supplying power to the electronics rack. Each of the power lines leaving the transformers carries 120 volts at 60 Hz. The allocation of these lines and their maximum current capacities and fusing are shown in Fig. 10 and will not be discussed here.

If a power outage occurs, the quick cool lines to the diffusion pump heaters are opened and the relay in the power line to the main power supply rack is opened. When the power is returned, the quick cool lines are closed automatically when the foreline pressure falls below its preset point as discussed in Sec. III.H. The relay in the main power supply must be reset manually.

This system has suffered power outages for periods ranging from $\sim$1 sec to $\sim$1 hour After a long power outage (>30 min) the cathode suffers about a 10% decrease in emission current. Otherwise, no ill effects have occurred due to power outages.

J. Construction Materials and Cleaning Procedures.

The choice of materials was determined by four criteria: 1) The material must be compatible with an ultra-high vacuum system including the bake-out procedure. 2) The material must not contain any material poisonous to the cathode emitting surface. 3) All material used within the magnetic shield must be non-magnetic. 4) Any material which holds a surface charge must be shielded from the interaction region. The first criterion requires the exclusive use of metal seals. The second criterion excludes the use of brass and requires all solder joints to be silver-soldered. The third criterion excludes the use of stainless steel inside the magnetic shield. The fourth criterion limits the use of insulators and aluminum (which oxidizes readily).

All four criteria must be adhered to within the magnetic shield. All threaded stock was locally fabricated from beryllium-copper alloy. All tapped holes are relieved with bleed holes or slotted screws to provide pumping channels. The replaceable apertures are fabricated from 0.13 mm thick molybdenum sheet. Aluminum has been used for gear wheels beneath the base plate. All other metal components have been fabricated from oxygen-free-high-conductivity (OFHC) copper.

All components within the vacuum system must be carefully cleaned. The purpose of cleaning is threefold. Contaminants which could poison the cathode must be removed. Volatile contaminants, particularly body oils, are difficult, if not impossible, to remove by baking and pumping. They must be removed by cleaning to ensure that an ultra-high vacuum can be obtained. All copper parts, particularly those forming tube lenses and electromagnetic shields, must have bare metal surfaces. This ensures that they are good conductors.

The cleaning procedure for OFHC copper and beryllium copper alloy has evolved from that given by Sutcliffe.[42] The procedure involves eight steps: 1) Degrease in acetone if needed. 2) Clean in a formic acid bath composed of: 300 ml formic acid (88%), 500 ml hydrogen peroxide (33%) and 600 ml distilled water. The purpose of this bath is to etch the surface of the copper down to bare metal. If a piece is exceptionally dirty, it is useful to remove it from the bath after a few minutes and scrub it, under running water, to remove foreign material. The piece may be rinsed in distilled water and returned to the formic acid bath. Normal pieces require only 10 to 20 minutes in the bath. 3) Rinse by dipping and swirling in a bath of distilled water. 4) Clean off formic acid in a bath composed of 600 ml hydrochloric acid (38%) in 6000 ml distilled water. It is important to thoroughly remove the formic acid before continuing. If a piece has tapped holes or small crevices, it is useful to swirl the piece in the acid. The piece usually requires only 5 to 10 minutes in this bath, but it can be left in the bath for periods up to one hour without adverse effects. 5) Rinse in distilled water to remove hydrochloric acid. 6) Rinse in a bath of reagent grade acetone. The acetone container is placed in an ultrasonic vibrator to aid in cleaning. 7) Rinse in a second bath of reagent grade acetone. 8) Remove from the last acetone bath and blow dry immediately with a heat gun. When possible, the clean copper is placed immediately in a vacuum system and pumped down. In practice, the copper can be stored for several days in a clean covered container.

The molybdenum apertures, machinable glass and alumina were cleaned in a bath of 10% hydrochloric acid. The pieces were scrubbed when necessary. They were left in the bath for periods of 10 min. to 1 hr. depending on how dirty they were. The pieces were then rinsed as described in steps 5 - 8 above. All aluminum parts were cleaned by scrubbing with acetone and rinsing with clean acetone.

K. Bakeout Procedure.

When the vacuum system is initially sealed, pump down is initiated by roughing the vessel through the diffusion pumps with the mechanical pump. When the foreline pressure falls below 0.1 Torr, the diffusion pumps are turned on and a pressure of $\sim 6 \times 10^{-5}$ Torr is achieved. Depending on how long the system has been exposed to the atmosphere, this pump down is achieved in from 1 to 12 hours. In order to lower the pressure further, it is necessary to bake the system to drive off water and other gases traped in the walls and the molecular sieve material. Heating tapes are used and power is supplied through variacs so the temperature change can be controlled. Since the system does not include valves between the chamber and the sorbent traps, the bake out is accomplished by slowly heating the main chamber first and then slowly heating the traps. The voltage to the heaters is increased until the wall temperature reaches $\sim 250^\circ$ C. When the temperature exceeds 250° C, one or more of the aluminum gaskets usually fails. For a system opened to air for more than one day, ~ 24 hrs. are required to reach 250° C. The heating must be done slowly so that the foreline pressure does not exceed ~ 0.2 Torr. The system is left at 250° C for 2 to 3 days and the system pumps down to ~ 5 μTorr. When this pressure is reached, the sorbent trap heaters are turned off slowly over a period of ~ 2 hrs. The system is then left overnight so the sorbent traps may cool completely. The pressure at this time is $\sim 10^{-7}$ Torr and the chamber heaters are turned off slowly. After about six hours the pressure will be down to 3.0×10^{-8} Torr and cathode activation, as discussed in Sec. III.B.1, may begin.

L. Mechanical Alignment Procedure.

The EG and rotation center are aligned first. The post which defines the rotation center for the EEA is bolted loosely to the EG frame and the EG frame is bolted loosely to the base plate. A 0.5 mm aperture is mechanically centered in the rotation center post. A He-Ne laser beam is directed onto the aperture and the result is a spot of light on the differential pumping manifold. The rotation center post is then moved around until the spot of light coincides with the 0.5 mm skimmer aperture. At the same time the axis of the EG is aligned with this rotation axis. The EG snout is removed and a precision ground carbon steel rod is inserted into the bore of the gun until it contacts the aperture in the 2 element. This rod is equipped with a needle-tipped cap. The EG is moved about until the needle-tip intersects the beam of light connecting the rotation center to the skimmer aperture. When this is accomplished, the EG and rotation center post are bolted tightly into position.

The FC is aligned next. Minor height adjustment is accomplished with copper shims between the FC and its rotation table. The FC is held at 0° with respect to the EG axis by an adjustable stop. The 0° position is determined by an alignment collar which fits on the end of the precision ground rod that is inserted in the EG bore. This collar fits into the FC when it is at 0° and the stop is set.

The EEA is put into place next. The arm which connects the EEA to the rotation center aligns the EEA mechanically as discussed in Sec. II.B.7. This alignment is checked by means of another needle-tipped cap and precision ground rod which is inserted into the bore of the EEA. The two needle tips should touch at the axis of rotation for all angular positions of the EEA and EG. This criterion is satisfied within about ± 0.2 mm through the entire combined angular ranges. This is excellent alignment considering the amount of machining involved.

Finally the PD is aligned. Minor height adjustment is made by sliding the C-clamp of the PD frame up or down the differential pumping manifold. The angular position is then determined. The alignment is purely mechanical and is accomplished by setting the EEA directly opposite the PD and fitting the top of the precision ground rod from the EEA into an alignment collar which fits into the PD aperture.

The EG is then rotated until its precision ground rod is placed perpendicular to the rod of the EEA. The perpendicularity is determined with a block of aluminum machined to a right angle. The angular position of the EG is then noted on its scale and this reading calibrates teh scale which determines θ_γ. When the alignment is complete, the rods and collars are removed and the snouts replaced. The system is then ready to be sealed.

CHAPTER IV

ELECTRONICS

A coincidence experiment with time resolution of ~ 1 nsec requires state-of-the-art electronics. Care must be taken to ensure that the electronics do not bias the data and alter the experimental results. Experimental checks must be developed to understand any systematic effects of the electronics, and any random effects must be minimized.

A. Power Supplies

The cathode common and analyser common power supplies are Hewlett Packard model 6209B operated in constant voltage mode. The load and line regulation is <0.02% and ripple is <1 mvolt rms. The total drift for 24 hours is <0.02%. The output is variable, 0 to 320 volts at 0.1 Amp.

The EG and EEA electrode power supplies are Kepco model PCX 100-0.2(C) operated in constant voltage mode. The load and line regulation is <0.01% and ripple is <5 mvolt rms. The total drift for 24 hours is <0.01%. The output is variable, 0 to 100 volts at 0.2 Amp. Each of the outputs of these power supplies is connected to a pair of ten-turn potentiometers (pots) for coarse and fine voltage control. These pots are arranged in pairs on the system control panel, and marked with the number of the electrode they control.

The filament power supply is a Kepco model JQE25-4(M) operated in constant current mode. The load and line regulation is <0.01% and ripple is <0.02% rms. The drift for 24 hours is 0.01%. The output is variable, 0 to 4 Amps.

The CEM high voltage power supplies are Canberra model 3002. The load and line regulation is <0.01% and ripple is <10 mvolt peak to peak. The drift for 24 hours is <0.01%. The regulated high voltage output is 0 to 3000 volts DC with 0 to 10 mAmp output current capability.

The digital electronic components are mounted in an auxiliary rack containing three Ortec model 401A modular system bins. Each bin is supplied with power by an Ortec model 402A power supply.

B. Pressure Measurement

The experiment is equipped with two Varian ionization gauges. These gauges are controlled by a Varian dual range control unit, model 971-1008. The Varian MilliTorr nude ionization gauge in the gas handling system indicates pressure in the range from 1 to 10^{-6} Torr. The low pressure gauge located in the top flange is a Varian model UHV-24 double filament nude gauge. The emission current is 15 μAmp for the milliTorr gauge and 4 mAmp for the UHV gauge. Both gauges are degassed by electron bombardment. The pressure is read from the meter in the control unit to an accuracy of ∿2%. All pressures given in this work have implied uncertainties of 2%.

C. Current Measurement

The current from the FC is detected by an Elcor model A308C current indicator capable of the measurement of currents in the range from 10^{-9}

to 10^{-4} Amp. The current is read from a meter to an accuracy of ∿1%. All currents given in this work have implied uncertainties of 1%. The current can be integrated for greater accuracy, if desired. The integration can also be used to provide logic pulses based on the time required to detect a given total amount of charge. The use of these pulses is discussed in Sec. IV.E.

D. Coincidence Circuit

The electron and photon pulses are AC coupled out of the CEMs as shown in Fig. 11. The negative pulses are ∿5 meV deep and ∿20 nsec FWHM. They form the input to the coincidence circuit shown schematically in Fig. 11. The pulses are fed into Ortec model 454 timing filter amplifiers (TFA) through 50Ω terminated inputs. The gain of the TFA is ∿x150. The amplified pulses are fed into Ortec model 473 constant fraction discriminators (CFD). The CFDs were used in both constant fraction and leading edge modes. These two modes given different timing resolutions, as discussed in Sec. IV.F. The outputs of a CFD are a NIM-standard fast, negative logic pulse and a NIM-standard slow, positive logic pulse. The slow, positive pulses from the electron and photon channels are connected to Ortec model 449 log/lin ratemeters. The electron count rate, R_e, and the photon count rate, R_γ, are read from these meters with 1% accuracy. All rates given in this work have implied uncertainties of 1% unless otherwise noted. The fast, negative pulses are fed into the start and stop inputs of an Ortec model 467 time-to-amplitude converter (TAC). The electron signal is used to start the TAC. Since the scattered electrons require ∿130 nsec to travel to the CEM, the photon pulses must be delayed. The fast, negative pulses from the photon channel are passed through a 250 nsec cable delay and are used to stop the TAC. Thus, if a true coincidence is detected, the photon should stop the TAC ∿130 nsec after the electron has started it. The time range of the TAC is set at 1000 nsec and the output pulses range in amplitude from 0 to 10 volts as a linear function of the start to stop time. The TAC output is fed to an Ortec model 6240A 1024 channel multichannel analyser (MCA) operated as a pulse height analyser (PHA). The amplitudes of the pulses from the TAC are converted to a coincidence time spectrum by the PHA. The true coincidences fall into a group of about 20 channels of the MCA corresponding to a range of delays Δt. This time resolution is discussed in Sec. IV.F.

Since the TAC is started on the "slow" event and stopped on the delayed "fast" event, the result is often referred to as an inverted time spectrum. This procedure can prevent both the loss of data due to TAC dead time effects and systematic error in N_c. This is a count rate dependent error and is in fact the most serious systematic effect in the experiment. This subject is discussed in detail in Sec. VII.B.

Each CFD provides an additional, separately generated, fast, negative logic pulse. These pulses are used with an additional TAC-MCA pair to produce a coincidence time spectrum utilizing photon starts and electron stops. This result is usually referred to as a direct time spectrum. The direct spectrum served as a consistency check on the electronics. This subject is discussed in Sec. VII.B.

The true start output of the TAC started by electrons is connected to an Ortec model 775 counter. This records the number of electron true starts, N_e, which is used to normalize the data as discussed in Sec. VI.B.

E. Energy Loss Circuit

It is necessary to obtain an energy loss spectrum to accurately determine the position of the 2^1P state on the system energy scale. The energy loss circuit is shown schematically in Fig. 12.

Pulses from the electron channel CFD are connected to the MCA operated as a multichannel scalar (MCS). The output of the current integrator is used to step the channel advance in the MCS. This integration accounts for small variations in the EG current which would affect the results. The channel-advance-out-pulse from the MCS is used to step the ramp voltage output of an Ortec model 487 spectrum scanner (SS). The ramp voltage is inserted in the positive side of the analyser common power supply. The initial energy loss is set by the start level of the SS and the range of the energy loss spectrum is set by the span of the SS. The spectrum can be cycled through the chosen range in 16, 32, 64, 128 or 1024 steps. The choice depends on the size of the energy range and the energy resolution desired.

F. Timing Calibration

The calibration of a TAC-PHA pair is accomplished with an Ortec model 462 time calibrator (TC). The TC generates logic signals at precise time intervals. These signals are fed into the start and stop inputs of the TAC and a time spectrum is generated in the PHA. The spectrum is a series of peaks ∿1 channel wide. The linearity of the TAC-PHA pair is established if the number of channels between these peaks is constant. These tests showed that the TAC-PHA pairs were linear in the range from channel 50 to channel 1024. Thus, the cable delay was made sufficiently long so that the coincidence peak would occur in the linear range. The time represented by one channel in the PHA is determined by dividing the period of the TC stop signals by the number of channels between peaks in the PHA spectrum. The result is the number of nanoseconds per channel, t_c (t_c = 0.976 nsec/channel).

The time resolution of the electronics is determined by attenuating the logic pulses of the TC and feeding them into the coincidence circuit. The FWHM of the peaks in the PHA spectrum then determines the time uncertainty of the electronics, Δt. When the CFDs are set in the constant fraction or in the leading edge mode, Δt is $\sim$2 nsec. However, this result is only valid for the uniform pulses provided by the TC. The FWHM of a measured coincidence peak obtained with the CFDs in the constant fraction mode is typically $\sim$8 nsec. When the CFD is operated in leading edge mode, the FWHM is typically $\sim$11.5 nsec. The change in the FWHM accurately gauges the improved time resolution of constant fraction discrimination. The increase of the FWHM from 2 nsec to 8 nsec is due to two contributions: 1) The electrons travel through the EEA in a variety of trajectories and their velocity varies with the lens voltages. Assuming the average energy of an electron in the EEA is 30 eV, the average electron's velocity is $\sim$3.2 mm/nsec. The shortest path from the collision center to the CEM is $\sim$270 mm, so possible trajectories need vary by only $\sim$5% to impose a $\sim$4.2 nsec uncertainty. 2) The size of the pulses from the CEMs varies from $\sim$6 meV to $\sim$3 meV. This variation leads to added time uncertainty in the CFD even when operated in the constant fraction mode.

One serious problem is encountered when using the constant fraction mode. There is some ringing present in the coincidence time spectrum.

This ringing becomes particularly large for high count rates and can make the data analysis difficult or impossible in some cases. Therefore the data presented in this work were taken in the leading edge mode. However, the experiment does not attempt to measure lifetimes or any parameters that are time dependent, so the time resolution is not a crucial consideration. As a precaution, some data was taken in the constant fraction mode and analysed. The results agreed within their uncertainties and this ensured that the leading edge operation did not affect the data.

CHAPTER V

DATA ACQUISITION

Before data is taken, it is necessary to check several experimental variables to ensure that the measurement is done properly. The procedure for data acquisition is followed rigorously to ensure that each measurement is made under well known conditions. Since a large volume of raw data is produced, effective means were developed to transfer and store this data for later analysis.

A. Experimental Alignment

Mechanical alignment, while necessary, is insufficient to completely align the experimental components. The flexibility in the operation of these components requires further alignment procedures after their performance has been maximized. Furthermore, theoretical calculations of resolution, based on design parameters, are seldom accurate; and the actual resolution must be determined experimentally where possible.

1. Alignment of the electron beam

After the cathode activation process is complete, the EG may be tuned to provide the desired electron beam. The electrode voltages given in Table I reflect the characteristics of a particular cathode. Different values will be found each time the cathode is changed. In addition, these voltages must be changed significantly if the cathode voltage is changed. Since each voltage affects two lenses, the trial and error technique is tedious; but it remains the only viable method of tuning the EG.

Once a stable beam has been achieved, the current is adjusted to the value required by the measurement being done. This choice is discussed in Sec. V.B. The electrostatic quadrupole steering lenses in the EG and the EEA are referred to as gun legs and analyser legs, respectively. The gun legs are used to maximize the current to the FC. This aligns the electron beam with the atomic beam axis. This alignment is checked by measuring the count rates R_e and R_γ of the electron and photon detectors, respectively, as the leg voltages are varied. When R_e and R_γ are maximized simultaneously, the electron beam is aligned. In practice, both of these methods give virtually identical results.

2. Alignment of electron scattering angle

The analyser legs are used to maximize R_e. As was pointed out in Sec. III.B.5, the analyser legs can alter the effective angular position of the EEA. To eliminate any uncertainty about the angular position of the EEA, the electron beam profile is checked prior to each individual measurement to determine the position of 0°.

3. Photon emission angle

The accurate determination of θ_γ is of particular importance in this experiment. The mechanical alignment, discussed in Sec. III.L, is accurate to $\sim\pm 3°$. This alignment is checked by measuring the total distribution of photons in the scattering plane, $I(\theta_\gamma)$. This distribution is given by Eq. (22). The position of the maximum of this distribution determines $\theta_\gamma = 90$ in this experiment to <1 . (The value of $\wp$ derived from this measurement was 0.42±0.08, which is in agreement with previous measurements.[53]) If the results of this measurement differ significantly from the results of mechanical alignment, it indicates that the mechanical alignment was not done correctly. In this experiment the results differed by $\sim 2°$.

4. Energy resolution

The energy resolution of the experiment is determined by measuring the FWHM of the elastic scattering peak Γ_e using the energy loss circuit. For this experiment Γ_e = 400 meV. The energy resolution of the EEA may be determined using the relation

$$\Gamma_e^2 = \Gamma_s^2 + \Gamma_A^2 \tag{30}$$

where Γ_s is the FWHM of the electron beam and Γ_A is the FWHM of the EEA. Using the value of Γ_s = 250 meV from Sec. III.A.4, the value of Γ_A is $\sim$312 meV. The design resolution of the EEA, calculated from Eq. (29) with $\bar{E}$ substituted for E_s, as discussed in Sec. III.B.6, is $\sim$307 meV. This good agreement indicates that the analyser tuning for maximum transmission is nearly identical to the tuning for maximum resolution.

B. Procedure

The rates R_e and R_γ vary directly with the product, IP, of current and pressure. In order to maintain high gain in the CEMs, neither R_e nor R_γ is allowed to exceed $\sim 3\times10^4$ counts/sec. This may require the adjustment of either current or pressure, to lower one or both of the rates for small electron scattering angles.

After the current and pressure are set, this procedure is followed: 1) Turn off the high voltage to the electron detector. 2) Rotate the electron gun to the desired value of θ_γ and lock the rotation mechanism. 3) Connect the inner sphere to the electrometer and rotate the EEA through the electron beam. Check the beam width and determine the scale position 0°. 4) Reconnect the inner sphere to its power supply and rotate the EEA to the desired value of θ_e. 5) Turn on the electron detector high voltage. 6) Check that the cathode voltage is −(80 + IR) volts. 7) Run an energy loss spectrum. This is usually done from 19 eV to 22 eV in steps of 30 meV. Typical energy loss spectra are shown in Fig. 13. 8) Calculate the position of the 2^1P peak and set ΔE accordingly. If the analyser is tuned correctly, ΔE will be ∿21.22 eV. 9) Record the values of the experimental parameters (current, pressure, R_e, R_γ, θ_e, θ_γ and the scale position of 0°) in the experiment log. 10) To start the data run, start the MCA and counter simultaneously for the inverted coincidence spectrum. 11) The data accumulation time T will vary from several hours to several days, depending on the product R_eR_γ and the level of counting statistics desired. Check the values of the experimental parameters periodically during the run, and note any changes in the experiment log. 12) The run may be interrupted prior to completion if desired. This is useful to check the position of the coincidence peak and determine, approximately, the size of the counting error. The MCA and counter must be stopped and started again simultaneously. 13) When the desired level of statistics is achieved, the run is stopped and the coincidence data is stored as discussed in the next section. The value of N_e is read from the counter and written in the experiment log. 14) When all the data are stored and their retrieval checked, the data in the MCA and counter are erased. 15) The experiment can now be set up for a new run.

C. Data Transfer and Storage

The 1024 channels of data are transferred to a Tektronix 4051 minicomputer via the TYPE output of the MCA. The data are stored in files on a magnetic tape cartridge. The data require a file with 8091 bytes allocated. A data cartridge can hold 36 files of this length. When the data are stored, a file header is included. The file header contains all the experimental parameters, any changes in these parameters and the value of N_e. To ensure that there are no magnetic tape write errors, the data are recalled and checked before the MCA is erased.

CHAPTER VI

DATA ANALYSIS AND STATISTICS

Electrons and photons from the same scattering event have a definite time correlation. These true coincidences are made to fall into a group of about 20 channels of the 1024 channels of the MCA. Accidental coincidences occur when the TAC is started and stopped by electrons and photons from different scattering events or by noise counts. These accidental coincidences create a background which must be subtracted to obtain the number of true coincidences, N_c. The values and uncertainties of $\lambda(\theta_e)$ and $\chi(\theta_e)$ are then determined by the analysis of $N_c(\theta_e,\theta_\gamma)$ and its uncertainty. The other parameters discussed in Chapter II are calculated using $\lambda(\theta_e)$ and $\chi(\theta_e)$, and their uncertainties are determined by the standard method of propagation of errors.

A. Determination of N_c

The reduction of N_c from a time spectrum requires a least-squares fit to the background and the integration of the real coincidences in the peak above the background. The functional form of the background has been derived by Sutcliffe et al.[23] in terms of the probability of obtaining a stop pulse in the TAC. However, in the present work it was found that fitting the background to a straight line, an exponential or the expression given in Ref. 23, all gave virtually the same results.

The background was fit to a straight line in this work.

The method of least-squares fit to a straight line is well known and may be found in any good text such as Bevington.[49] Thus, only the results are given here. The background is fit to the straight line

$$y_i = a + ib \tag{31}$$

where i is the channel number and a and b are the optimum values of the intercept and slope, respectively. The quality of the fit of y_i to the data is given by the reduced chi-square,

$$\chi^2 = \frac{\sum_B [(y_i - N_i)^2/N_i]}{\sum_B i} \tag{32}$$

where the B indicates that the summation is over the background, excluding the 30 channels centered on the coincidence peak, N_i is the number of counts in the ith channel, and $\sqrt{N_i}$ is the one standard deviation counting uncertainty of N_i.

The integrated number of counts in the peak, N_c, and its standard deviation are given by

$$N_c = \sum_p N_i - y_i \tag{33}$$

$$\sigma_{N_c} = \left\{\sum_p [N_i + \sigma_a^2 + i^2\sigma_b^2 + 2i\sigma_{ab}^2]\right\}^{1/2} \tag{34}$$

where the p indicates that summation is over the peak, σ_a^2 is the variance of the intercept, σ_b^2 is the variance of the slope and σ_{ab}^2 is the covariance of a and b. The coincidence rate is $\dot{N}_c = N_c/T$, where T is the data accumulation time. The accidental rate per channel i is $\dot{N}_{ai} = y_i/T$. A typical coincidence spectrum and the least-squares fit to the background is shown in Fig. 14.

B. Determination of λ and χ

The expression of Macek and Jaecks,[14] given in Eq. (6), was rewritten by Golden and Steph[33] as

$$\dot{N}_c(\theta_e,\theta_\gamma) = \frac{3}{8\pi}\frac{I_e}{e}\sigma\varepsilon_e\varepsilon_\gamma J_c(\theta_e,\theta_\gamma)f(\lambda,\chi,\theta_\gamma) \tag{35}$$

where $\gamma'/\gamma = 1$, and

$$J_c(\theta_e,\theta_\gamma) = \int_{\ell_c} \rho(z)\Delta\Omega_e(z,\theta_e)\Delta\Omega_\gamma(z,\theta_\gamma)dz \tag{36}$$

where $\rho(z)$ is the density of target atoms, $\Delta\Omega_e$ and $\Delta\Omega_\gamma$ are the solid angles subtended by the electron and photon detectors, respectively, as a function of the position of a scattering event along the z-axis, and ℓ_c is the interaction length viewed mutually by the two detectors. The effect of variations in the electron beam intensity, atomic density and electron detector efficiency can be eliminated by normalizing the number of real coincidences N_c collected in a time T to the number of electron pulses N_e that started the TAC in this same time T,

$$N_e = T\left\{\frac{I_e}{e}\varepsilon_e(\sigma+\sigma')J_e(\theta_e) + \dot{n}_e\right\} \tag{37}$$

where σ' is the cross section for the production of electron counts in the window of the energy analyser due to states other than 2^1P, $\dot{n}_e$ is the count rate due to electronic noise and

$$J_e(\theta_e) = \int_{\ell_e} \rho(z)\Delta\Omega_e(z,\theta_e)dz \tag{38}$$

where ℓ_e is the interaction length viewed by the electron detector. In performing the experiment, the discriminator in the electron channel is adjusted so that $\dot{n}_e$ is zero. The normalized coincidence rate is then

$$\eta(\theta_e,\theta_\gamma) = \frac{\dot{N}_c}{\dot{N}_e} = \frac{3}{8\pi}\,\frac{\varepsilon_\gamma}{(1+\sigma'/\sigma)}\,\frac{J_c(\theta_e,\theta_\gamma)}{J_e(\theta_e)}\,f(\lambda,\chi,\theta_\gamma)\ . \tag{39}$$

Since the analysis is done at fixed θ_e, we may collect all quantities which only vary with θ_e into a constant $A(\theta_e)$ and write

$$\eta(\theta_e,\theta_\gamma) = A(\theta_e)J_c(\theta_e,\theta_\gamma)f(\lambda,\chi,\theta_\gamma)\ . \tag{40}$$

The analytic evaluation of $J_c(\theta_e,\theta_\gamma)$ is described in Sec. VII.A. The values of $J_c(\theta_e,\theta_\gamma)$ obtained in the present case are shown in Fig. 15. To ensure that ε_γ was constant during runs at a fixed θ_e the photon count rate was measured several times during the runs for each value of θ_γ. The variation of ε_γ for a given θ_e was always less than 1%.

If angular correlation data at fixed θ_e for various values of θ_γ is normalized to data obtained at $\theta_\gamma = \pi/2$, $A(\theta_e)$ in Eq. (40) does not need to be determined. Thus.

$$\frac{f(\lambda,\chi,\theta_\gamma)}{\lambda} = \frac{J_c(\theta_e,\pi/2)}{J_c(\theta_e,\theta_\gamma)}\,\frac{\eta(\theta_e,\theta_\gamma)}{\eta(\theta_e,\pi/2)}\ . \tag{41}$$

Then, using $x = (1-\lambda)/\lambda$ and $z = \cos\chi$ as parameters we use the method of least-squares and derive analytic expressions for the optimum values of λ and $|\chi|$ and their standard deviations in terms of the data and their standard deviations.

The chi-square of the fit of the normalized angular correlation function, $f(\lambda,\chi,\theta_\gamma)/\lambda$, to the angular correlation data, $\eta(\theta_\gamma)$, may be rewritten

$$\chi^2 = \sum_{\theta_\gamma} \frac{\left[m(\theta_\gamma) - \dfrac{f(\lambda,\chi,\theta_\gamma)}{\lambda}\right]^2}{\sigma_m^2} \tag{42}$$

where $m(\theta_\gamma) = \eta(\theta_\gamma)/\eta(\pi/2)$ and

$$\sigma_m^2 = m^2(\theta_\gamma)\left\{\frac{1}{N_c(\theta_\gamma)} + \frac{1}{N_c(\pi/2)}\right\} \tag{43}$$

The minimum value of χ^2 is given when the values of x and z are such that

$$\frac{\partial\chi^2}{\partial x} = \sum_{\theta_\gamma}\left[\frac{m(\theta_\gamma) - \frac{f(\lambda,\chi,\theta_\gamma)}{\lambda}}{\lambda_m^2}\right]\left[\sqrt{x}\cos^2\theta_\gamma - \sin\theta_\gamma\cos\theta_\gamma z\right] = 0 \tag{44a}$$

$$\frac{\partial\chi^2}{\partial z} = \sum_{\theta_\gamma}\left[\frac{m(\theta_\gamma) - \frac{f(\lambda,\chi,\theta_\gamma)}{\lambda}}{\sigma_m^2}\right]\left[-\sin\theta_\gamma\cos\theta_\gamma\right] = 0\ . \tag{44b}$$

These equations can be rearranged to yield a pair of simultaneous equations

$$xA + zG - 2z^2xD - xD - x^3E + 3zx^2F - zB = 0$$

$$B - G - x^2F + 2zxD = 0 \tag{45}$$

where the capital letters represent the sums of products:

$$A = \sum_{\theta_\gamma}\frac{m(\theta_\gamma)\cos^2\theta_\gamma}{\sigma_m^2}$$

$$B = \sum_{\theta_\gamma}\frac{m(\theta_\gamma)\sin^2\theta_\gamma\cos^2\theta_\gamma}{\sigma_m^2}$$

$$D = \sum_{\theta_\gamma}\frac{\sin^2\theta_\gamma\cos^2\theta_\gamma}{\sigma_m^2}$$

$$E = \sum_{\theta_\gamma}\frac{\cos^4\theta_\gamma}{\sigma_m^2}$$

$$F = \sum_{\theta_\gamma}\frac{\sin\theta_\gamma\cos^3\theta_\gamma}{\sigma_m^2}$$

$$G = \sum_{\theta_\gamma} \frac{\sin^3\theta_\gamma \cos\theta_\gamma}{\sigma_m^2} \tag{46}$$

The optimum values of x and z are determined by solving Eqs. (45). The results are

$$x = \left[\frac{F(B-G) + D(D-A)}{F^2 - ED}\right]^{\frac{1}{2}} \tag{47}$$

$$z = \frac{G - B + x^2 F}{2xD} \tag{48}$$

Analytical expressions for the uncertainties in x and z are also obtained:

$$\sigma_x^2 = \sum_{\theta_\gamma} \left[\frac{D\cos^2\theta_\gamma - F\sin^2\theta_\gamma \cos^2\theta_\gamma}{(DE - F^2)\sigma_m}\right]^2 \tag{49}$$

$$\sigma_z^2 = \sum_{\theta_\gamma} \left[\frac{U\cos^2\theta_\gamma + V\sin^2\theta_\gamma \cos^2\theta_\gamma}{\sigma_m}\right]^2 \tag{50}$$

where

$$U = \left(\frac{B-G}{x} + F\right)\left[\frac{1}{4\sqrt{x}\,(DE-F^2)}\right]$$

and

$$V = \left(\frac{G-B}{x} - F\right)\left[\frac{F}{4\sqrt{x}\,D(DE-F^2)}\right] - \frac{1}{2\sqrt{x}\,D}$$

Finally, the results for λ and χ and their uncertainties (one standard deviation) are

$$\lambda = \frac{1}{1+x} \tag{51}$$

$$\sigma_\lambda = (1+x)^{-2}\sigma_x \tag{52}$$

$$|\chi| = \cos^{-1} z \tag{53}$$

$$\sigma_\chi = (1-z^2)^{-1}\sigma_z \tag{54}$$

C. Discussion of Uncertainty in Fitted Parameters

Any experimental result should be accompanied by some statement of the uncertainty of the result. When the method of least-squares can be applied analytically, as in the present work, the uncertainties of the derived parameters can be directly related to the counting errors of the raw data. When the resulting uncertainty in a parameter is expressed as the square root of the variance, it is called the standard deviation of the parameter, σ_p. The significance of σ_p is usually expressed in terms of probability. If an additional measurement is made, the probability is 0.6827 that the new measurement will differ from the initial measurement by no more than σ_p. Thus uncertainties expressed as σ_p are often referred to as representing a 68% confidence limit. In the literature, an uncertainty of one standard deviation is sometimes referred to as probable uncertainty or probable error (PE). Strictly speaking, PE represents 50% confidence limits and is related to σ_p as

$$PE = 0.6745\ \sigma_p\ . \tag{55}$$

In the absence of adequate discussion, it is often impossible to determine which meaning an author attaches to PE.

The probability that an additional measurement will differ from the initial measurement by $<2\sigma_p$ is 0.9545. Thus, uncertainties expressed as $2\sigma_p$ are often referred to as representing a 95% confidence limit.

In the literature, an uncertainty of two standard deviations is often referred to as the maximum probable error or, somewhat misleadingly, as the maximum error. In principle, the maximum error of a measurement is infinite. This is implied in the definition of uncertainty in terms of the standard deviation. An infinite number of standard deviations must be allowed before the confidence limit is identically 100%. In some experiments it is not possible to calculate the uncertainty of a parameter analytically. A discussion of the procedure for the estimation of uncertainty in such experiments may be found in the work of Steph et al.[50]

The uncertainty of a measurement is usually expressed graphically as an error bar. In the literature, the error bars usually represent one standard deviation, unless they are specifically stated to represent two standard deviations. Results from different experiments are said to be in agreement within one standard deviation (or two standard deviations) when their respective error bars overlap. Measurements which differ by more than $2\sigma_p$ are generally said to be in disagreement.

In this work, all uncertainties are derived analytically and represent one standard deviation.

CHAPTER VII

DISCUSSION OF SYSTEMATIC ERROR

In order to ensure that the results are free from any systematic effects, various possible sources of systematic error have been investigated.

A. Background Effects

The interaction volume viewed by a detector (either photon or electron) is defined by the electron beam and the length ℓ that a detector views along the electron beam. When a detector is positioned perpendicular to the electron beam ($\theta = 90^o$), ℓ is defined by the opening angle θ of the detector and its distance from the electron beam. As θ is increased (or decreased), ℓ increases until at some maximum (or minimum) value of θ the entire electron beam is viewed. To relate the number of scattering events detected at different angles, one must correct for these changes in volume, or equivalently for changes in ℓ. In addition, the probability of detection for a scattering event depends on the solid angle, $\Delta\Omega(z,\theta)$, a detector subtends at a given point in the scattering volume and the density of scattering targets, $\rho(z)$, at that point. ($z=0$ is the center of intersection of the electron and atomic beams.) Thus, the rate of scattering events detected at a scattering angle θ is proportional to

$$\dot{N} \propto \int_{\ell(\theta)} \rho(z)\Delta\Omega(z,\theta)dz = J(\theta) \tag{56}$$

where the electron beam is taken to be uniform and along the z-axis. If $\rho(z)$ is written as the sum of the density of the atomic beam $\rho_B(z)$ and the uniform background density ρ_0, Eq. (56) may be written

$$J = \int_{\ell_B} \rho_B(z)\Delta\Omega(z,\theta)dz + \rho_0 \int_{\ell(\theta)} \Delta\Omega(z,\theta)dz \tag{57}$$

where ℓ_B is the width of the atomic beam. Since ℓ_B is sufficiently small ($\sim$0.5 mm) the variation of $\Delta\Omega(z,\theta)$ is negligible in the first integral and may be taken outside that integral to yield

$$\begin{aligned} J(\theta) &= \rho_0\Omega\left\{\int_{\ell_B} \frac{\rho_B(z)}{\rho_0}\, dz + \int_{\ell(\theta)} \frac{\Delta\Omega(z,\theta)}{\Omega}\, dz\right\} \\ &= \rho_0\Omega\left\{K + L(\theta)\right\} \end{aligned} \tag{58}$$

where Ω is the solid angle subtended at $z = 0$ and is independent of θ. The integral $L(\theta)$ is determined solely by properties of the detector and may be calculated exactly. While $\rho_B(z)$ can not be directly determined in this experiment, the value of the integral K may be inferred from measurements of the elastic electron scattering rate at a given angle with the atomic beam on, $N^B_{e\ell}$, and with the atomic beam off and the chamber flooded to the same background density, $N^F_{e\ell}$. The result is

$$K = \left\{\frac{N^B_{e\ell}(\theta_e)}{N^F_{e\ell}(\theta_e)} - 1\right\} L_e(\theta_e) \tag{59}$$

where the subscript e denotes the electron detector. This measurement is made at several values of θ_e to ensure that K is independent of θ_e. Once K is determined, we may calculate the integral

$$J_e(\theta_e) = \int_{\ell_e(\theta_e)} \rho(z)\Delta\Omega_e(z,\theta_e)dz = \rho_0\Omega_e\left(K + L_e(\theta_e)\right) \tag{60}$$

necessary for the electron count rate. The coincidence rate depends on both the electron and photon detectors and the required integral is

$$J_c(\theta_e,\theta_\gamma) = \int_{\ell_c(\theta_e,\theta_\gamma)} \rho(z)\Delta\Omega_e(z,\theta_e)\Delta\Omega_\gamma(z,\theta_\gamma)dz$$
$$= \rho_0\Omega_e\Omega_\gamma\{K + L_c(\theta_e,\theta_\gamma)\} \qquad (61)$$

as was discussed in Sec. VI.B.

Examples of $\Delta\Omega_e(z,\theta_e)$, $\Delta\Omega_\gamma(z,\theta_\gamma)$ and their product are shown in Fig. 16. Note that when $\theta \neq 90^o$, the maximum values of $\Delta\Omega_e$ and $\Delta\Omega_\gamma$ do not occur at $z = 0$. If the atomic beam were large, there could be a systematic error in the position of the detectors. In the present work, the beam diameter was $\sim$0.51 mm as discussed in Sec. III.E. Thus, the angular position of the detectors was unaffected.

The calculation of the integral given by Eq. (61) accounts for contributions to N_c due to scattering from both beam and background helium. As can be seen in Fig. 15, $J_c(\theta_e,\theta_\gamma)$ has no significant variation for $20^o < \theta_e < 160^o$. This is mainly due to the use of the two 1.33 mm apertures which form the grounded snout of the EEA. Since the EEA acceptance profile is determined solely by geometry, the snout places geometrical limits on the length ℓ_e. For values of $\theta_e \gtrsim 30^o$, the coincidence length, ℓ_c, is determined solely by ℓ_e. Thus, at these values of θ_e, ℓ_c is independent of θ_γ.

The angular divergence of electrons entering the focusing electrodes is limited to 3^o. This alleviates problems with background counts at small electron scattering angles, where elastic scattering is large, and at large electron scattering angles where N_e is small ($\lesssim$20 counts/sec) and can be seriously affected by spurious electrons.

Since the FC is displaced during runs at $\theta_e < 25^o$, the uncollected beam can scatter through the appartus and cause additional 2^1P excitations. This effect can be seen in the present work as an increase in the photon count rate of $\lesssim$2% for $\theta_e < 25^o$. Because the ratio $\Omega_\gamma/\Omega_e = 33.3$, the effect on the electron count rate is expected to be much smaller, and the effect on the coincidence rate rate to be smaller still.

B. Count Rate Distortion

When the TAC is started by electrons, and stopped by delayed photons the result is referred to as an inverted time spectrum. Since this work uses inverted time spectra, it is important to note that the detector efficiency ε_e includes both the efficiency of the CEM and the probability that an electron pulse will start the TAC. Thus, an electron which is detected but fails to start the TAC is no different from an electron which strikes the CEM but fails to produce a pulse: neither can produce a coincidence. Since this dead time correction is necessarily count rate dependent, it varies with both θ_e and θ_γ. This problem is completely eliminated by normalizing the data to N_e, where N_e represents only those electrons which actually start the TAC during the collection time T.

We have also analyzed the data by dividing N_c by the number of accidentals in the peak channel of the coincidence spectrum N_a^P. This procedure results in larger errors in the parameters because

N_a^P must be determined by fitting the background. However, for all angles studied, the optimum values of λ and $|\chi|$ are virtually the same regardless of which of these two normalization procedures is used. Since normalizing by N_a^P removes the dependence on ε_γ, this demonstrates the absence of significant instability or drift in the photon detector; and indicates that the effect of dead time on true stops is negligible in this work.

For most of the data runs an additional TAC and MCA were used to obtain a concurrent coincidence spectrum starting on photons and stopping on electrons. The result obtained with the TAC in this configuration is referred to as a direct spectrum. While the number of coincidences obtained in a direct spectrum is not a different measurement of N_c and cannot be used to lower the counting error,[48] it serves as a consistency check on the electronics. The values of N_c from the direct spectra are analysed by dividing by N_a^P and the results agree with the results of the inverted spectra. However, the raw number of coincidences differed considerably, particularly for $\theta_e \gtrsim 30^o$. When $R_\gamma > R_e$, data is lost in a direct time spectrum due to TAC dead time. This effect has been discussed in detail by Coleman[51] who gives an example: In a system with start and stop pulse rates of 10^6 and 10, respectively, a direct spectrum would record about 3% of the data, whereas the use of an inverted spectrum incurs virtually no loss. The amount of data lost in a direct spectrum is strongly count rate dependent. Since the photon count rate varies with θ_γ, this TAC dead time effect results in a systematic error in the measured angular correlation function. The size and effect of this systematic error is discussed with the results of Hollywood et al.[24] in Chapter VIII.

C. Angular Resolution

Another systematic effect is the angular resolution imposed by the finite size of the detectors. In the absence of a known shape for $\lambda(\theta_e)$ and $\chi(\theta_e)$ it is difficult to determine the effect of the angular resolution of the EEA, $\Delta\theta_e$. For this work $\Delta\theta_e$ was restricted to a flat response of $\pm 1^c$ and therefore any significant effect would require an extremely sharp maximum or minimum in $\lambda(\theta_e)$ or $\chi(\theta_e)$. Thus no effect was attributed to $\Delta\theta_e$. Since the shape of $f(\lambda,\chi,\theta_\gamma)$ is known, the effect of the angular resolution of the PD, $\Delta\theta_\gamma$, is readily calculated. The effect of a finite angular resolution on a measurement of a sinusoidal function such as $f(\lambda,\chi,\theta_\gamma)$ is to decrease its amplitude. This change in amplitude is a function only of the shape of the angular resolution and the fractional decrease is independent of amplitude. Therefore, if the shape of the angular resolution is known, the data can be corrected in the following way: Determine the fractional change in amplitude, ΔA, of a sine wave by folding it with the known angular resoltuion function of the detector. Find the best fit of the uncorrected data $f(\theta_\gamma)$ and from this fit determine the inflection angle θ_I $\{f(\theta_I) = 0.5\}$. The correction for any point $f^{corr}(\theta_\gamma)$ is then

$$f^{corr}(\theta_\gamma) = f(\theta_\gamma) + \Delta A\{f(\theta_\gamma) - f(\theta_I)\} \tag{62}$$

Assuming that the detection efficiency is constant across the face of the photon detector it has a flat angular response of $\pm 5^{\circ}$. This implies that $\Delta A = 0.006$, and since the maximum possible amplitude of $f(\lambda,\chi,\theta_{\gamma})$ is 0.5 the maximum possible correction is 0.003. This is only significant for points near θ_{min}, the minimum of $f(\lambda,\chi,\theta_{\gamma})$, and then only for $\theta_e < 20^{\circ}$. The effect of small changes in amplitude on λ and $|\chi|$ is detailed in Ref. 33.

D. Energy Resolution

In principle, it is only necessary that the energy resolution be sufficient to exclude detection of electrons from the n=3 manifold. In practice it is necessary that the resolution be sufficient to clearly resolve the 2^1P peak because of the normalization procedure. The normalized coincidence rate given by Eq. (39) is proporrional to $(1 + \sigma'/\sigma)^{-1}$. The ratio σ'/σ can become quite large for large values of θ_e. This can be seen in the energy loss spectrum for $\theta_e = 90^{\circ}$ presented in Fig. 13b. To ensure that σ'/σ was a minimum, an energy loss spectrum was taken prior to each data run to establish the position of the 2^1P peak. To ensure that σ'/σ was constant during a data run, the relevant potentials were monitored and another energy loss spectrum was taken at the completion of each run to ensure that there was no change in the position of the 2^1P peak. If the 2^1P peak is not resolved, its position must be estimated, thus introducing additional uncertainty in the measured angular correlation.

E. Resonant Trapping

The problem of resonant trapping has been considered in some detail by both Eminyan et al.[20] and Hollywood et al.[24] These authors show that resonance trapping at $\theta_e = 16^{\circ}$ has a negligible effect on λ but increases the value of $|\chi|$ as pressure increases. As pointed out in Golden and Steph,[33] when $|\chi|$ is small (<0.5 rad), the amplitude of the angular correlation function $f(\lambda,\chi,\theta_\gamma)$ is solely determined by $|\chi|$ and its phase by λ. This implies that the effect of resonance trapping is to add a uniform background to $f(\lambda,\chi,\theta_\gamma)$ which results in a decrease in its amplitude. If this behavior is independent of θ_e then its effect at values of $\theta_e \geq 50^{\circ}$ would be to decrease both λ and $|\chi|$. To ensure that resonant trapping would not be a problem in this experiment, the background pressure dependence of the photon detection rate at $\theta_\gamma = 90^{\circ}$ was measured and the results are shown in Fig. 17. The linearity and the zero intercept of the results indicate that resonant trapping is not present at a significant level and also show that there are no charged particles affecting the photon count rate.

CHAPTER VIII

EXPERIMENTAL RESULTS AND DISCUSSION

The experimental results are summarized in Table V where values of λ and $|\chi|$ are tabulated as a function of electron scattering angle. The table also lists values for θ_{min} calculated from Eq. (21), the orientation $|O_{1-}^{col}|$ calculated from Eq. (9) and the non-vanishing components of the alignment tensor calculated from Eqs. (10) - (12). The angular correlation functions measured in this work for all angles studied are shown in Fig. 18. The total counting time represented by these data is $\sim$2200 hrs.

Since the use of Eq. (41) allows an analytic solution for the parameters λ and $|\chi|$, it is only necessary to measure $N_c(\theta_e,\pi/2)$ and $N_c(\theta_e,\theta_\gamma)$ at two other values of θ_γ. When the $\theta_e = 10^\circ$ data is analysed using all 11 data points shown in Fig. 18b, the results obtained are $\lambda = 0.488 \pm 0.016$, and $|\chi| = 0.371 \pm 0.038$. When the data is analysed using only the three points $\theta_\gamma = 52.5^\circ$, 90° and 135° the results are $\lambda = 0.485 \pm 0.018$ and $|\chi| = 0.376 \pm 0.059$. Thus, the results are not significantly different. However, when only three points are used there is an increase in the uncertainty which is accompanied by a significant reduction in the data accumulation time. Even though we need to measure $N_c(\theta_e,\theta_\gamma)$

at only three values of θ_γ, the data accumulation time can become prohibitively long at large values of θ_e. A total of 28 days of counting time were required to accumulate the data used to obtain the angular correlation function at θ_e=100°, shown in Fig. 18i. In order to reduce the uncertainties in λ and $|\chi|$ by a factor of 2, it would be necessary to increase the data accumulation time or the product $\Omega_e\Omega_\gamma$ by a factor of 4. Increasing the product $\Omega_e\Omega_\gamma$ carries with it an angular averaging problem and increasing the data accumulation time is not practical.

The measured variation of λ with θ_e is presented in Fig. 19a for the range $5° \leq \theta_e \leq 50°$ and in Fig. 19b for the range $60° \leq \theta_e \leq 155°$, together with the results of previous measurements. The measured variation of $|\chi|$ with θ_e is shown in Fig. 20 together with the results from previous measurements and calculations. The present results for $|\chi|$ agree with all previous measurements in their common angular ranges. The present results for λ agree with all previous measurements for values of $\theta_e < 70°$. Our value of λ at $\theta_e = 90°$ agrees with the result of Sutcliffe et al.,[23] but our values of λ for θ_e = 80°, 90° and 100° are about 20% to 40% larger than the corresponding values obtained by Hollywood et al.[24] The angular correlation data of Hollywood et al.[24] were obtained by starting a TAC with photons and stopping with electrons. Their values of N_c were normalized by dividing by the total number of electrons detected during the accumulation time. As was discussed in Sec. VII.B, values of N_c obtained using photon starts should be normalized to the number of accidentals to eliminate TAC dead time effects on the value of N_c. In order to study this effect, coincidence spectra at $\theta_e = 20°$ and $\theta_e = 90°$ were measured using photon starts. When the 20° data was analysed using the technique of Hollywood et al.,[24] a value of λ of 0.285 and a value of $|\chi|$ of 0.578 were obtained. In a similar fashion at $\theta_e = 90°$ using their technique a value of λ of 0.760 and a value of $|\chi|$ of 1.996 were obtained. The values of λ and $|\chi|$ obtained at $\theta_e = 20°$ are 4% less and 1.6% greater than those obtained using our method. At $\theta_e = 90°$, the value of $|\chi|$ is unchanged while the value of λ is 14.6% less than that obtained using our method. Thus the major effect of the analysis used by Hollywood et al.[24] is to obtain too small a value of λ at large values of θ_e, where the photon count rate is large compared to the electron count rate. Since this effect is count rate dependent, it is difficult to estimate how much the values of λ obtained at large values of θ_e by Hollywood et al.[24] were depressed due to their normalization procedure. However, because the background is a negligible effect in the work of Hollywood et al.,[24] $\dot{N}_\gamma$ should have a larger variation with θ_γ than in the present experiment and therefore this count rate dependent effect should be larger in their work than in the present work. This analysis leads to the conclusion that for $\theta_e \geq 80°$ the method of analysis used by Hollywood et al.[24] yields an angular correlation function with too small an amplitude and an altered phase.

The present results for λ are compared with the results of several calculations in Fig. 21. All of the present data points are in agreement within one standard deviation with the calculation of Madison and Calhoun.[25,52] It should be noted that the most recent R-matrix calculation of Fon et al.[31] agrees quite well with the present large angle data and the only serious disagreement is at the minimum ($\theta_e \sim 20°$). In contrast, their results for $|\chi|$ agree remarkably well with all of the data of $\theta_e \lesssim 20°$ while their result disagrees with all of the data at larger angles.

Finally, the values of the minimum in the angular correlation function $f(\lambda,\chi,\theta_\gamma)$ as a function of θ_e are presented in Fig. 22. This function depends upon the values of both λ and $|\chi|$ and is calculated using Eq. (21). All of the experimental data is in agreement with the exception of the points at 90° and 100°. The R-matrix calculation of Fon et al.[31] agrees reasonably with the present data at all angles.

In conclusion, the experimental apparatus and the measurement technique of the present work have been thoroughly analysed for sources of systematic and random error. Where there is disagreement with previous measurement, the disagreement has been explained and resolved in favor of the present results. There is excellent agreement between the most recent and sensitive theoretical estimates.[31,52] The excellent agreement between experimental results at small angles indicates that the parameters λ and $|\chi|$ are established to better than 5% for $\theta_e < 40°$. The present results have established λ and $|\chi|$ at the larger angles to $\sim$12%.

Presently the apparatus is measuring λ and $|\chi|$ for an impact energy of 100 eV and this will be followed by measurements at 200 eV. Then measurements of λ and $|\chi|$ will be made from 40 eV down to the region of the threshold of the 2^1P state.

REFERENCES

1. J. J. Thomson, Phil. Mag. 44, 293 (1897).
2. J. J. Thomson, Phil. Mag. 48, 547 (1899).
3. H. Geiger and E. Marsden, Pro. Roy. Soc. (London) A 82, 495 (1909).
4. E. Rutherford, Phil. Mag. 21, 669 (1911).
5. N. Bohr, Phil. Mag. 26, 1,476,857 (1913).
6. C. Ramsauer, Ann. Physik 64, 513 (1921).
7. R. B. Brode, Phys. Rev. 25, 636 (1925).
8. B. L. Moiseiwitsch and S. J. Smith, Rev. Mod. Phys. 40, 238 (1968).
9. S. Bashkin and G. Beauchemin, Can. J. Phys. 44, 1603 (1966).
10. E. L. Chupp, L. W. Dotchiu and D. J. Pegg, Phys. REv. 175, 44 (1968).
11. J. Macek, Phys. Rev. Lett. 23, 1 (1969).
12. G. C. M. King, A. Adams and F. H. Read, J. Phys. B 5, L254 (1972).
13. I. C. Percival and M. J. Seaton, Phil. Trans. Roy. Soc. (London) A 251, 113 (1958).
14. J. Macek and D. H. Jaecks, Phys. Rev. A 4, 2288 (1971).
15. U. Fano and J. Macek, Rev. Mod. Phys. 45, 553 (1973).
16. K. Rubin, B. Bederson, M. Goldstein and R. E. Collins, Phys. Rev. 182, 201 (1969).
17. J. Wykes, J. Phys. B 5, 1126 (1972).
18. K. Blum and H. Kleinpoppen, J. Phys. B 8, 922 (1975); Physics Reports (to be published).

19. J. Eichler and W. Fritsch, Phys. B 9, 1477 (1976).

20. M. Eminyan, K. B. MacAdam, J. Slevin, and H. Kleinpoppen, Phys. Rev. Lett. 31, 576 (1973); J. Phys. B 7, 1519 (1974).

21. A. Ugbabe, H. Arriola, P. J. O. Teubner, and E. Weigold, J. Phys. B 10, 72 (1977).

22. K. H. Tan, J. Fryar, P. S. Farago, and J. W. McConkey, J. Phys B 10, 1073 (1977).

23. V. C. Sutcliffe, G. N. Haddad, N. C. Steph and D. E. Golden, Phys. Rev. A 17, 100 (1978).

24. M. T. Hollywood, A. Crowe, and J. F. Williams, J. Phys. B 12, 819 (1979).

25. D. H. Madison and R. V. Calhoun (unpublished).

26. L. D. Thomas, G. Csanak, H. S. Taylor and G. S. Yarlagadda, J. Phys. B 10, 1073 (1977).

27. M. R. Flannery and K. J. McCann, Phys. Rev. A 12, 846 (1975).

28. T. Scott and M. R. C. McDowell, J. Phys. B 8, 1851 (1975).

29. B. H. Bransden and K. H. Winters, J. Phys. B 9, 1115 (1976).

30. G. D. Meneses, N. T. Padial, and Gy Csanak, J. Phys. B 11, L237 (1978).

31. W. C. Fon, K. A. Berrington and A. D. Kingston, J. Phys. B 12, L171 (1979).

32. K. L. Baluja and M. R. C. McDowell, J. Phys. B (to be published).

33. D. E. Golden and N. C. Steph, "Correlation in Electron Atom Excitation," in Coherence and Correlation in Atomic Physics, H. Kleinpoppen and J. Williams, eds., Plenum Press (to be published).

34. H. Kleinpoppen, Atomic Physics, Vol. 4, Plenum Press, New York, 449 (1975).

35. M. R. C. McDowell, Comm. Atom. Mol. Phys. 6, 1 (1976).

36. H. Kleinpoppen, Comm. Atom. Mol. Phys. 6, 35 (1976).

37. L. A. Morgan and M. R. C. McDowell, Comm. Atom. Mol. Phys. 7, 123 (1978).

38. M. C. Standage and H. Kleinpoppen, Phys. Rev. Lett. 36, 577 (1976).

39. R. S. Longhurst, Geometrical and Physical Optics, 3rd ed., Longman Group Limited, London (1973).

40. The expressions for S_1, S_2 and S_3 in terms of the intensity of radiation are taken from Ref. 39. The negative sign in the definition of S_3 is not present in Principles of Optics by Born and Wolfe, but this is the present majority view of this parameter. This definition leads to expressions in agreement with those of Ref. 37.

41. M. C. Standage, J. Phys. B 10, 2789 (1977).

42. V. C. Sutcliffe, Ph.D. thesis, University of Oklahoma, Norman, Oklahoma.

43. D. E. Golden, F. D. Schowengerdt and J. Macek, J. Phys. B 7, 478 (1974).

44. F. H. Read, J. Comer, R. E. Imhof, J. N. H. Brunt and E. Harting, J. Elect. Spec. 4, 293 (1974).

45. C. E. Kuyatt, Methods of Experimental Physics, Vol. 7A, Academic Press, New York (1968).

46. H. P. Myers, Proc. Roy. Soc. (London) 215A, 329 (1952).

47. A. I. Naumov, Soviet Physics-Tech. Phys. 8, 88 (1963).

48. Sutcliffe et al. in Ref. 23 used both photon starts and electron starts at the same time in two TACs to reduce the counting error. We have determined experimentally that only $\sim$5% of the coincidences

detected using photon starts are different from those detected using electron starts. Thus their uncertainties should be increased by about $\sqrt{2}$.

49. P. R. Bevington, Data Reduction and Error Analysis for the Physical Sciences, McGraw-Hill (1969).

50. N. C. Steph, L. McDonald and D. E.Golden, J. Phys. B 12, 1507 (1979).

51. P. G. Coleman, Appl. Phys. 5, 223 (1974).

52. D. H. Madison (private communication).

53. M. J. Mumma, M. Misakian, W. M. Jackson and J. L. Faris, Phys. Rev. A 9, 203 (1974).

TABLE I. EG physical dimensions and operating voltages.

Element	Voltage* (Volt)	Tube Diameter (mm)	Tube Length (mm)
Anode	8.21	6.35	5.21
2	93.10	6.35	12.70
3	39.46	6.35	8.13
4	112.90	6.35	27.38
5	38.29	6.35	20.96
6	11.52	6.35	9.53

*Voltage measured with respect to a cathode common voltage of 82.32 Volts. The current was ∿2 μAmp.

Cathode emitting surface area.................... 15.8 mm^2

Angle of Pierce element.......................... 58.5^o

Anode-cathode spacing............................ 2.9 mm

Anode aperture diameter.......................... 1.0 mm

2 element aperture diameter...................... 1.0 mm

Snout replaceable aperture diameter.............. 1.27 mm

Snout fixed aperture............................. 1.27 mm

Lens spacing..................................... 1.0 mm

Snout length..................................... 24.3 mm

Snout-collision center distance.................. 25.4 mm

TABLE II. Cathode activation schedule.

Elapsed Time (min)	Pressure at Power Change (10^{-8} Torr)	Filament Current (Amp)	Peak Pressure (10^{-8} Torr)
	2.0	0.1	2
5	2.0	0.2	2
15	2.4	0.25	10
20	2.5	0.35	21
35	3.2	0.4	9
45	3.2	0.41	9
51	3.2	0.42	12
60	3.5	0.44	14
75	6.0	0.46	22
90	20.0	0.47	26
100	22.0	0.48	40
120	22.0	0.50	30
133	14.0	0.53	28
140	4.6	0.6	9
145	5.2	0.7	10
160	6.4	0.53	--

TABLE III. EEA physical dimensions and operating voltages.

Element	Voltage* (Volt)	Tube diameter (mm)	Tube Length (mm)
6	24.53	6.35	9.53
5	60.79	6.35	20.96
4	20.73	6.35	27.38
R	2.10	8.03	9.58
SR	19.98	8.03	10.16
IS	23.712	NA	NA
OS	17.618	NA	NA

*Voltage with respect to analyser common for $\Delta E = 21.22$ Volt.

Collision center to snout........................ 18.65 mm

Snout length..................................... 25.4 mm

Snout fixed aperture diameter.................... 1.33 mm

Snout replaceable aperture diameter.............. 1.33 mm

Input (output) aperture.......................... 1.02 mm

IS radius.. 46.9 mm

OS radius.. 54.8 mm

Mean radius...................................... 50.8 mm

$\Delta\theta_e$.. 0.865°

Ω_e .... 7.16×10^{-4} sr

TABLE IV. Photon detector physical dimensions.

Scattering center to aperture..................	25.0 mm
Aperture to CEM face...........................	29.4 mm
Aperture diameter..............................	4.75 mm
CEM face diameter..............................	9.5 mm
Front aperture to first grid...................	24.13 mm
Grid spacing...................................	1.96 mm
$\Delta\theta_\gamma$	$\pm 5^0$
Ω_γ	2.39×10^{-2} sr

TABLE V. Values of the parameters derived from the measured angular correlations as a function of the electron scattering angle θ_e, for incident energy of 80 eV. Uncertainties quoted represent one standard deviation.

θ_e(deg)	λ	$\lvert\chi\rvert$ (rad)	θ_{min}(deg)	$\lvert O_{1-}^{col}\rvert$	$\lvert A_0^{col}\rvert$	$\lvert A_{1+}^{col}\rvert$	$\lvert A_{2+}^{col}\rvert$
5	0.766+0.020	0.231+0.220	28.57+1.71	0.097+0.009	-0.649+0.030	0.412+0.012	-0.117+0.010
10	0.488+0.015	0.370+0.038	45.71+0.94	0.181+0.007	-0.232+0.023	0.466+0.003	-0.256+0.008
20	0.297+0.014	0.568+0.054	58.86+1.08	0.246+0.006	0.055+0.021	0.385+0.006	-0.352+0.007
30	0.444+0.023	1.182+0.053	53.27+3.34	0.460+0.005	-0.166+0.035	0.188+0.011	-0.278+0.012
50	0.919+0.054	1.994+0.146	-7.47+3.86	0.249+0.076	-0.879+0.081	-0.112+0.037	-0.041+0.027
60	0.903+0.074	2.424+0.416	-14.45+7.70	0.195+0.068	-0.855+0.111	-0.223+0.077	-0.049+0.037
80	0.861+0.102	2.570+0.402	-19.44+9.02	0.187+0.065	-0.792+0.153	-0.291+0.092	-0.070+0.051
90	0.871+0.103	2.001+0.243	-10.33+7.70	0.305+0.105	-0.807+0.154	-0.140+0.057	-0.065+0.051
100	0.838+0.108	1.842+0.175	-8.16+6.64	0.355+0.096	-0.757+0.162	-0.099+0.047	-0.081+0.054

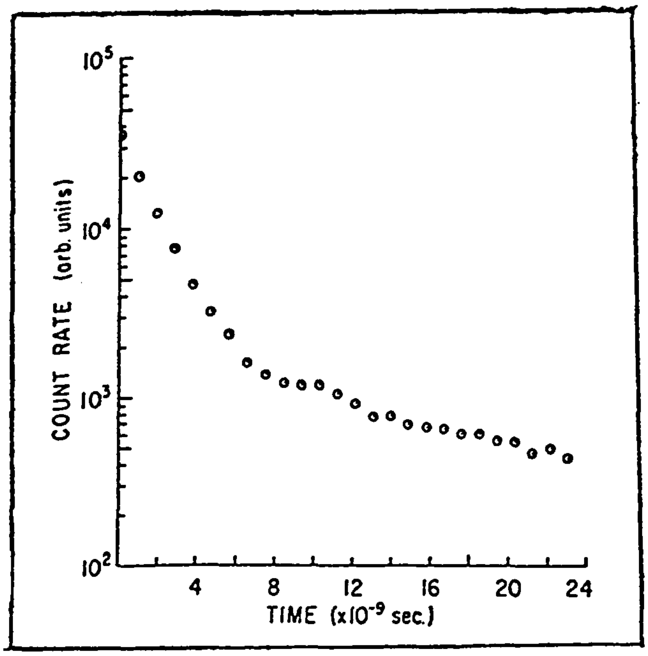

Fig. 1. An intensity decay curve of the Lyman α line in hydrogen, taken from Ref. 10.

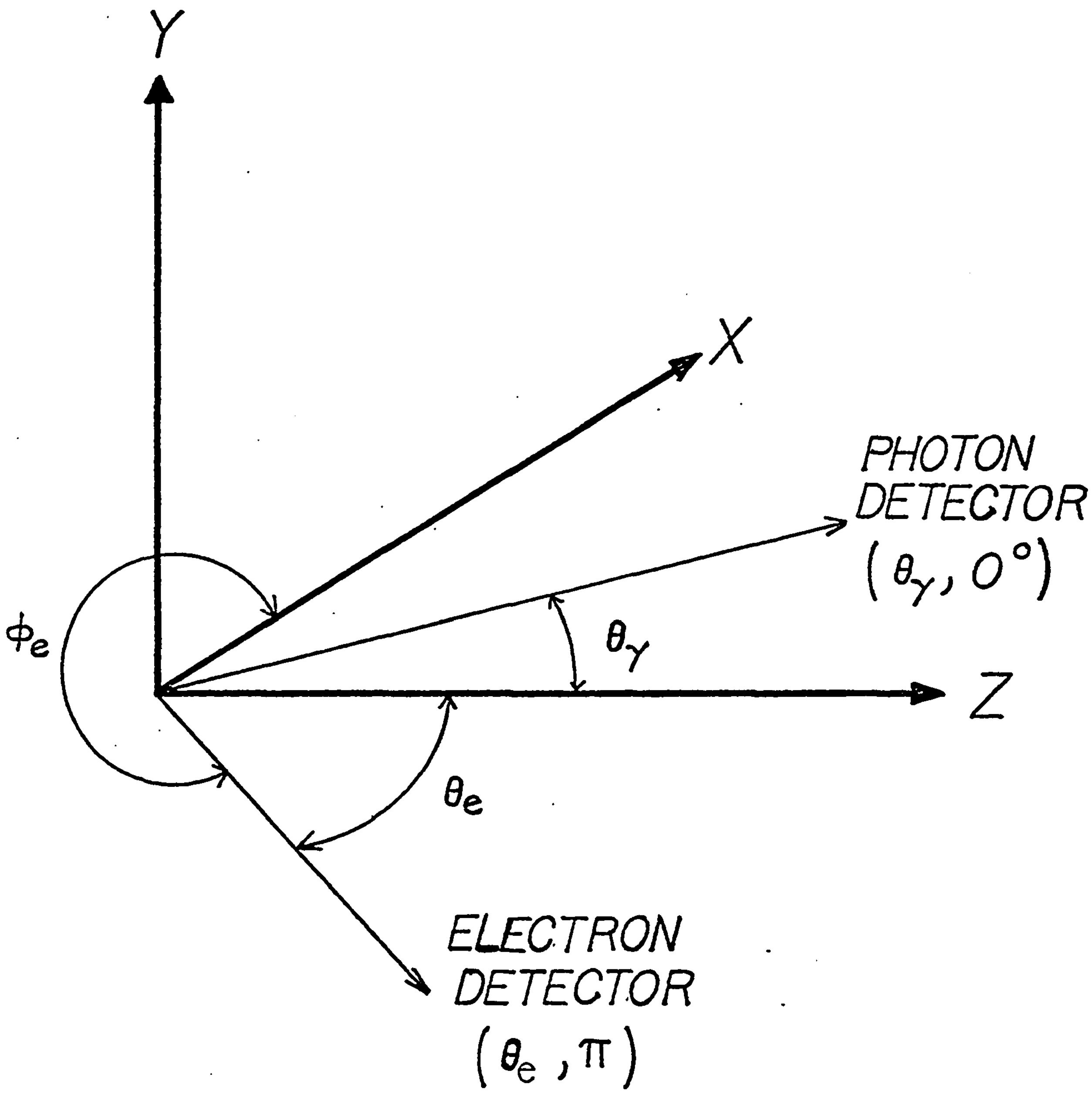

Fig. 2. Detector geometry in the collision frame defined by the incident electron beam and the crossed atomic beam.

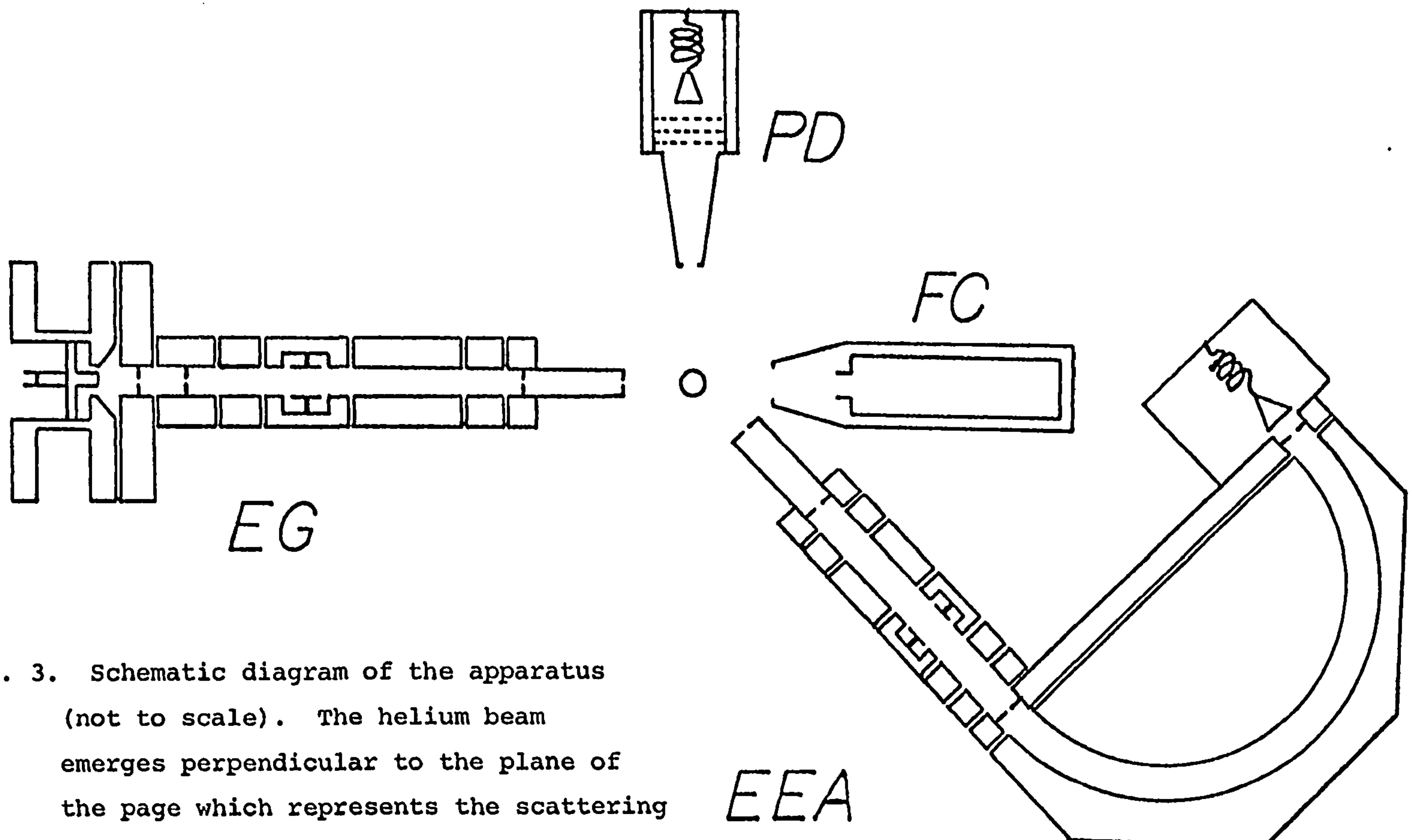

Fig. 3. Schematic diagram of the apparatus (not to scale). The helium beam emerges perpendicular to the plane of the page which represents the scattering plane. EG, electron gun; EEA, electrostatic energy analyser; FC, Faraday cup; PD, photon detector.

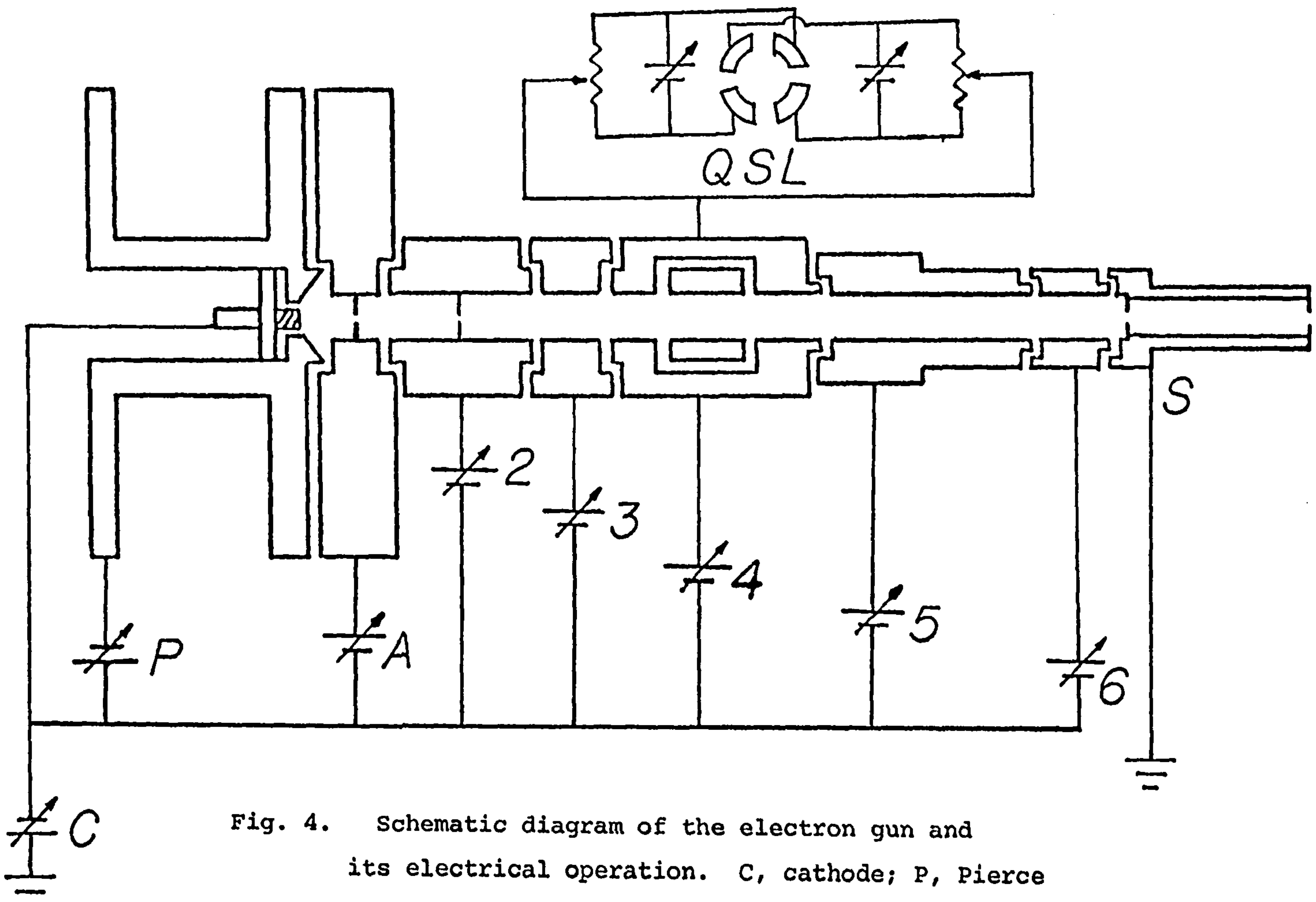

Fig. 4. Schematic diagram of the electron gun and its electrical operation. C, cathode; P, Pierce element; A, anode; S, snout; QSL, quadrupole steering lens.

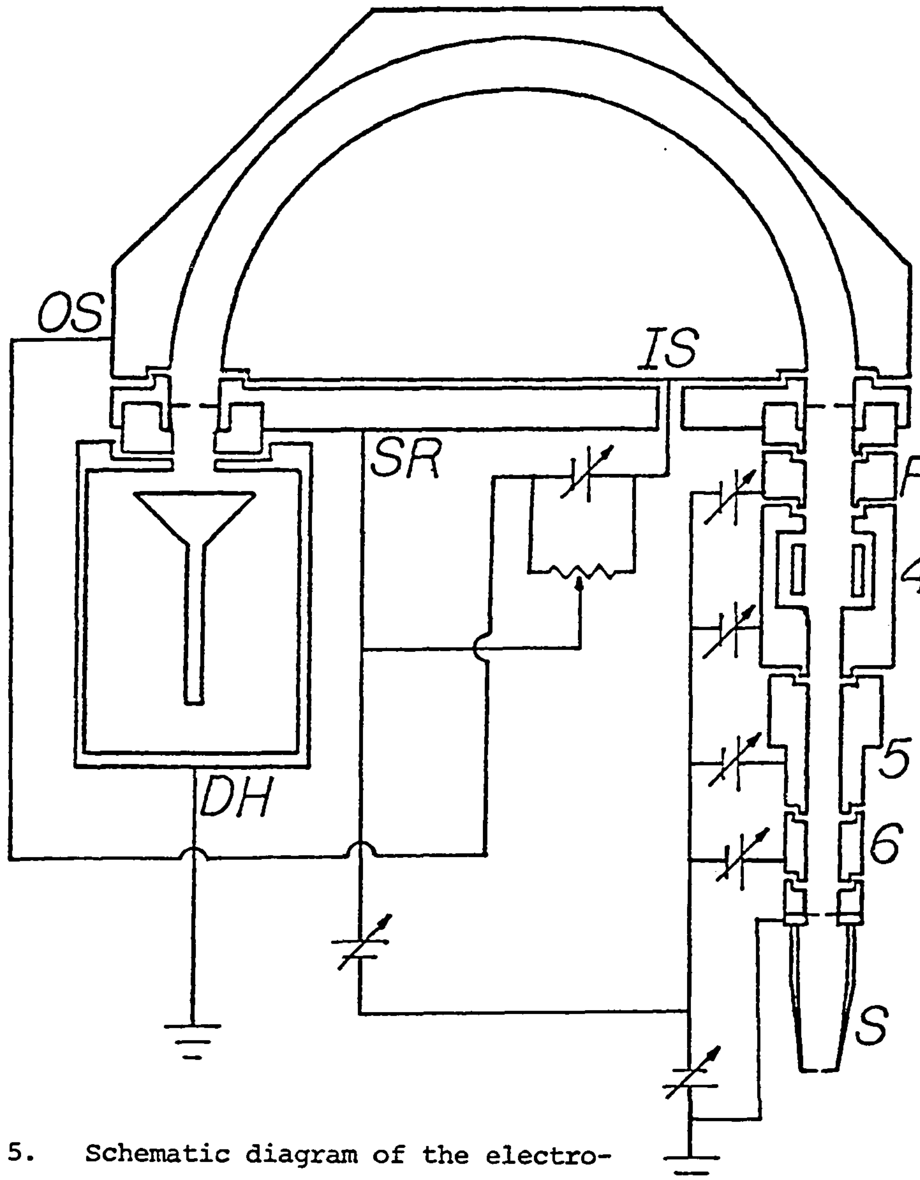

Fig. 5. Schematic diagram of the electrostatic energy analyser and its electrical operation. S, snout; SR, sphere reference electrode; IS, inner sphere; OS, outer sphere; DH, detector housing.

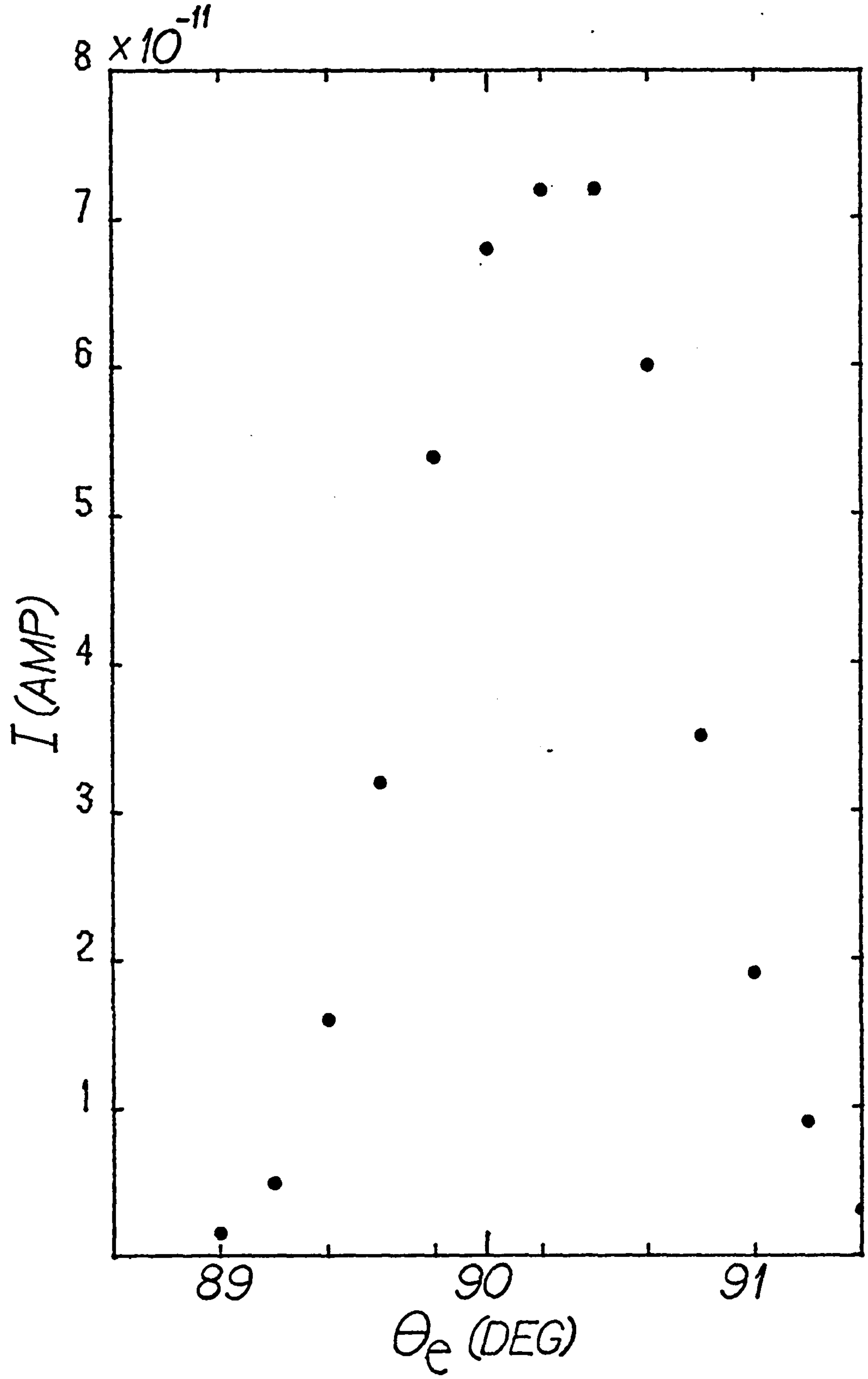

Fig. 6a. Measurement of the electron beam profile with the EEA lenses grounded.

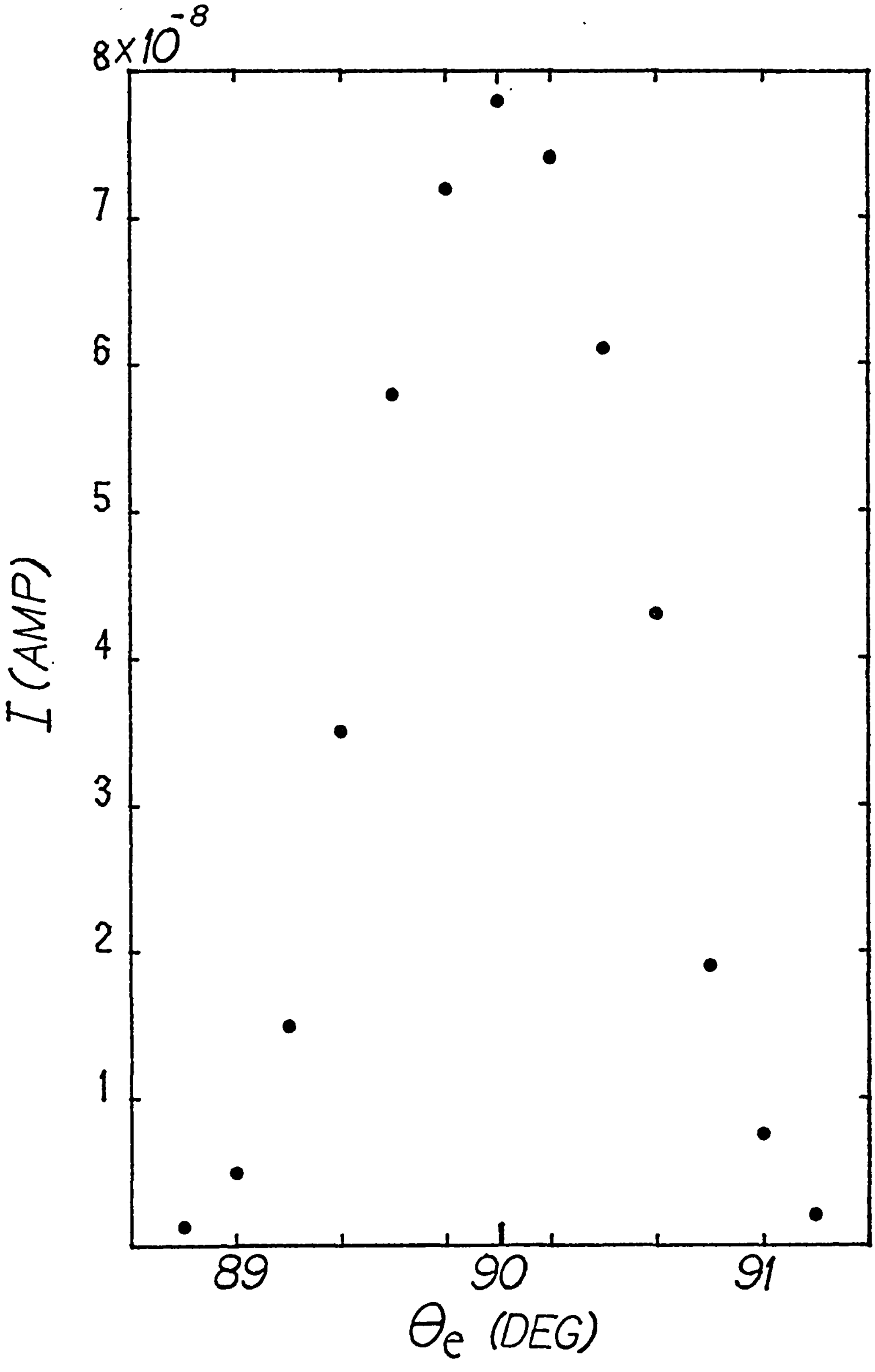

Fig. 6b. Measurement of the electron beam profile with the EEA lenses at their operating potentials.

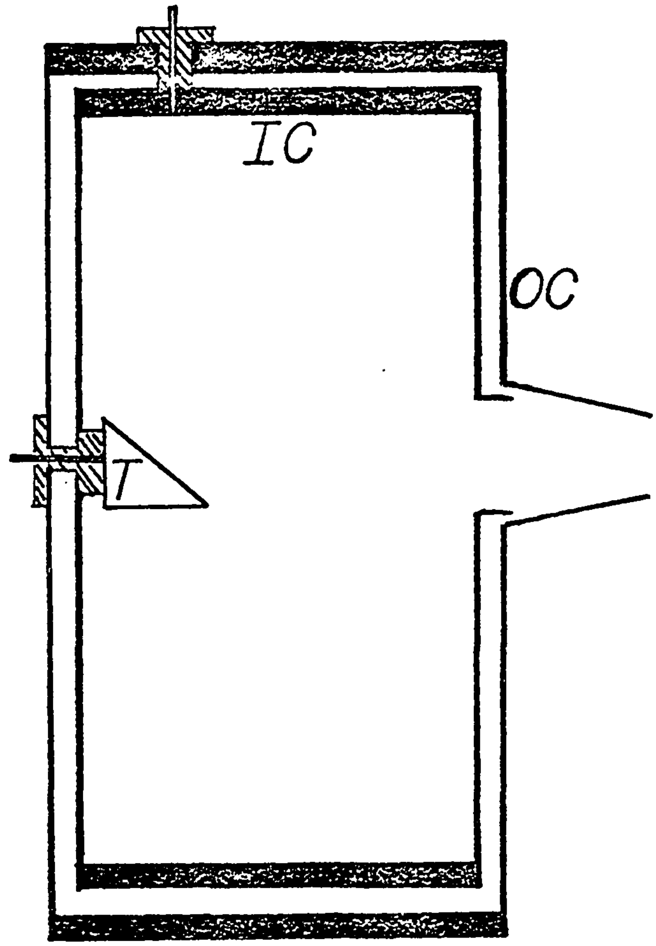

Fig. 7. Schematic diagram of the Faraday cup. OC, outer cup; IC, inner cup; T, target (to deflect electrons away from the entrance aperture).

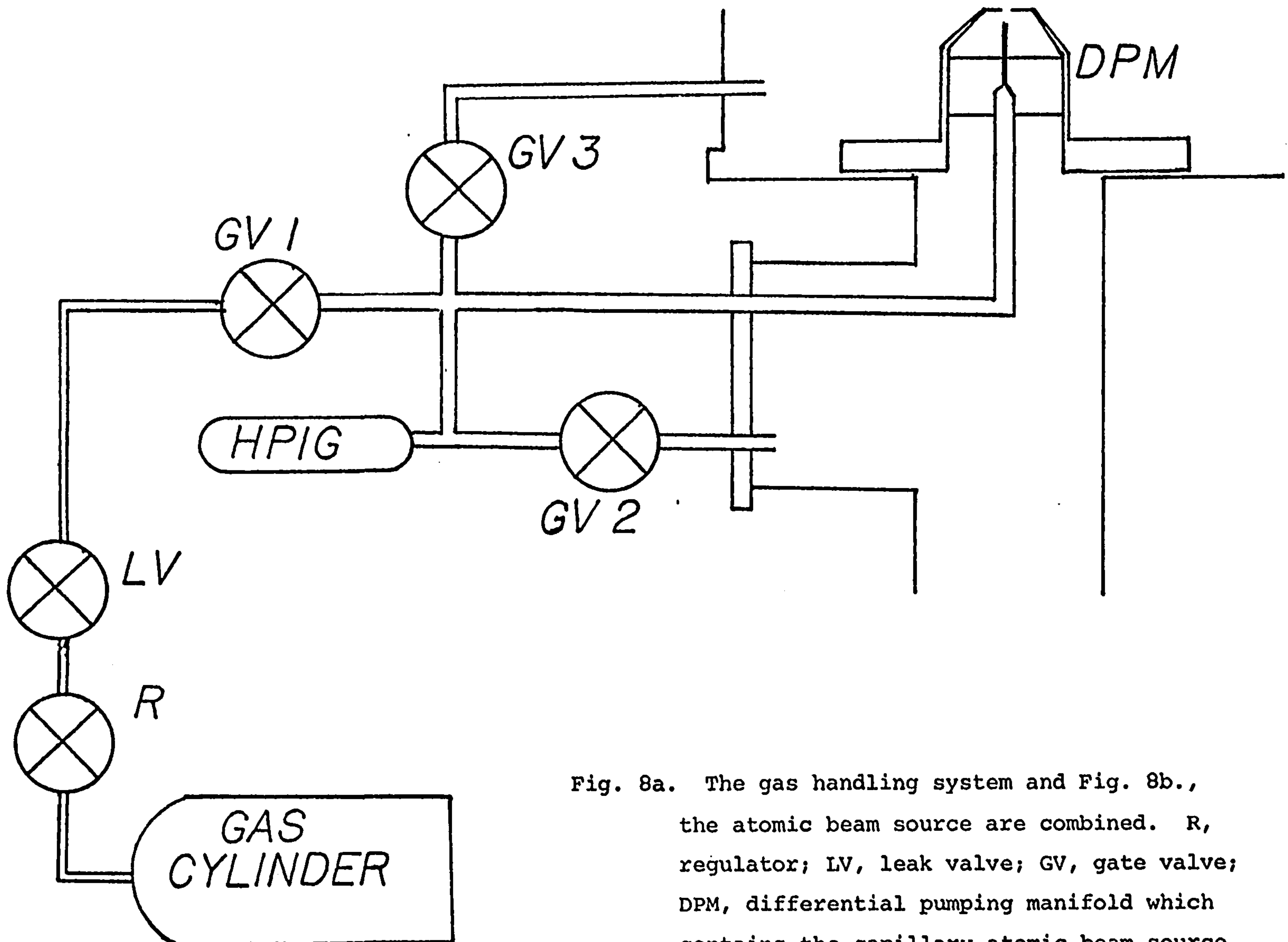

Fig. 8a. The gas handling system and Fig. 8b., the atomic beam source are combined. R, regulator; LV, leak valve; GV, gate valve; DPM, differential pumping manifold which contains the capillary atomic beam source. The capillary is held and aligned by spider bushings.

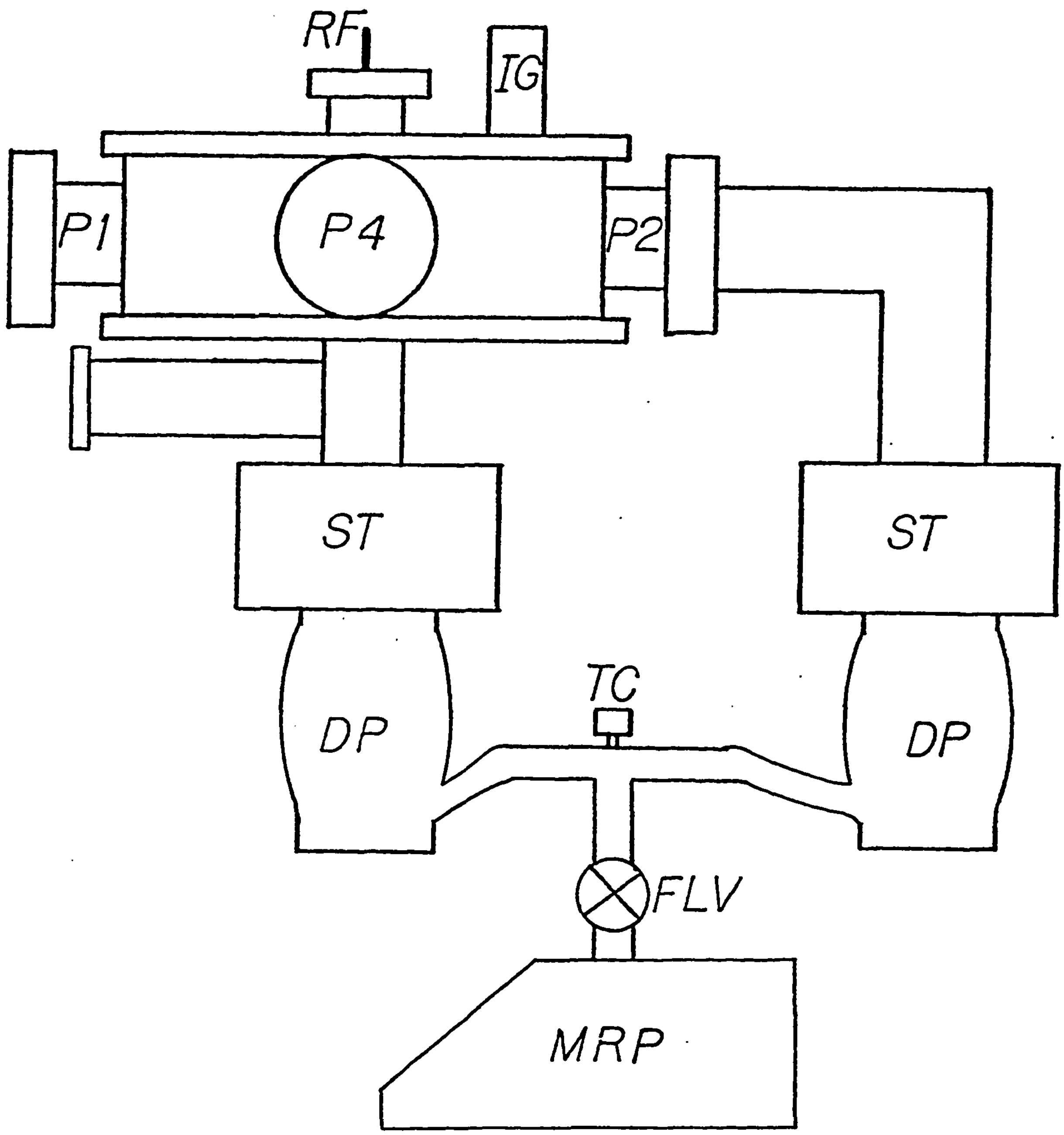

Fig. 9. Schematic diagram of the ultra-high vacuum system. RF, rotary feed thru; IG, ionization gauge; P1-P4, access ports; ST, sorbent traps; DP, diffusion pumps; TC, thermocouple foreline pressure gauge; FLV, foreline valve; MRP, mechanical rotary pump.

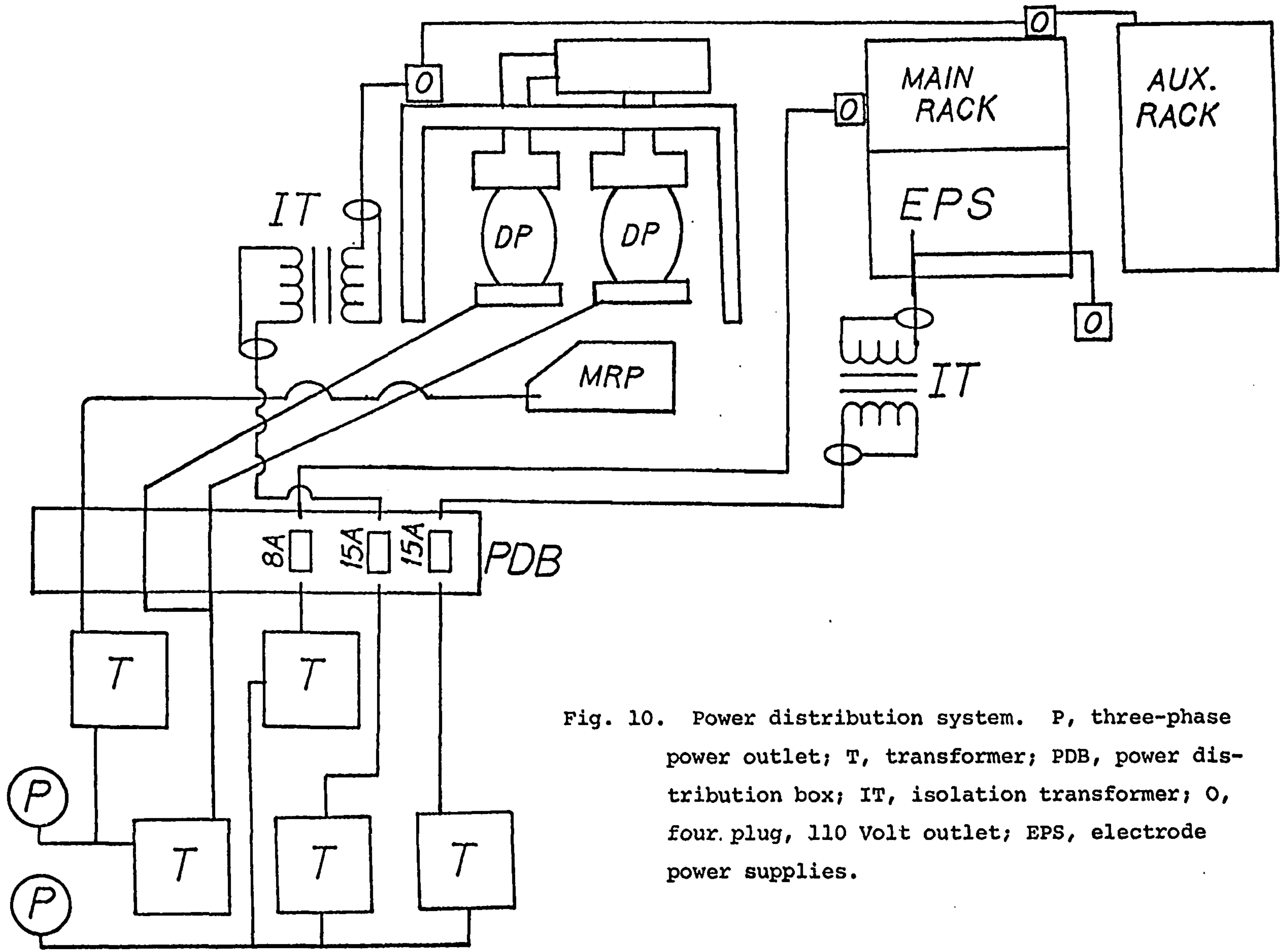

Fig. 10. Power distribution system. P, three-phase power outlet; T, transformer; PDB, power distribution box; IT, isolation transformer; O, four plug, 110 Volt outlet; EPS, electrode power supplies.

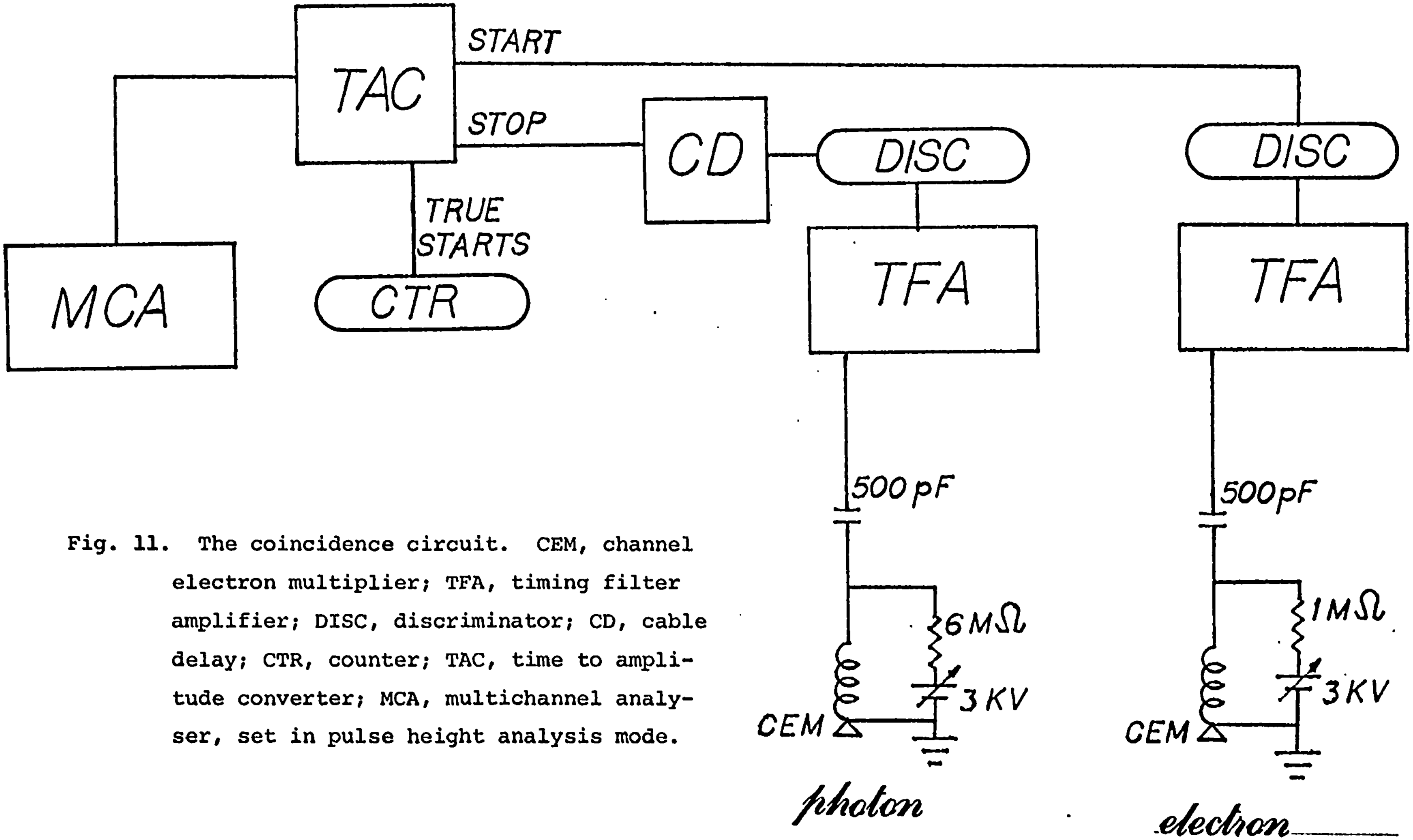

Fig. 11. The coincidence circuit. CEM, channel electron multiplier; TFA, timing filter amplifier; DISC, discriminator; CD, cable delay; CTR, counter; TAC, time to amplitude converter; MCA, multichannel analyser, set in pulse height analysis mode.

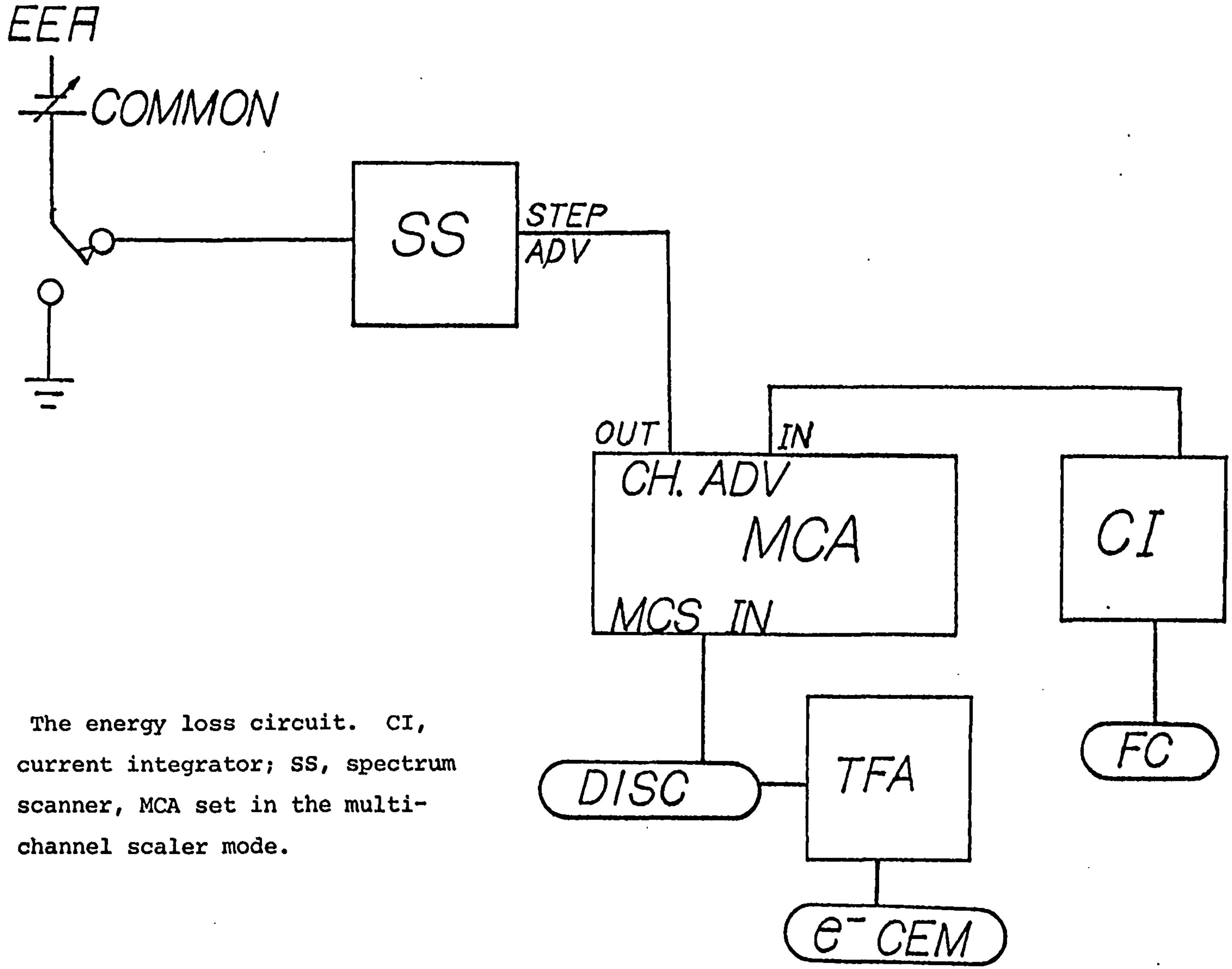

Fig. 12. The energy loss circuit. CI, current integrator; SS, spectrum scanner, MCA set in the multichannel scaler mode.

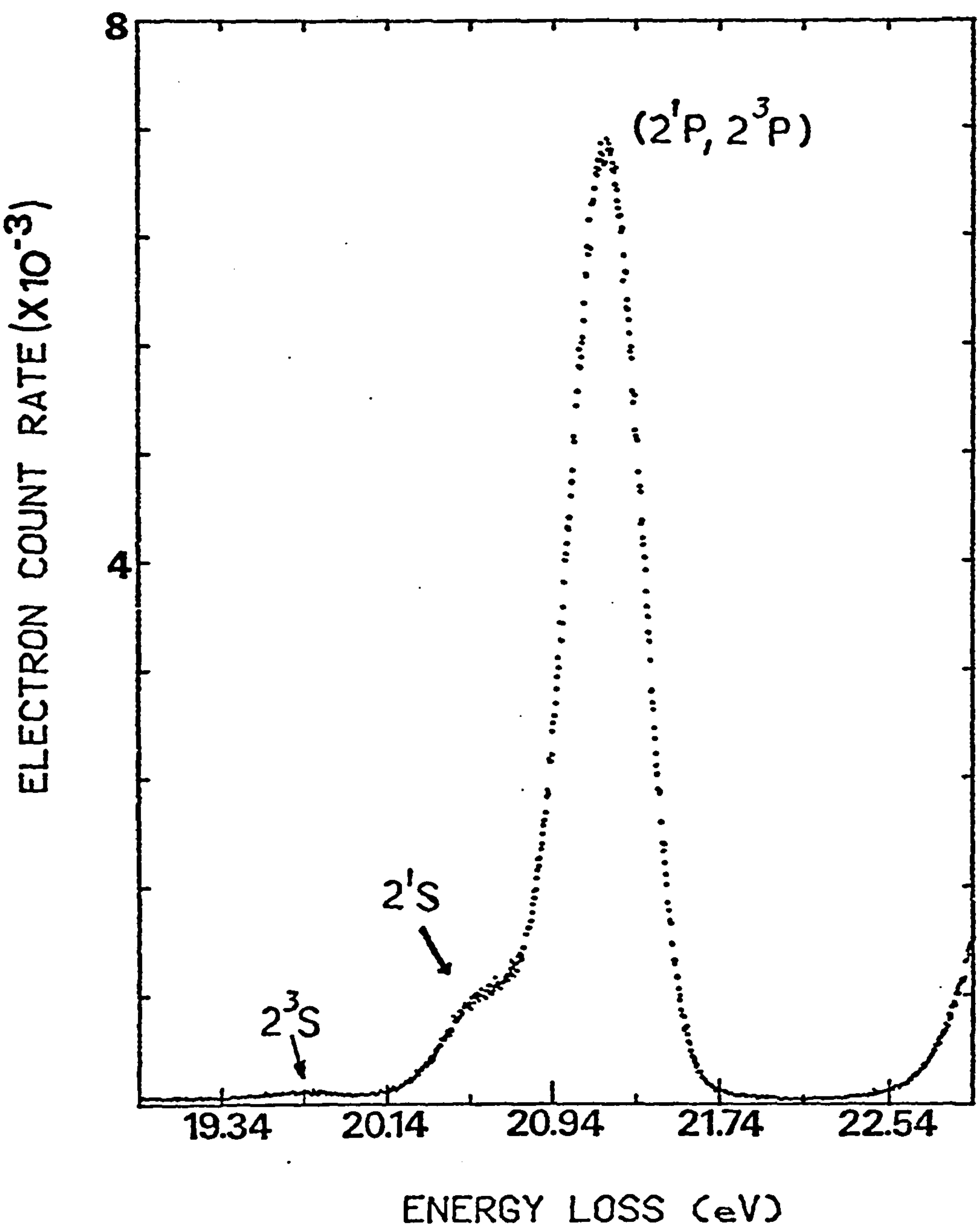

Fig. 13a. Energy loss spectrum for $\theta_e = 10°$. (2^3P is a negligible component.

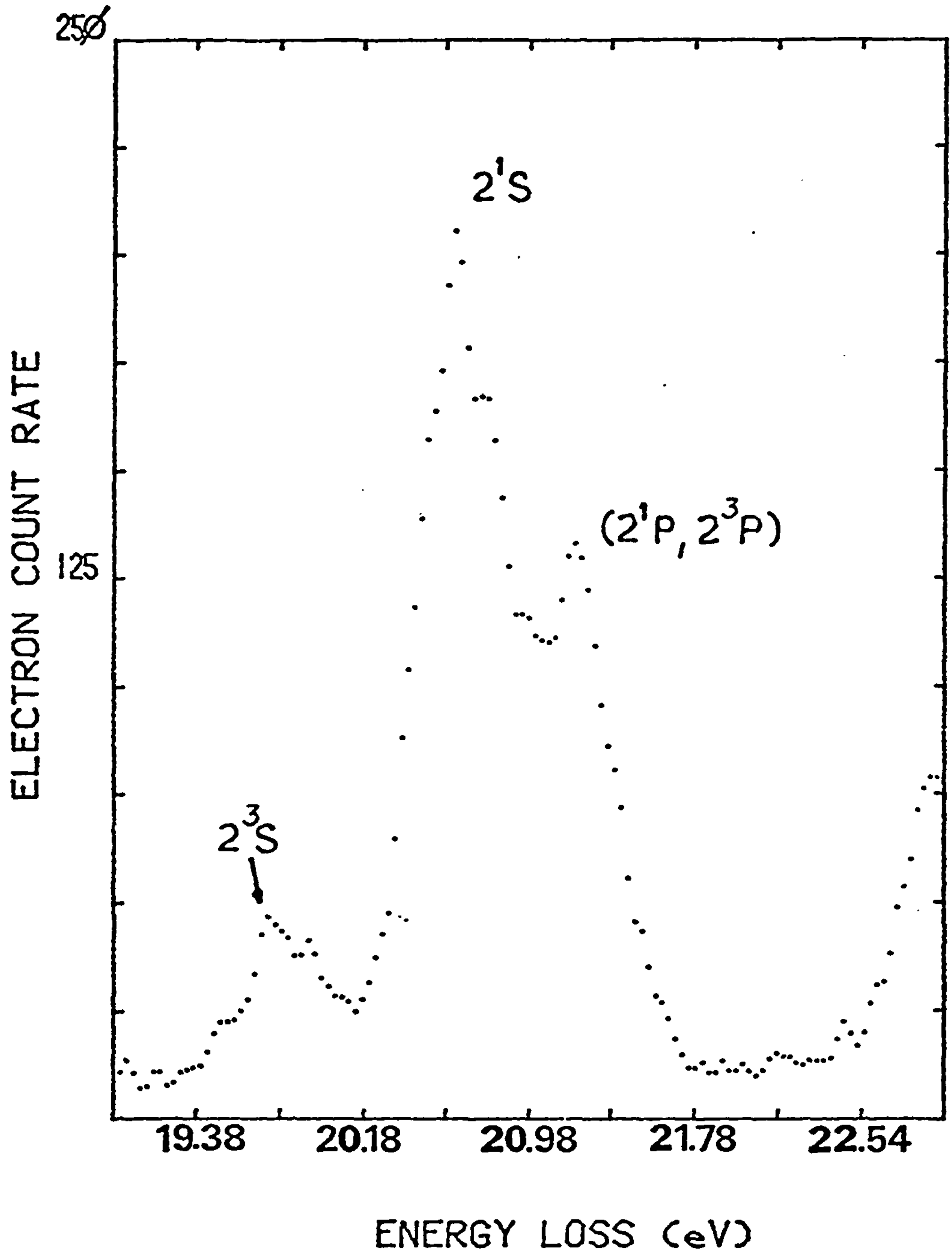

Fig. 13b. Energy loss spectrum for θ_e = 90 . (2^3P is a negligible component.)

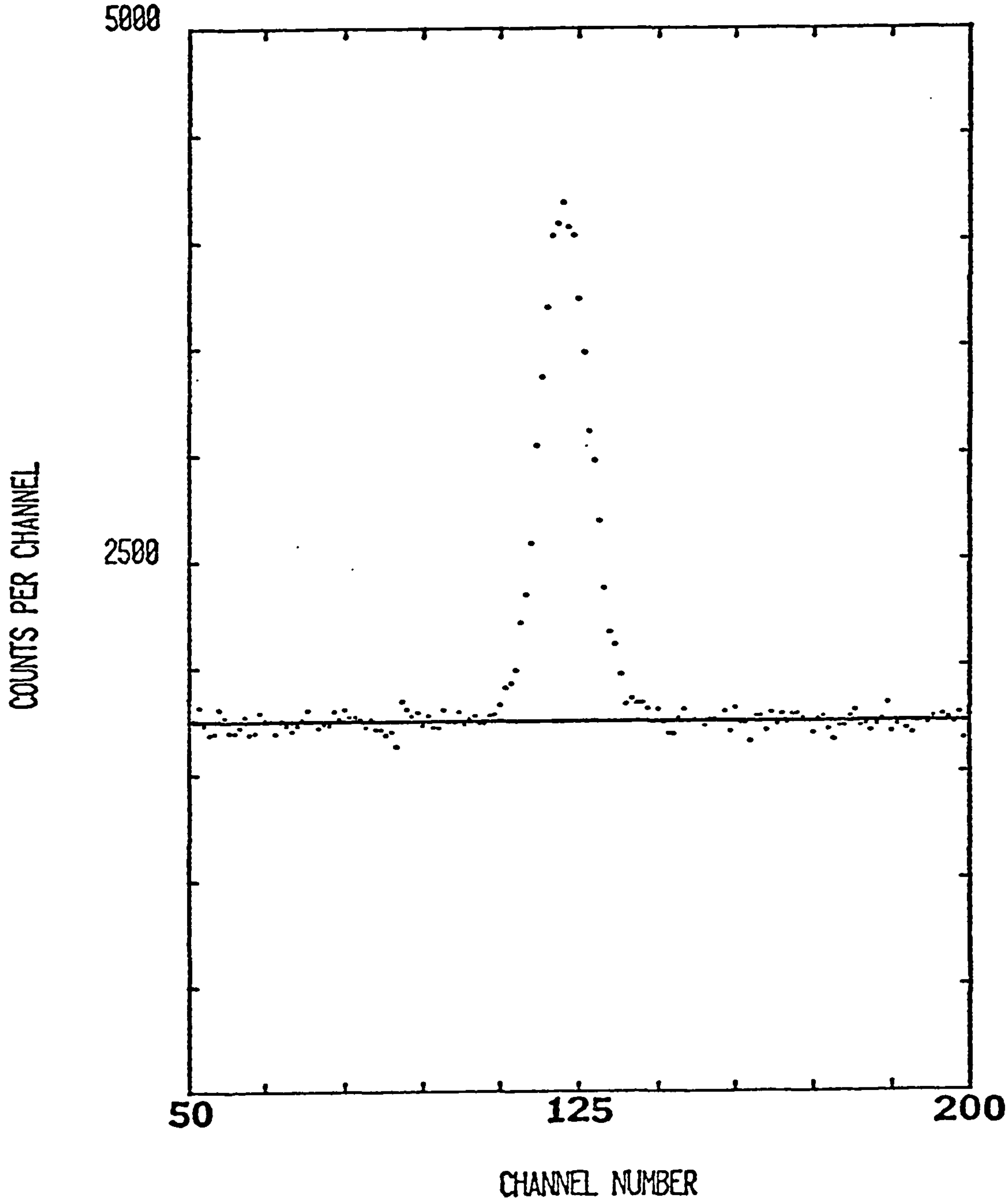

Fig. 14. Delayed coincidence spectrum for an electron energy of 80 eV, $\theta_e = 5^o$, $\theta_\gamma = 90^o$. The TAC was started on electrons. Accumulation time $\sim$11 hrs., channel width 0.967 nsec, $R_e \sim 9.5$ kHz, $I_e \sim 1.1$ μA, background pressure $\sim 3.5 \times 10^{-7}$ Torr. Linear least-squares fit to the background has a slope of -0.021 and an intercept of 1741.4; $N_c = 28{,}400 \pm 280$. The total number of electrons detected was 3.76×10^8; $N_e = 3.53 \times 10^8$. $R_\gamma \sim 4.2$ kHz.

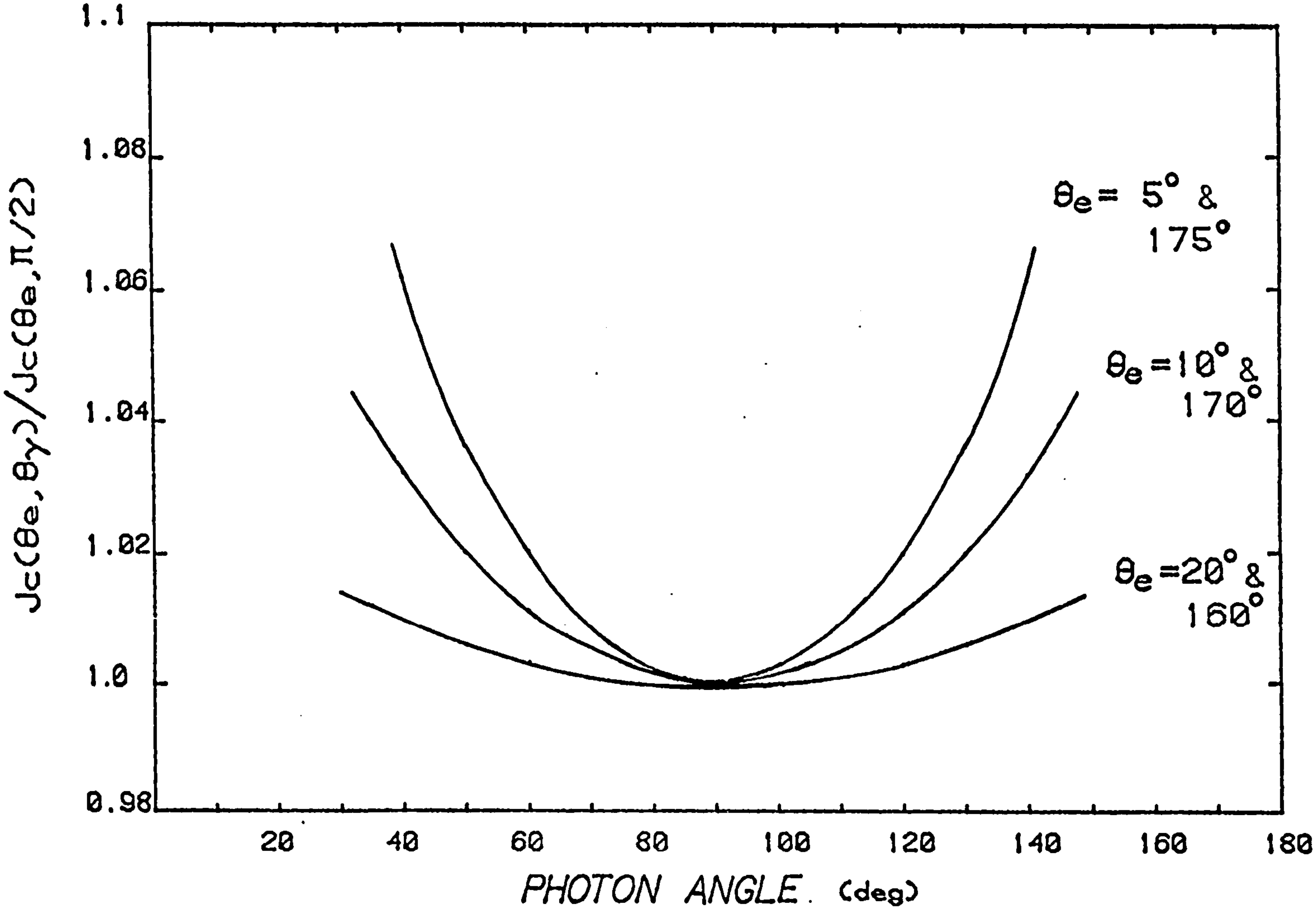

Fig. 15. Multiplicative factor $J_c(\theta_e,\theta_\gamma)/J_c(\theta_e,\pi/2)$. This factor accounts for scattering from both beam and background helium.

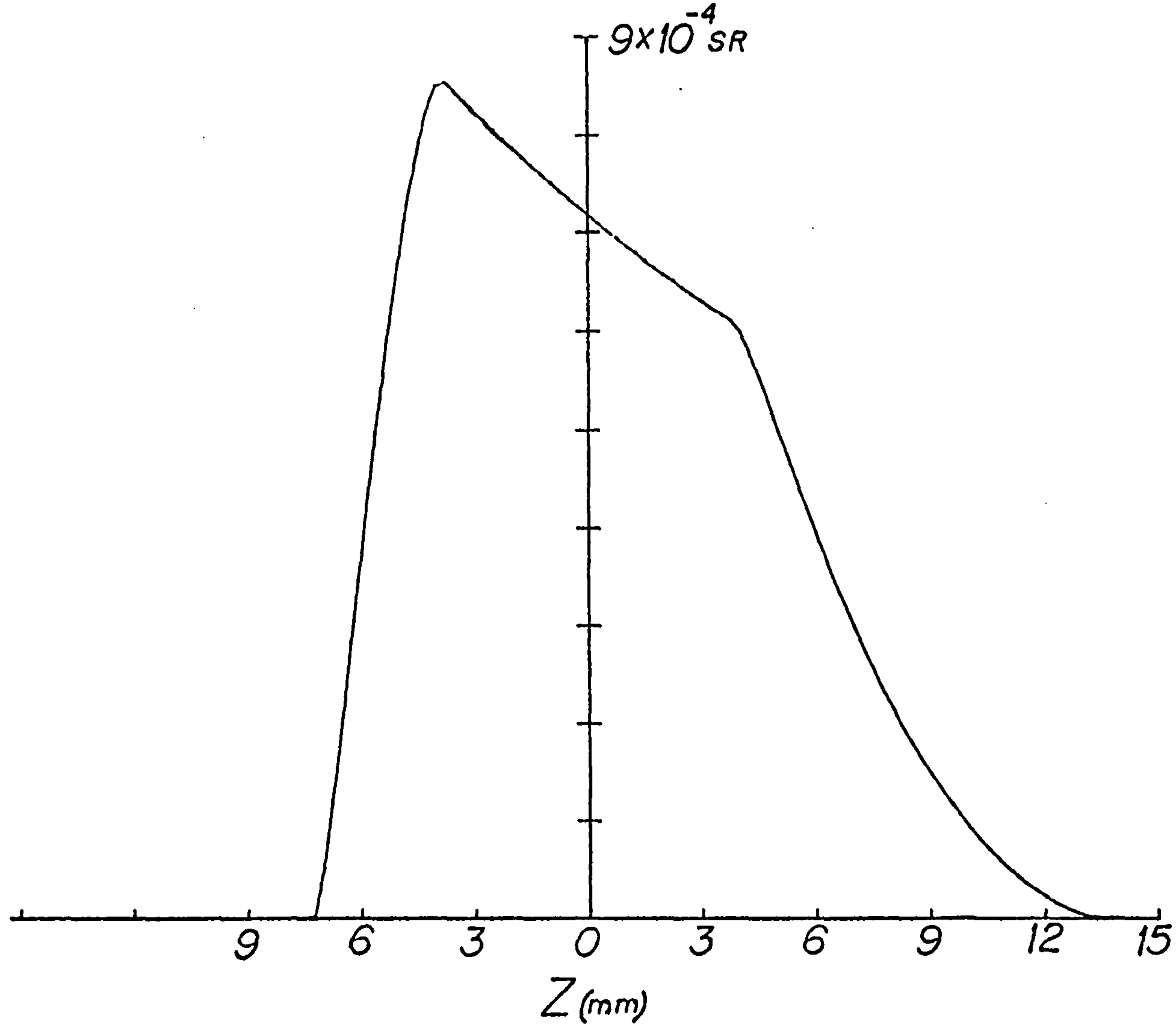

Fig. 16a. $\Delta\Omega_e(z, 10°)$

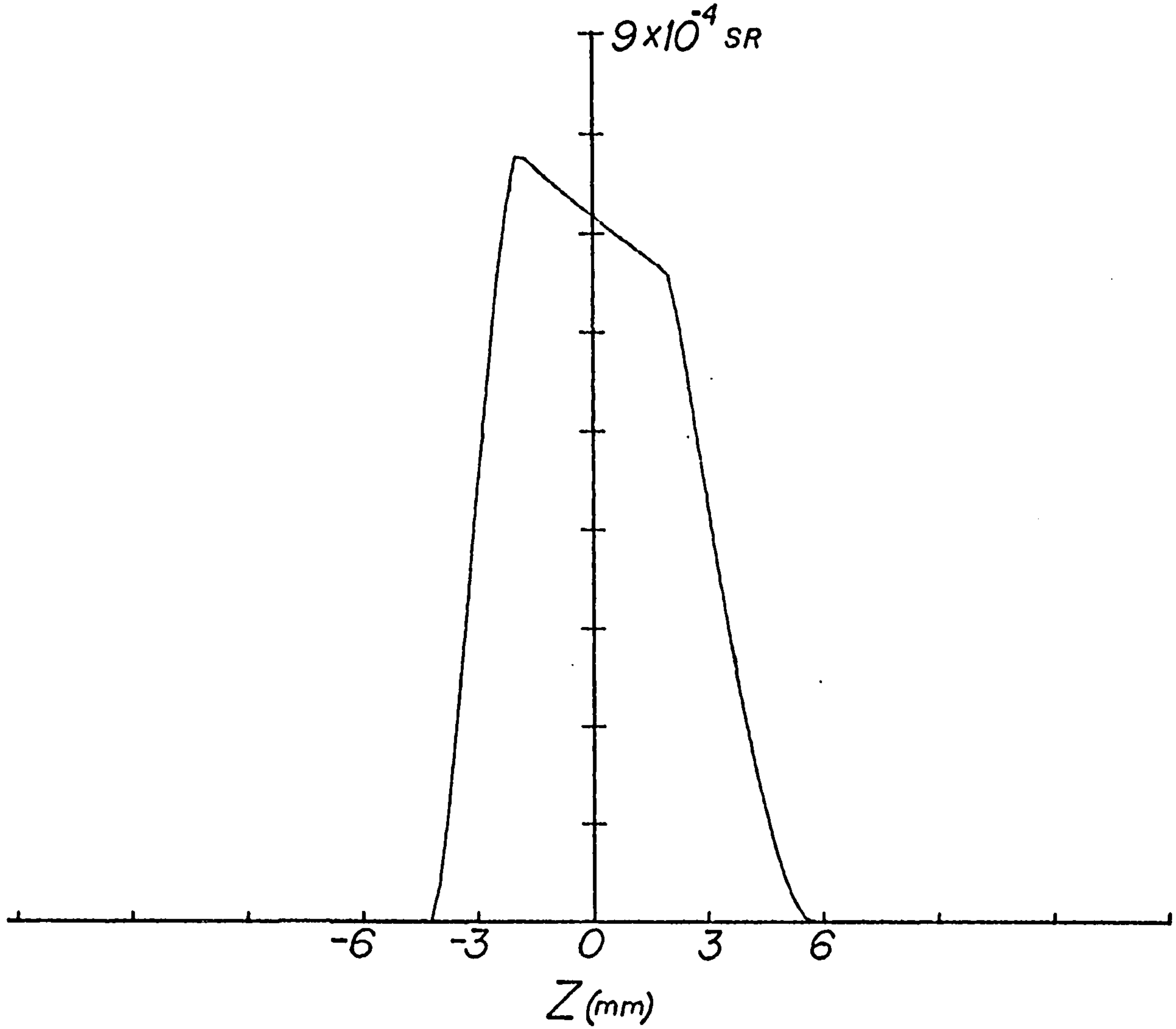

Fig. 16b. $\Delta\Omega_e(z, 20^\circ)$

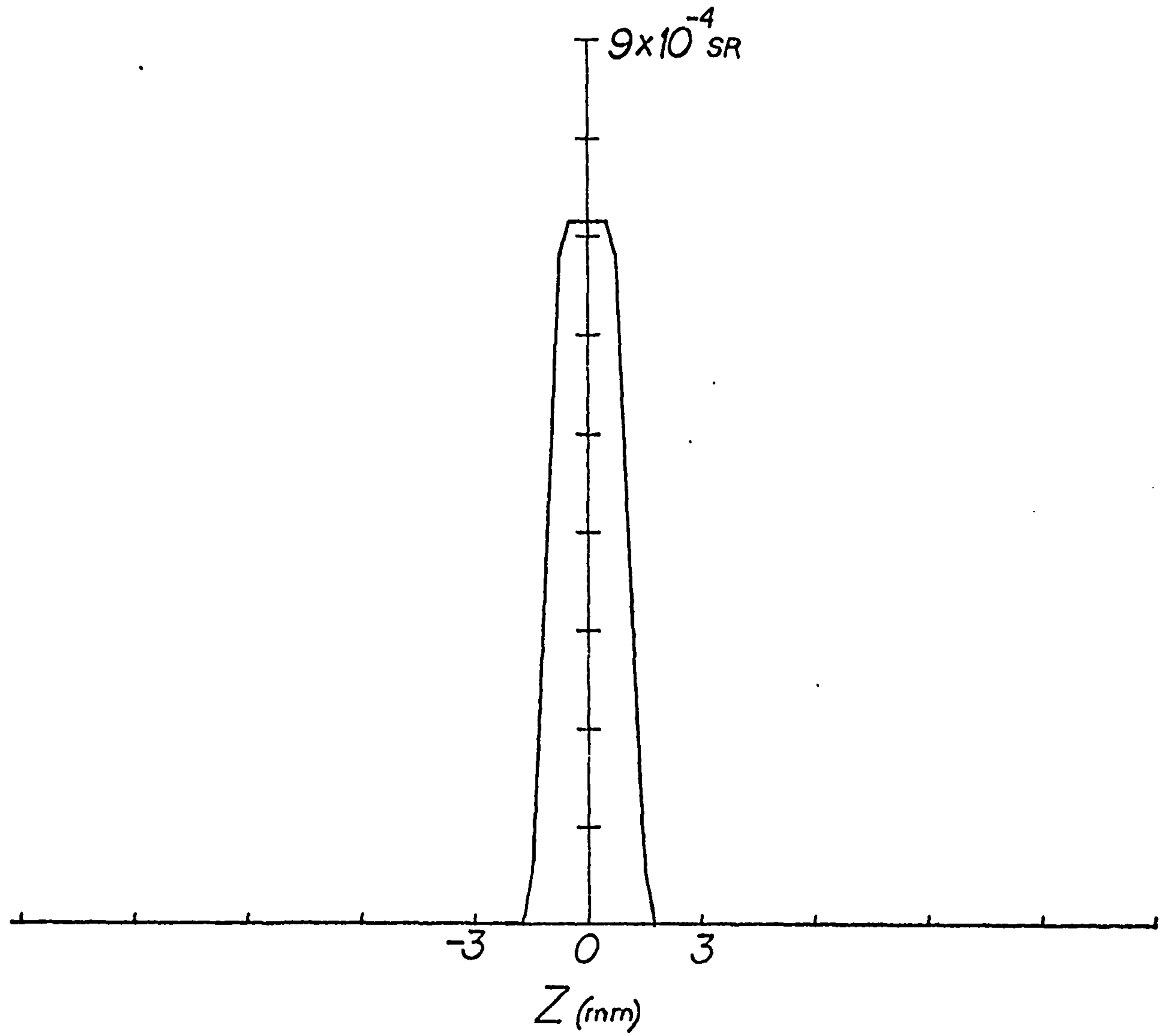

Fig. 16c. $\Delta\Omega_e(z,90°)$

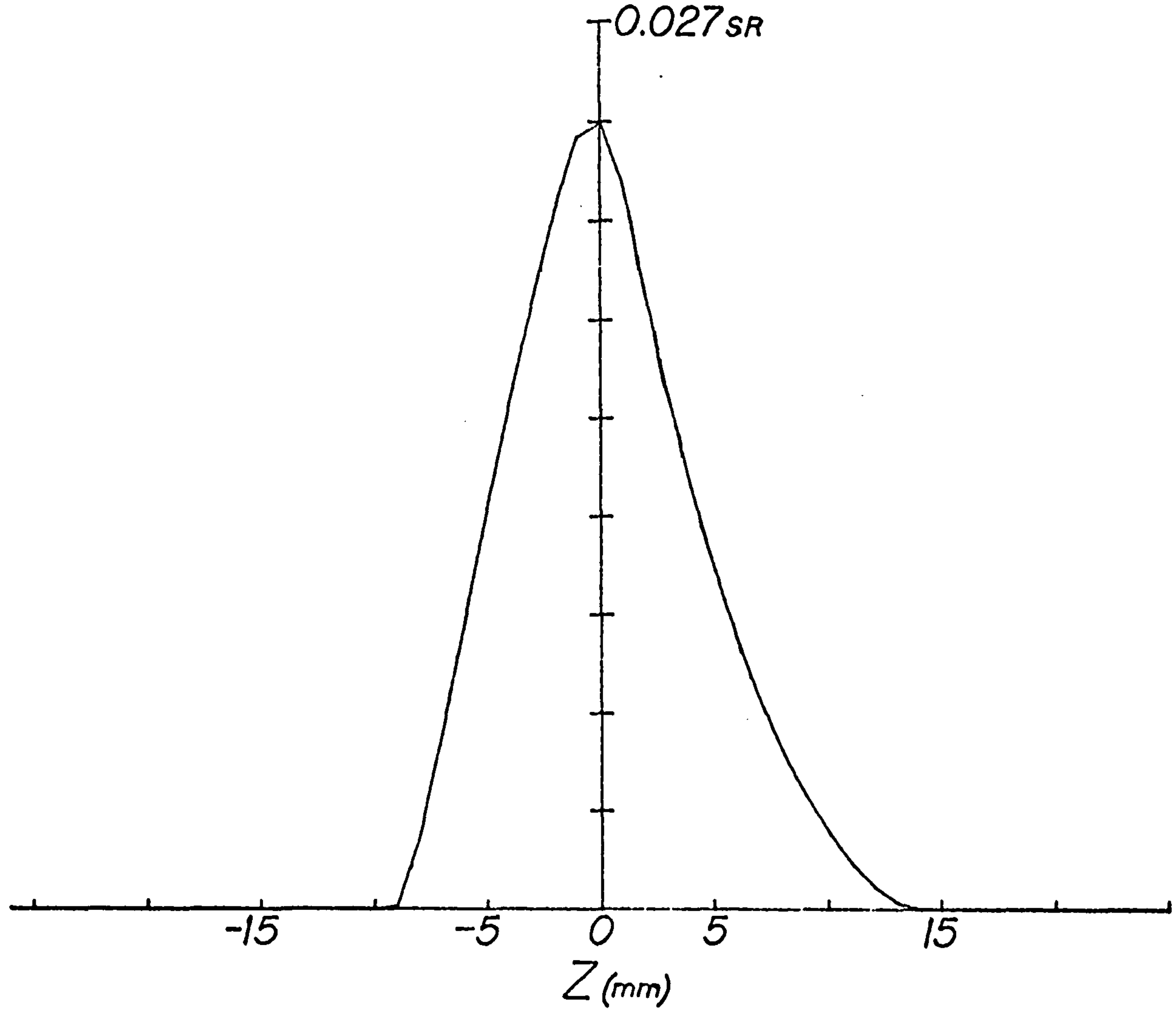

Fig. 16d. $\Delta\Omega_{\gamma}(z, 50°)$

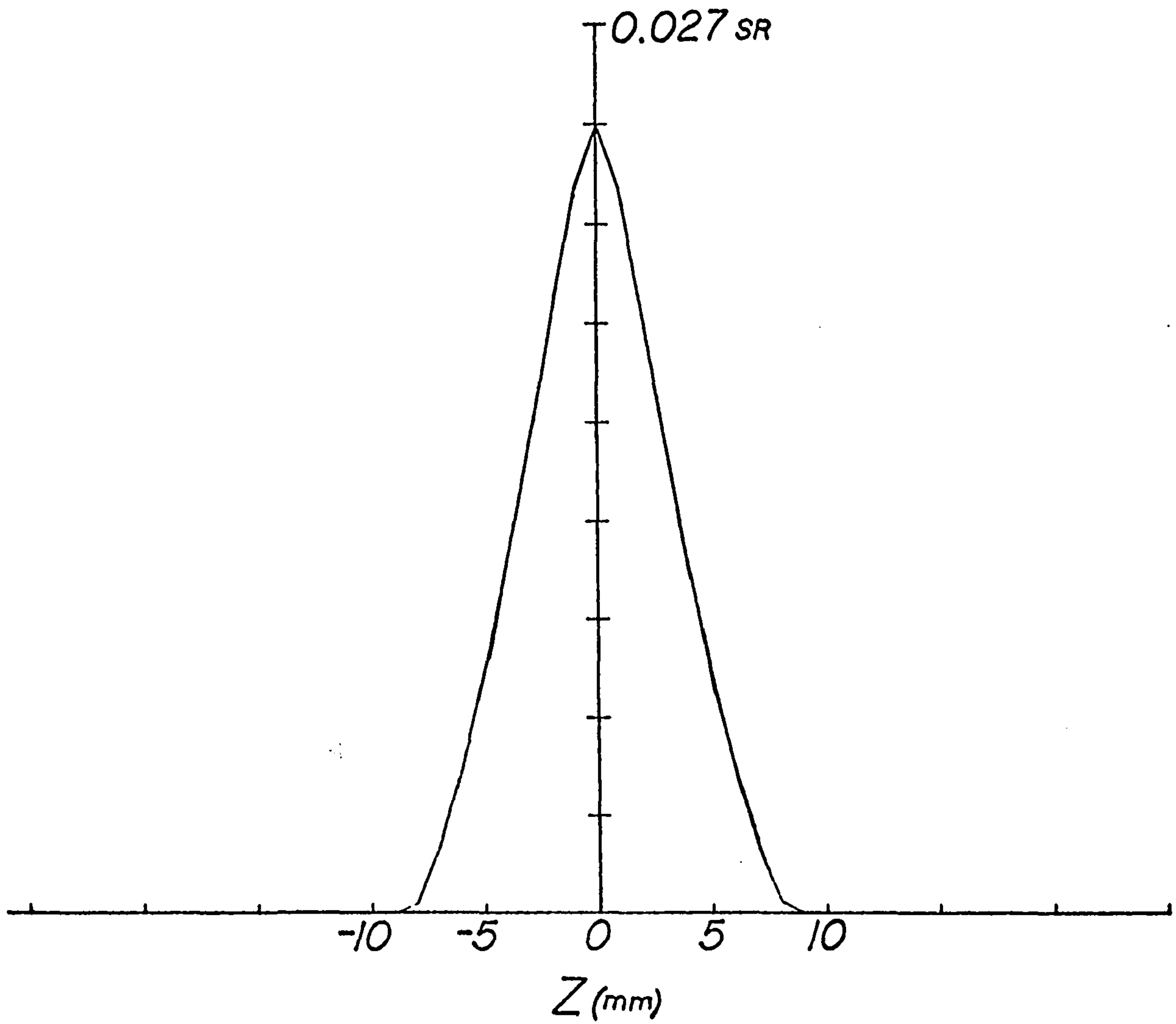

Fig. 16e. $\Delta\Omega_{\gamma}(z,90^{\circ})$

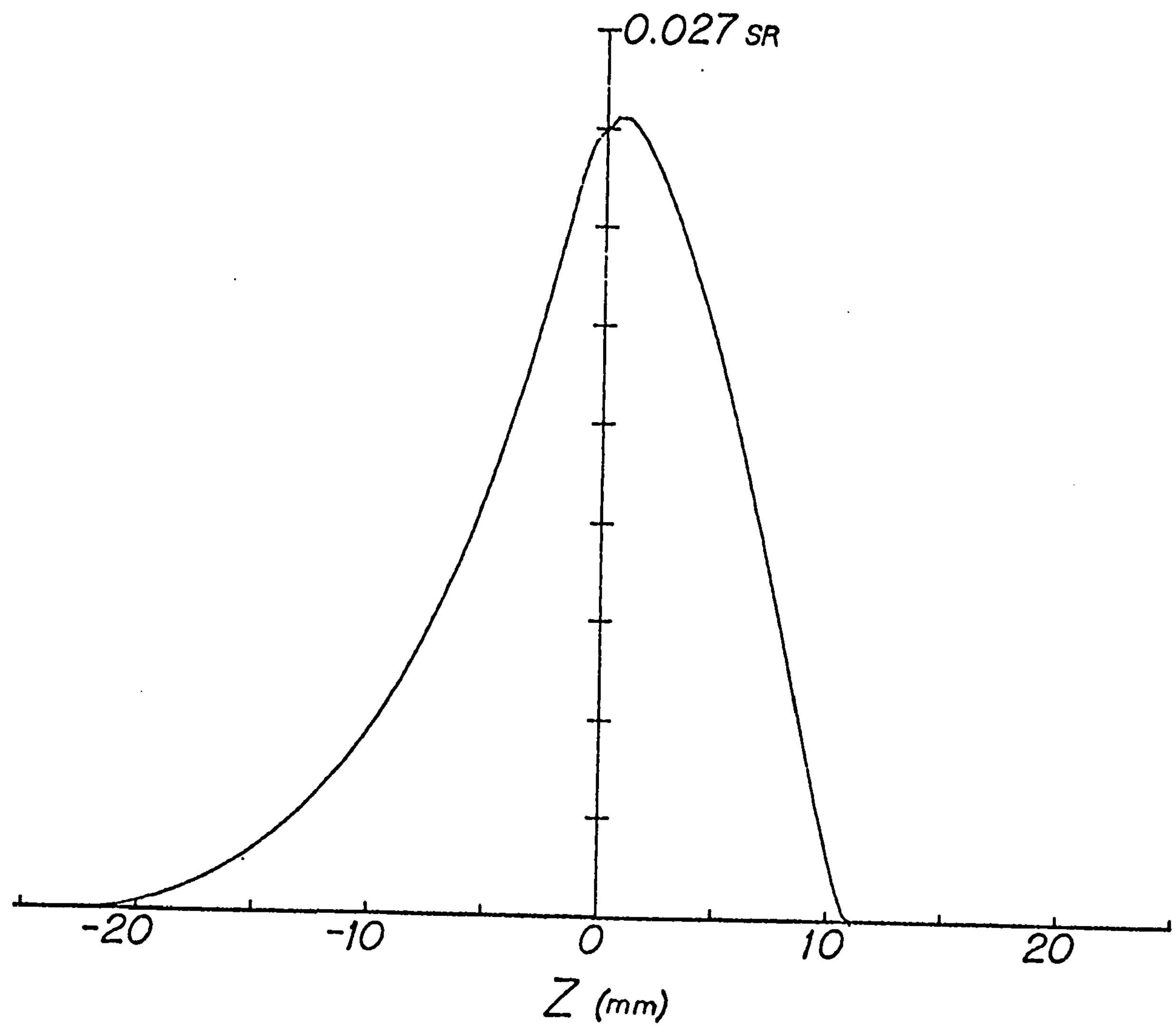

Fig. 16f. $\Delta\Omega_{\gamma}(z,145^{\circ})$

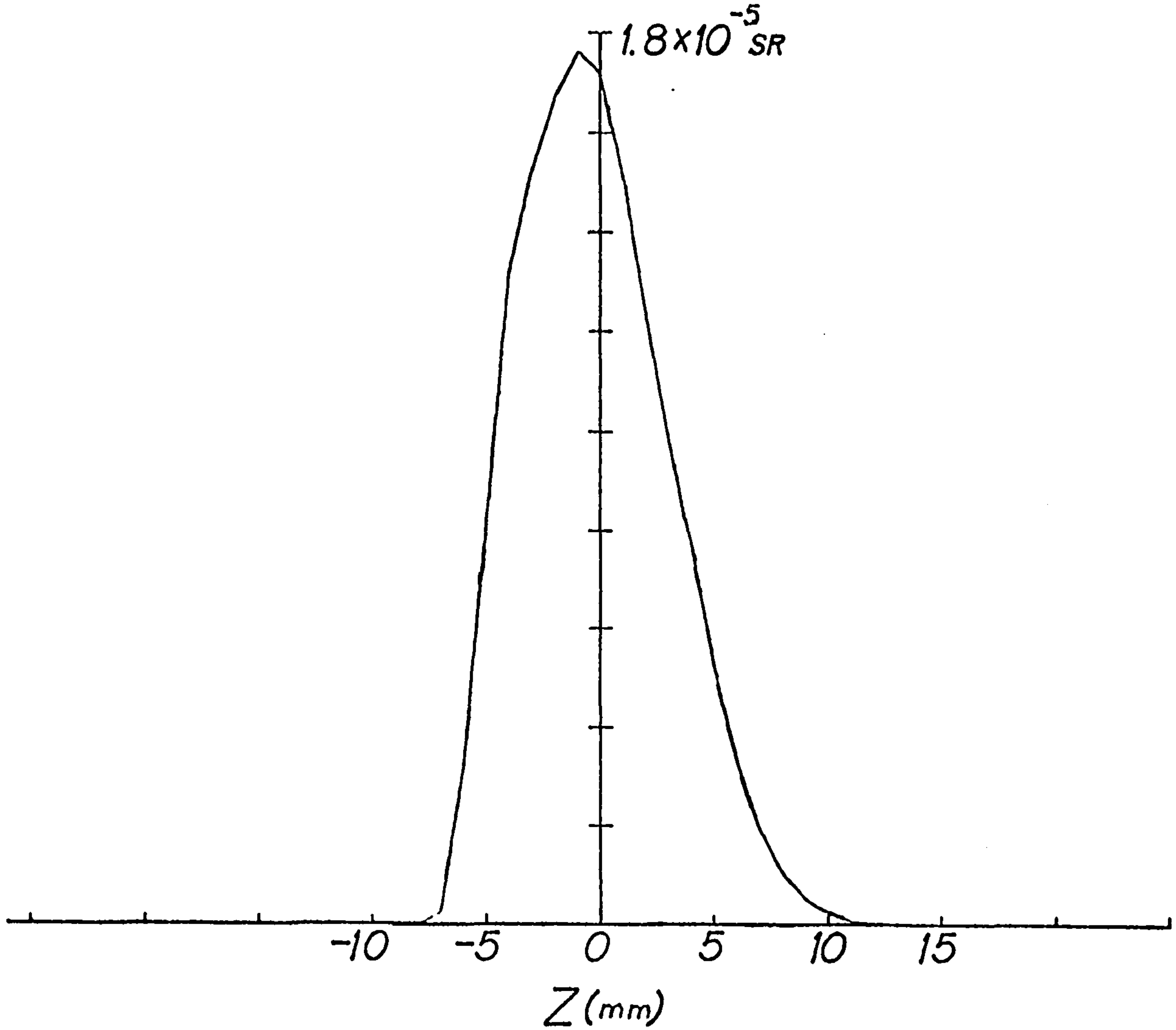

Fig. 16g. $\Delta\Omega_e(z,10^\circ)\Delta\Omega_\gamma(z,50^\circ)$

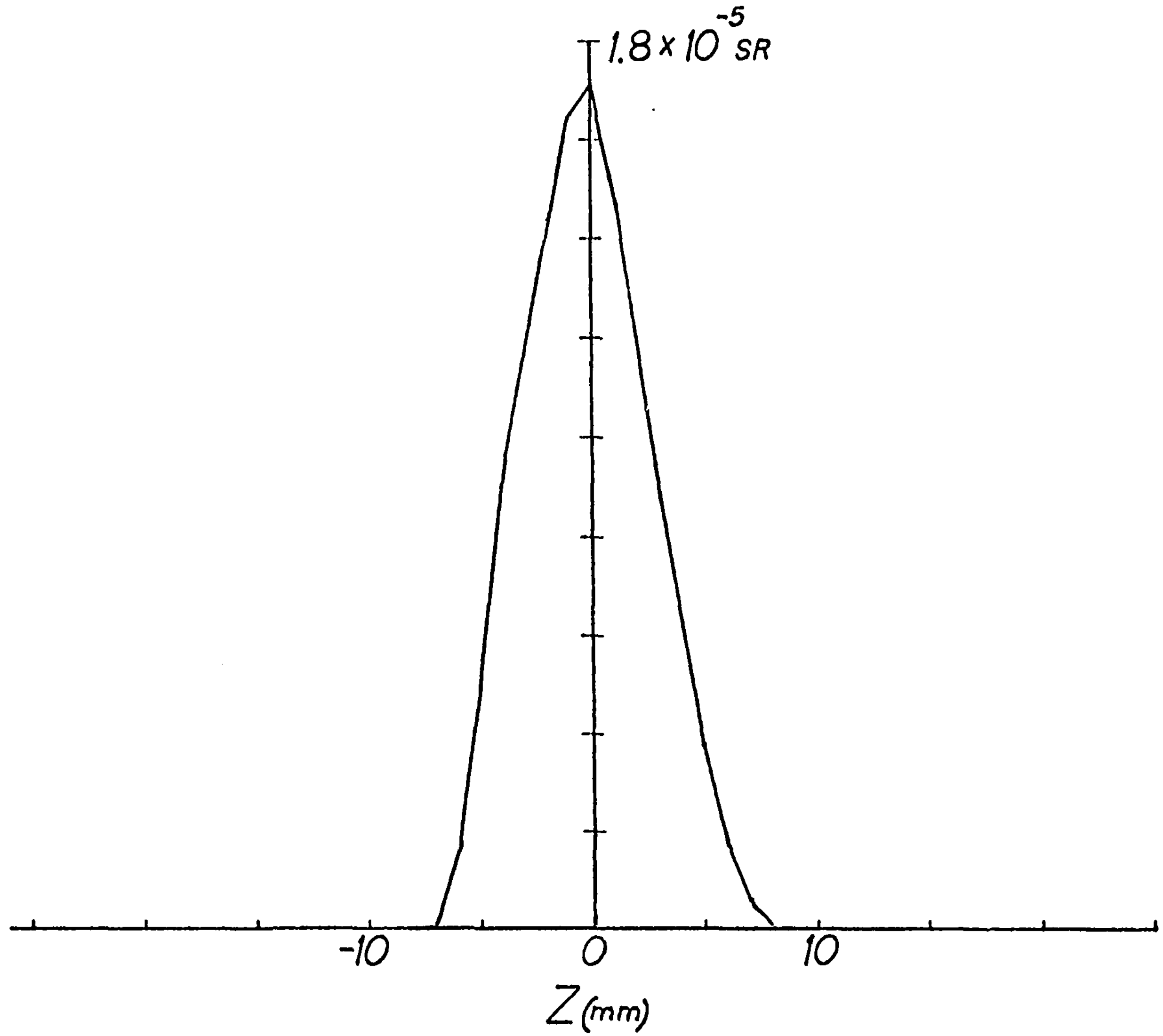

Fig. 16h. $\Delta\Omega_e(z,10^\circ)\Delta\Omega_\gamma(z,90^\circ)$

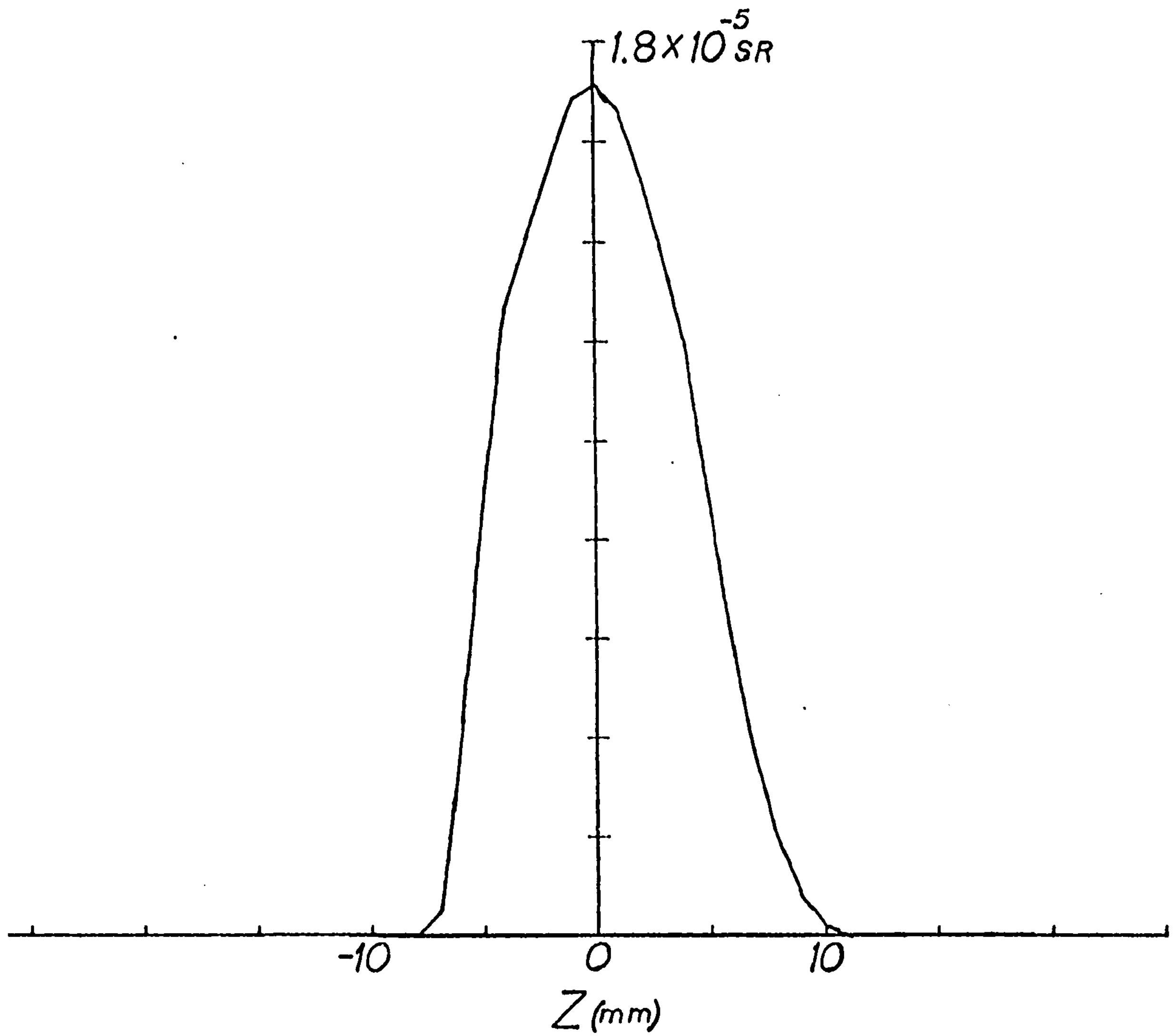

Fig.16i. $\Delta\Omega_e(z,10^\circ)\Delta\Omega_\gamma(z,145^\circ)$

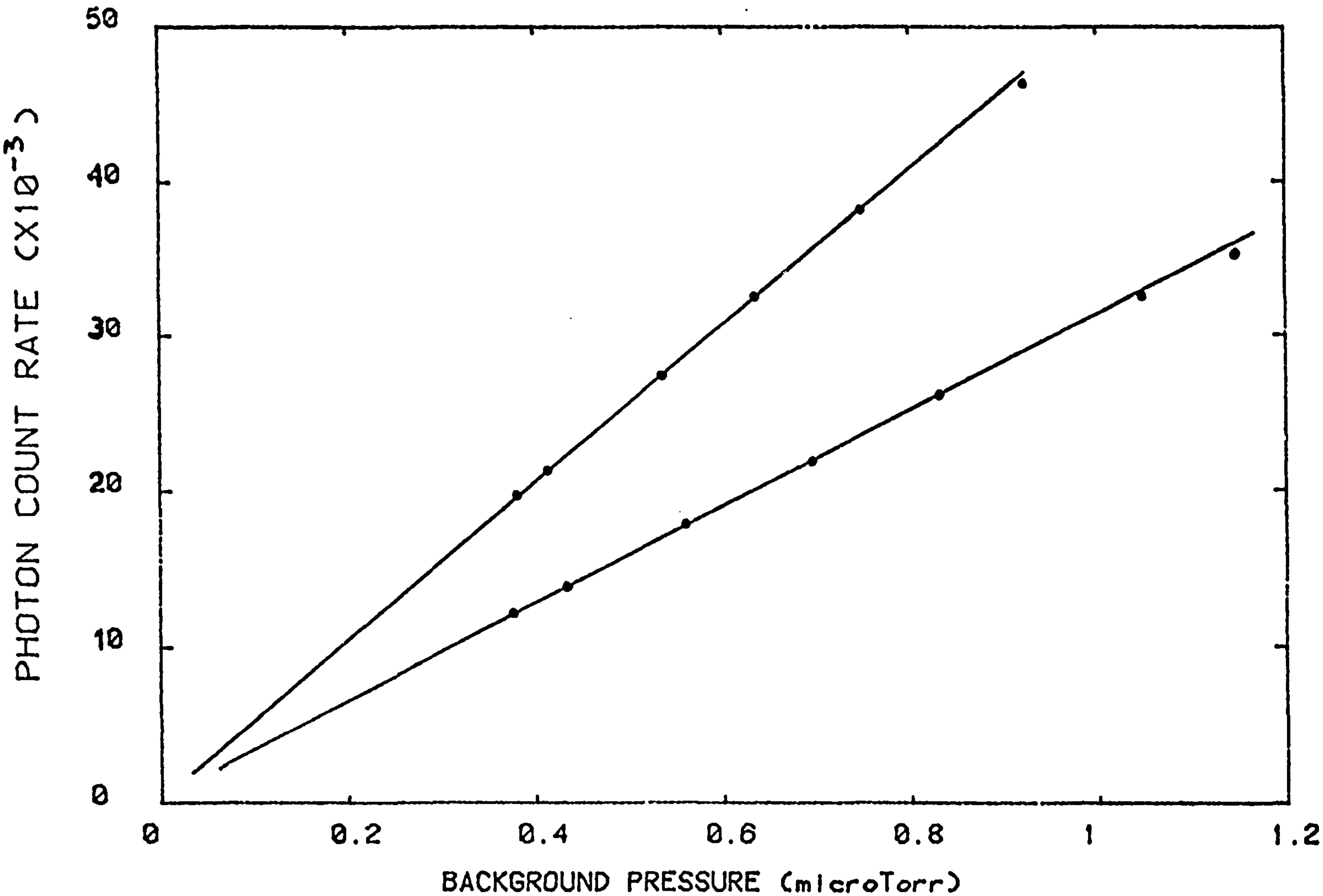

Fig. 17. The pressure dependence of the photon count rate for two values of ε_γ. The curves are linear up to a background pressure of 1 μTorr.

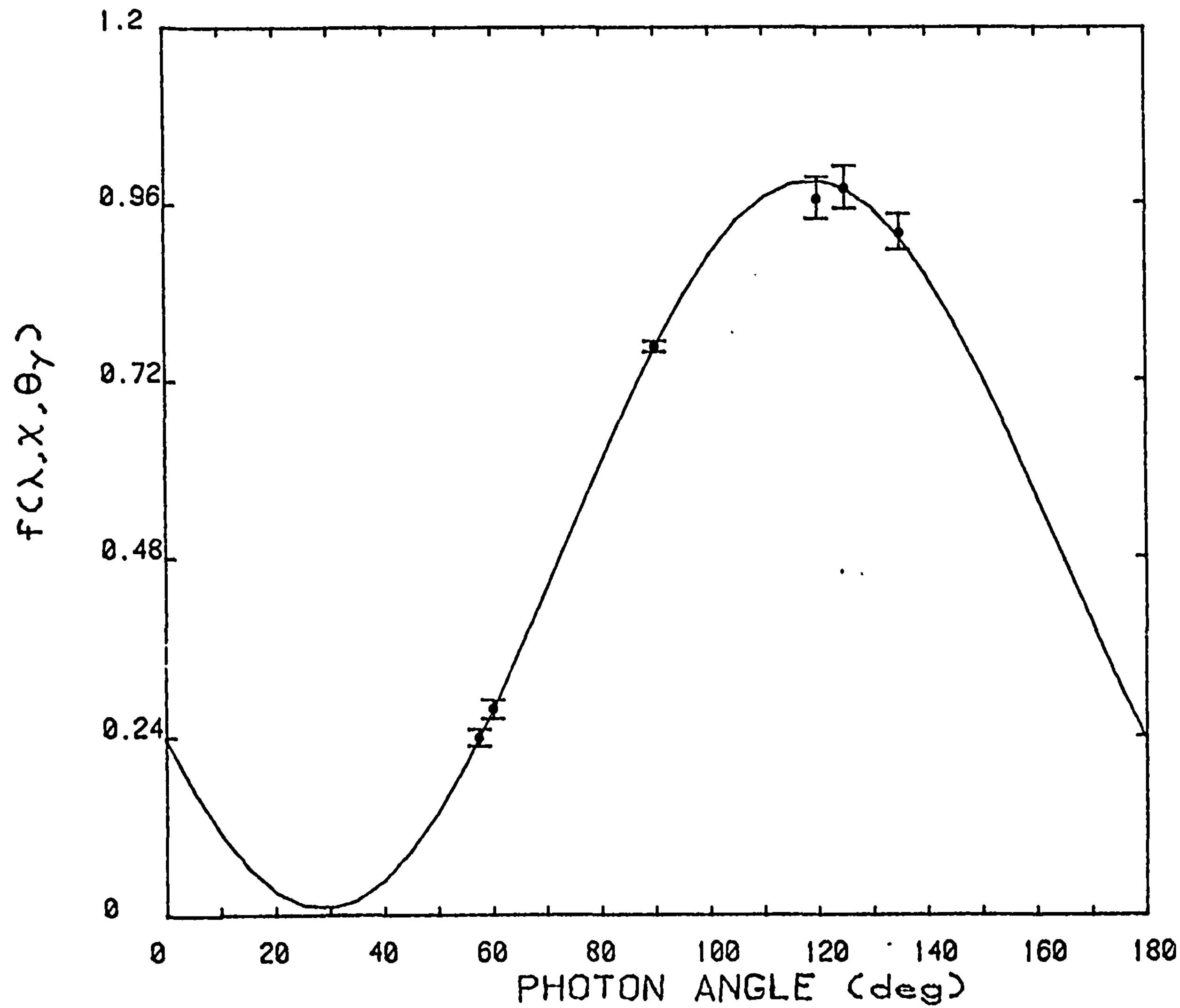

Fig. 18a. Measured Angular correlation for electron angle 5 deg.

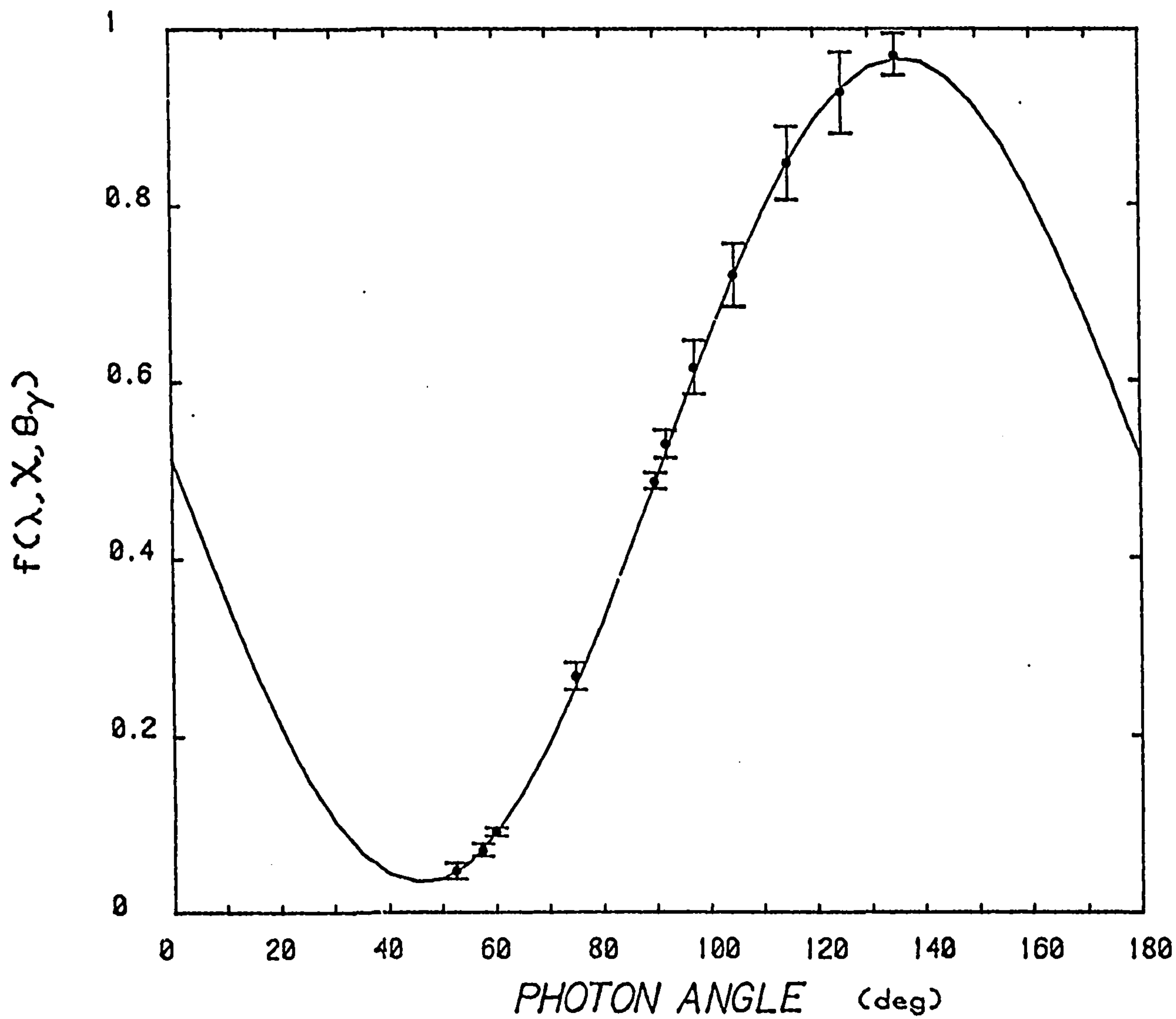

Fig. 18b. Measured angular correlation for electron angle 10 deg.

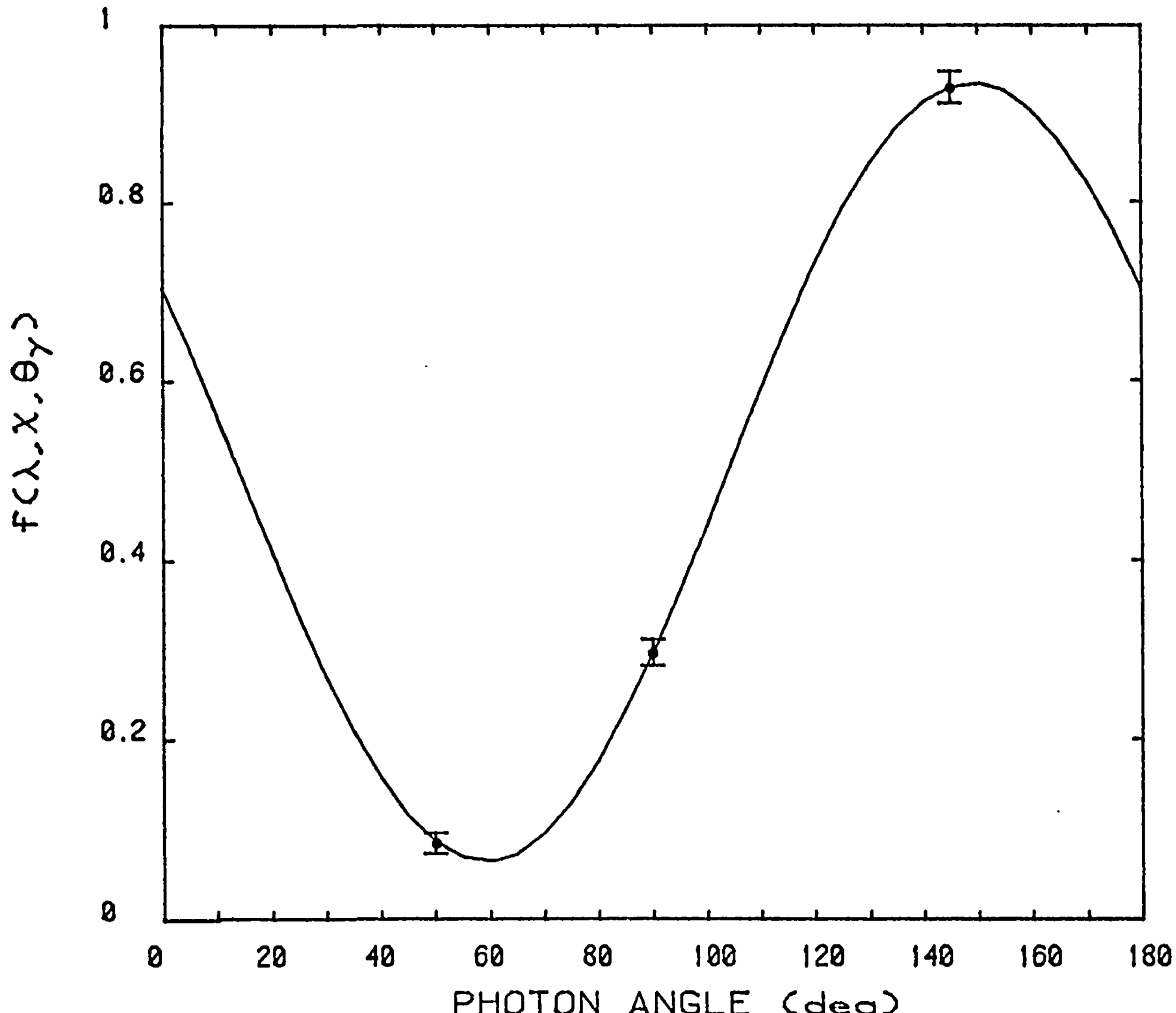

Fig. 18c. Measured angular correlation function for electron angle 20 deg.

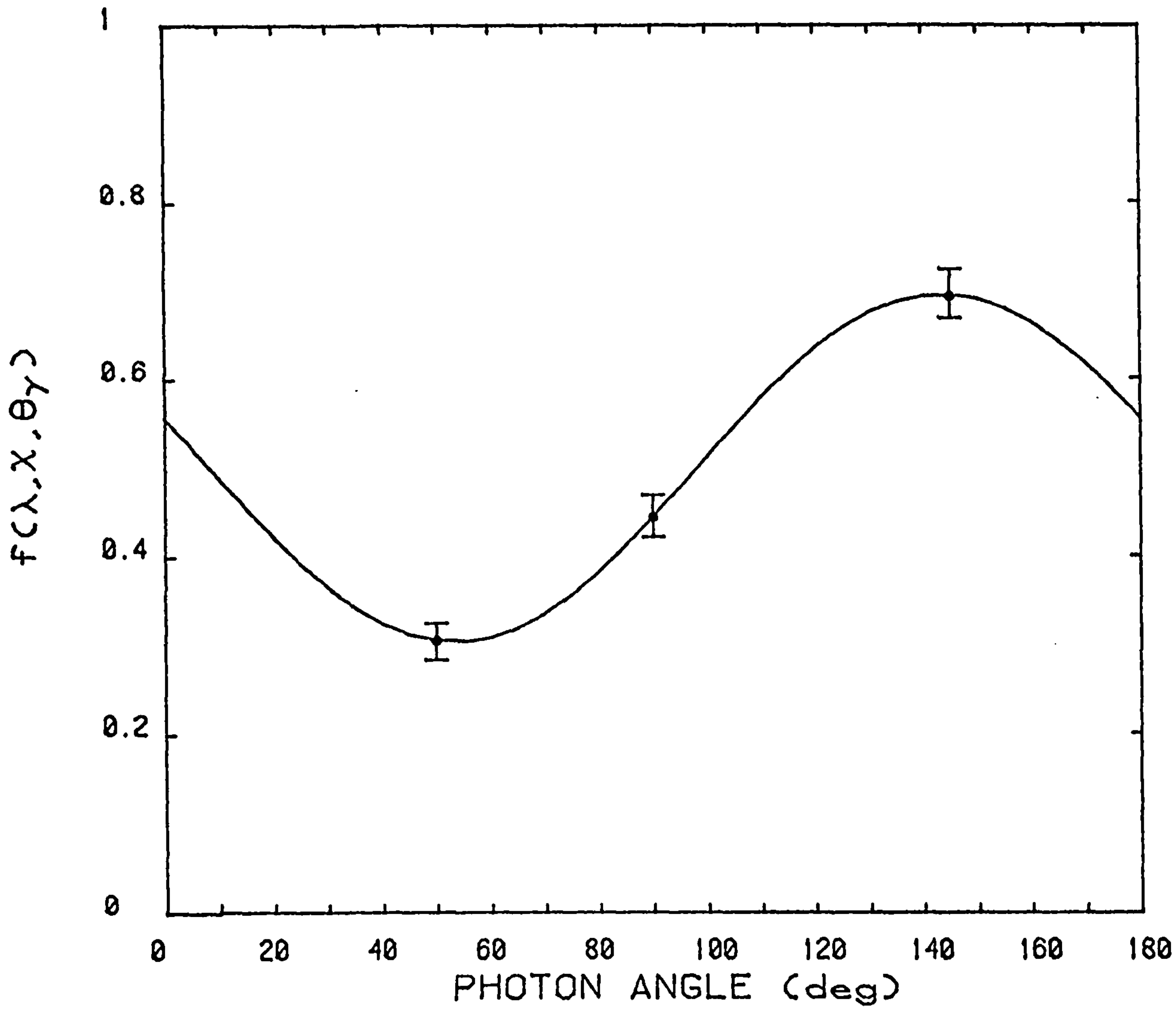

Fig. 18d. Measured angular correlation function for electron angle 30 deg.

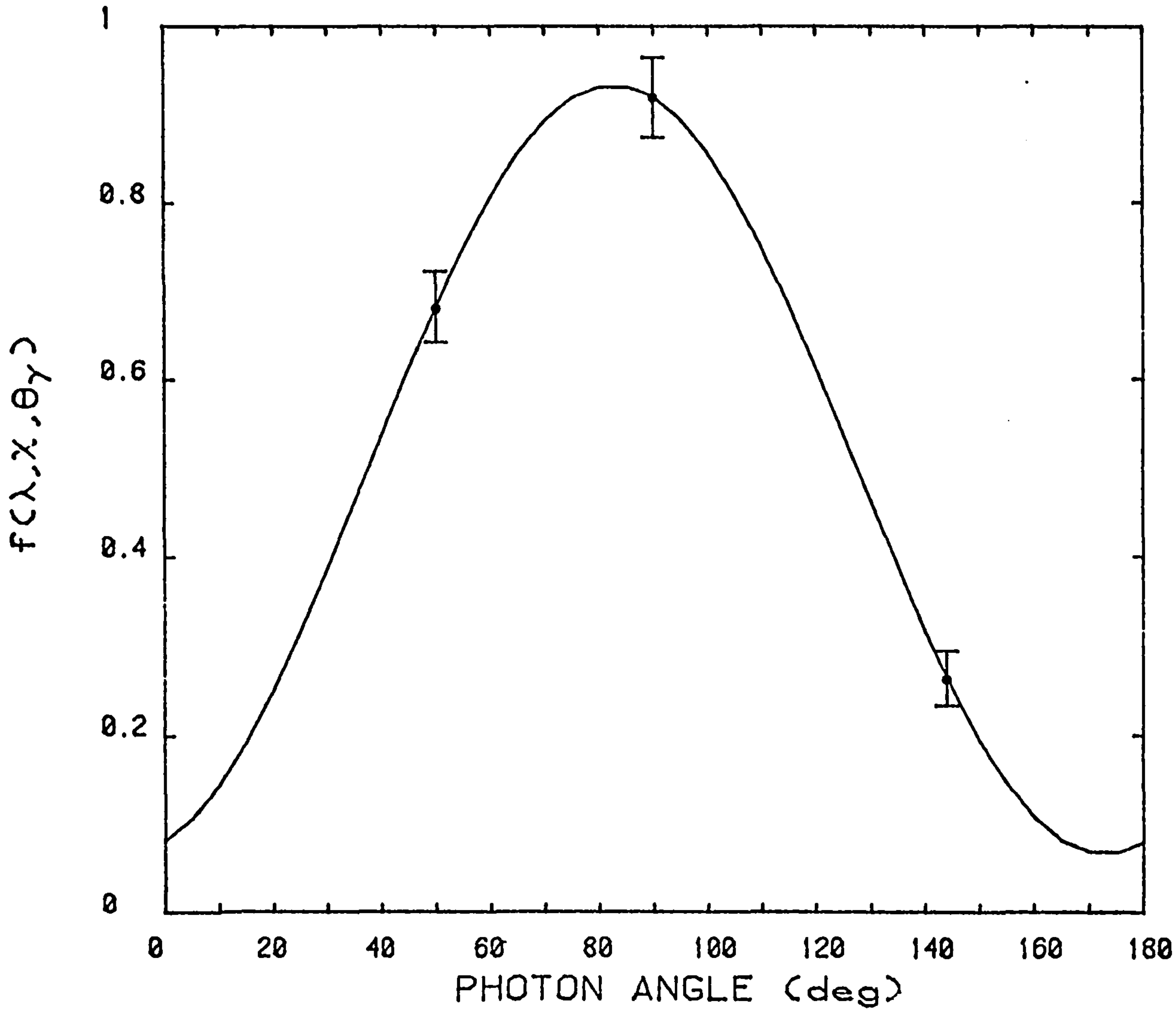

Fig. 18e. Measured angularcorrelation for electron angle 50 deg.

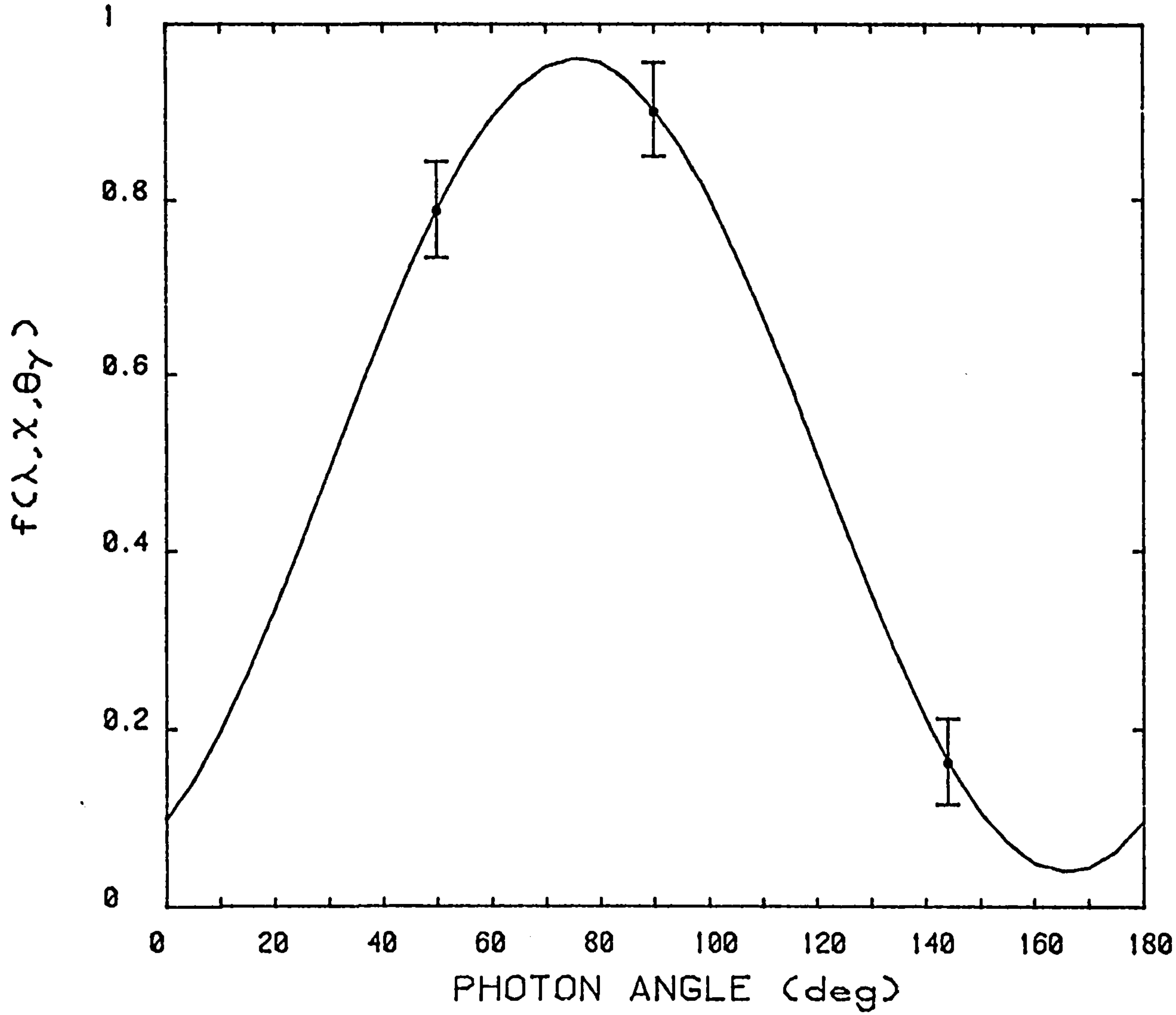

Fig. 18f. Measured angular correlation for electron angle 60 deg.

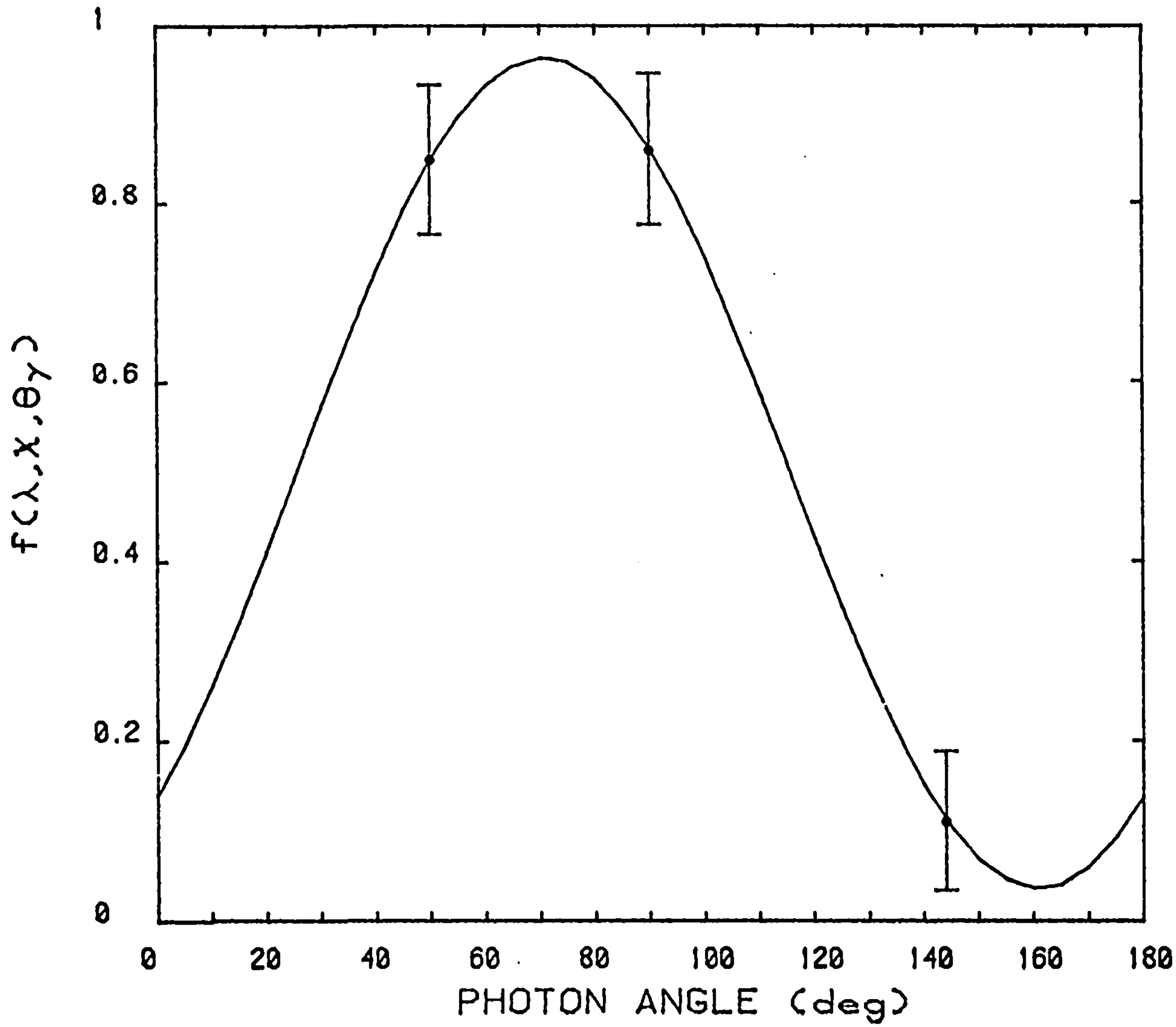

Fig. 18g. Measured angular correlation function for electron angle 80 deg.

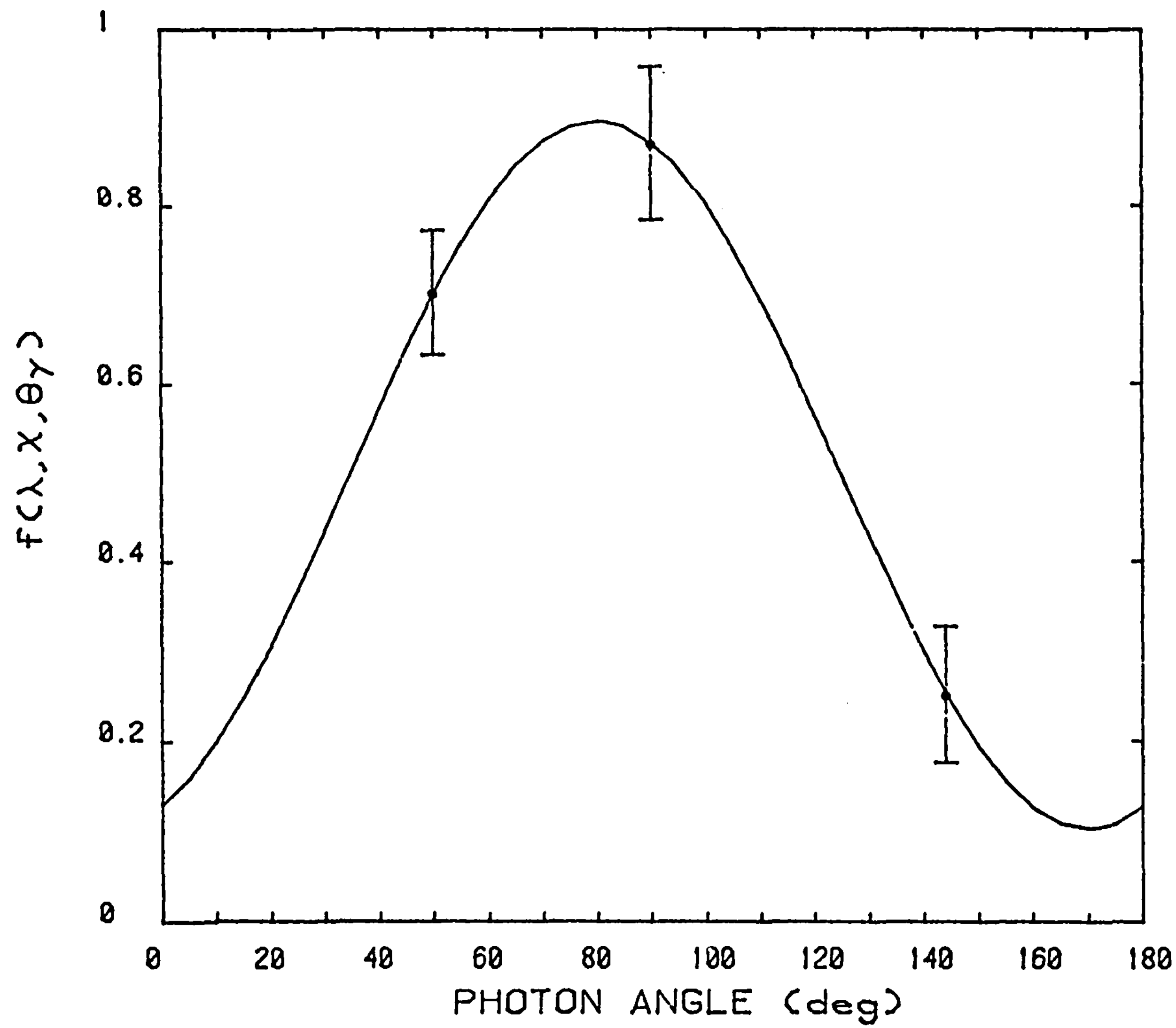

Fig. 18h. Measured angular correlation function for electron angle 90 deg.

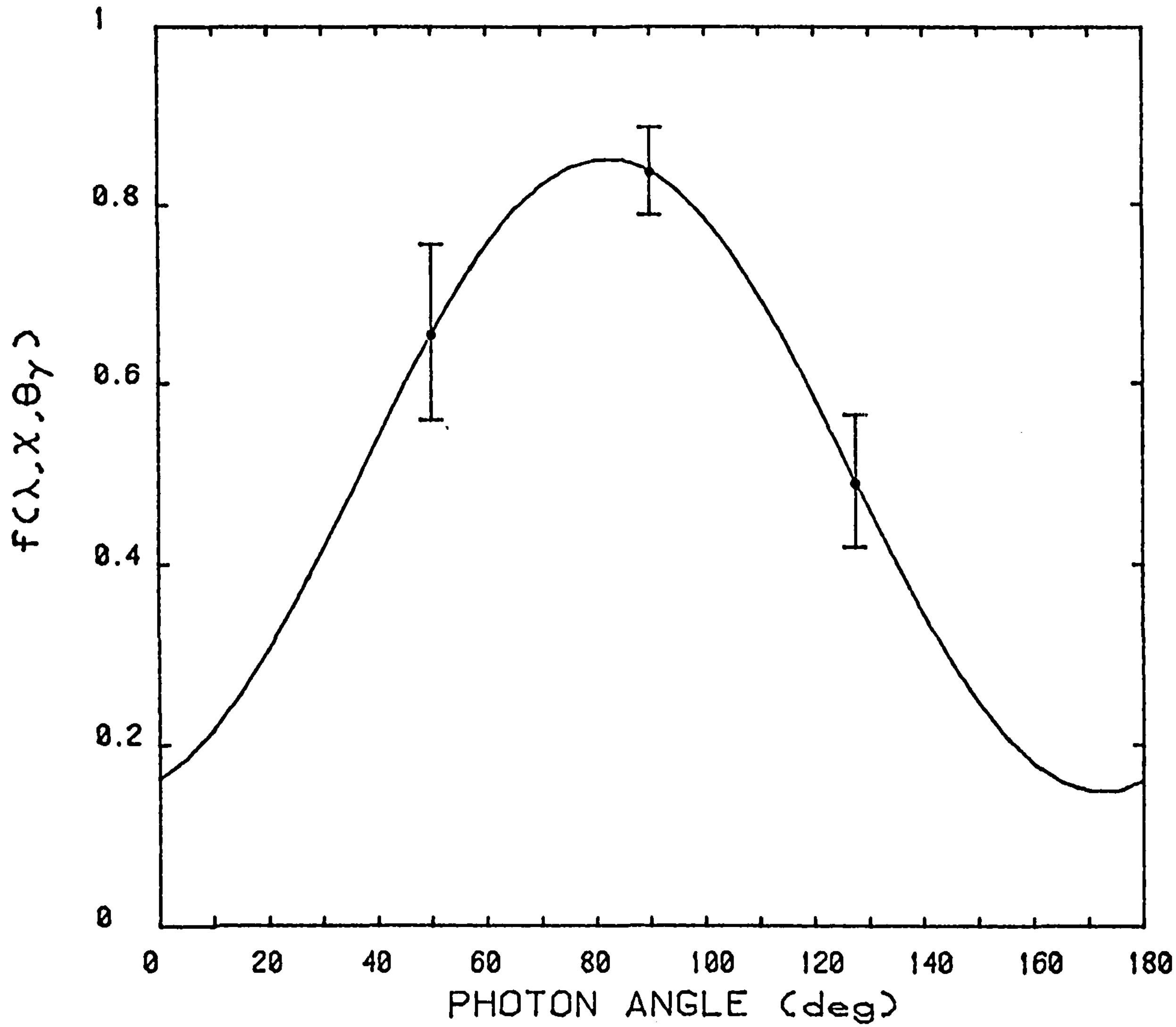

Fig. 18i. Measured angular correlation function for electron angle 100 deg.

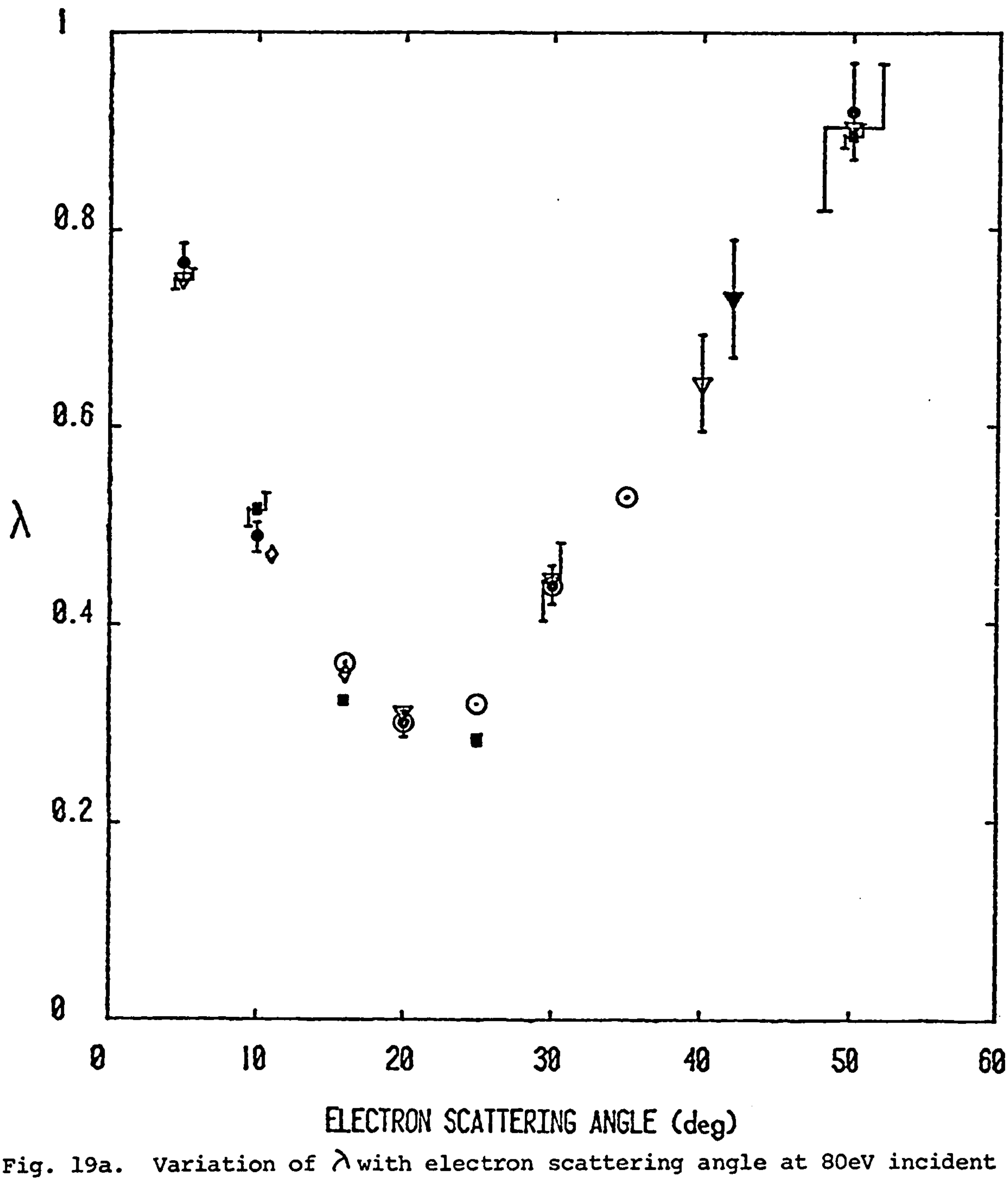

Fig. 19a. Variation of λ with electron scattering angle at 80eV incident energy. ● , present data; ⊙, results of Ref. 20; ◇, results of Ref. 21; ▼, results of Ref. 22; ▽, results of Ref. 23; ■, results of Ref. 24.

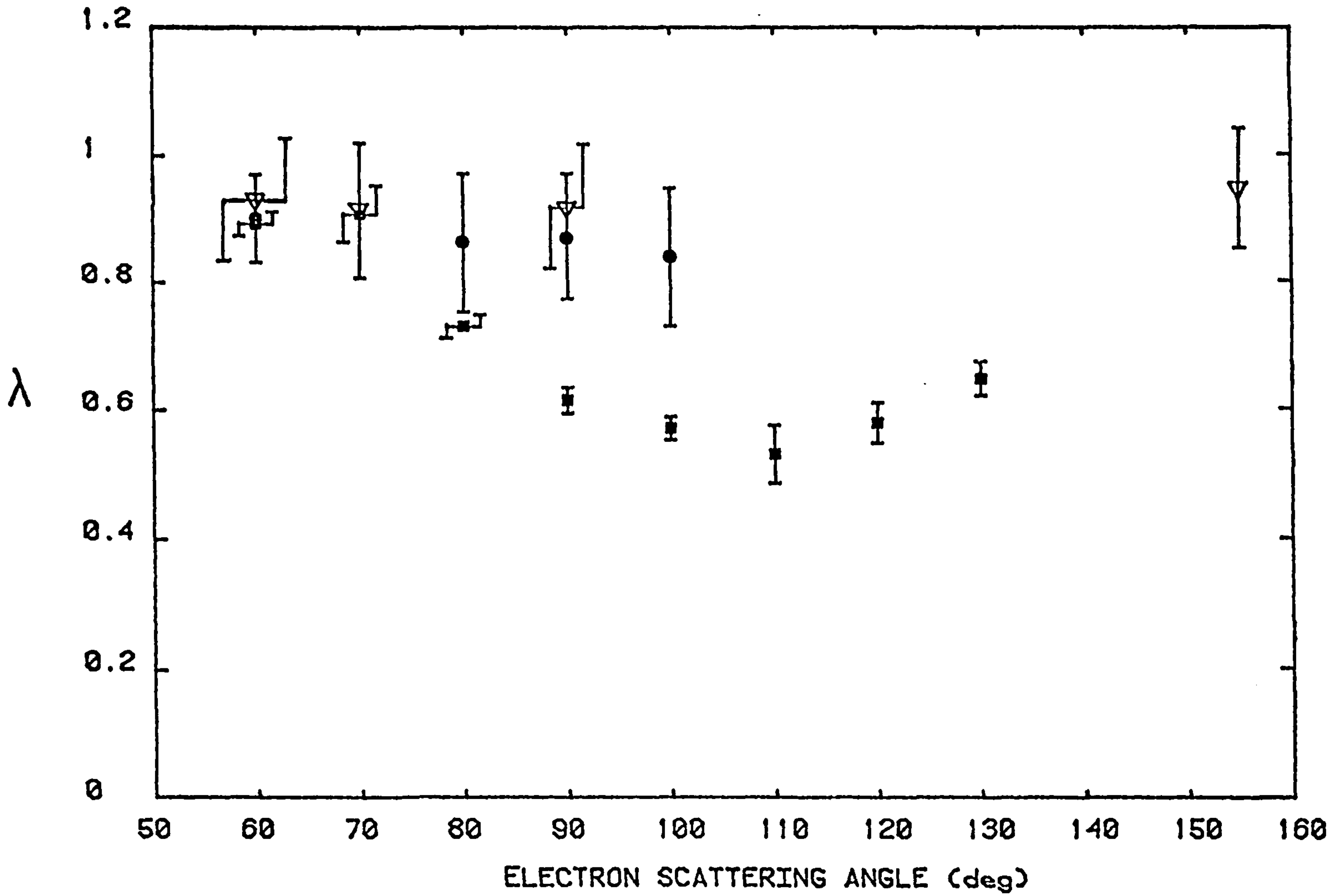

Fig. 19b. Variation of λ with electron scattering angle at 80eV incident energy. ●, present data; ▽, results of Ref. 23; ■, results of Ref. 24.

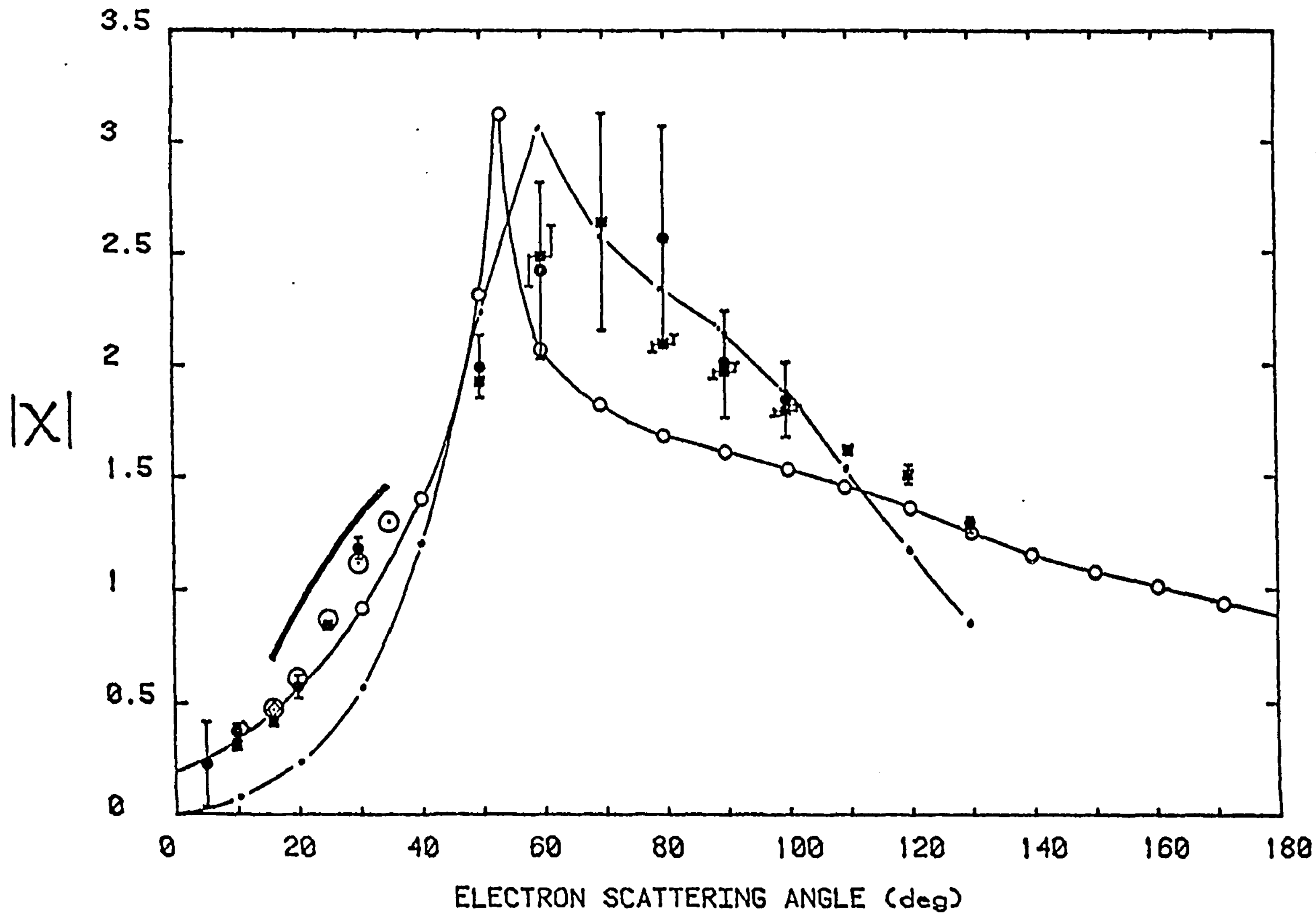

Fig. 20. Variation of $|\gamma|$ with electron scattering angle for an incident energy of 80 eV. ● , present data; ⊙, results of Ref. 20; ◇, results of Ref. 21; ▬, calculation Ref. 25; ■, results of Ref. 24; —·—, calculation of Ref. 28; —O—, calculation of Ref. 31.

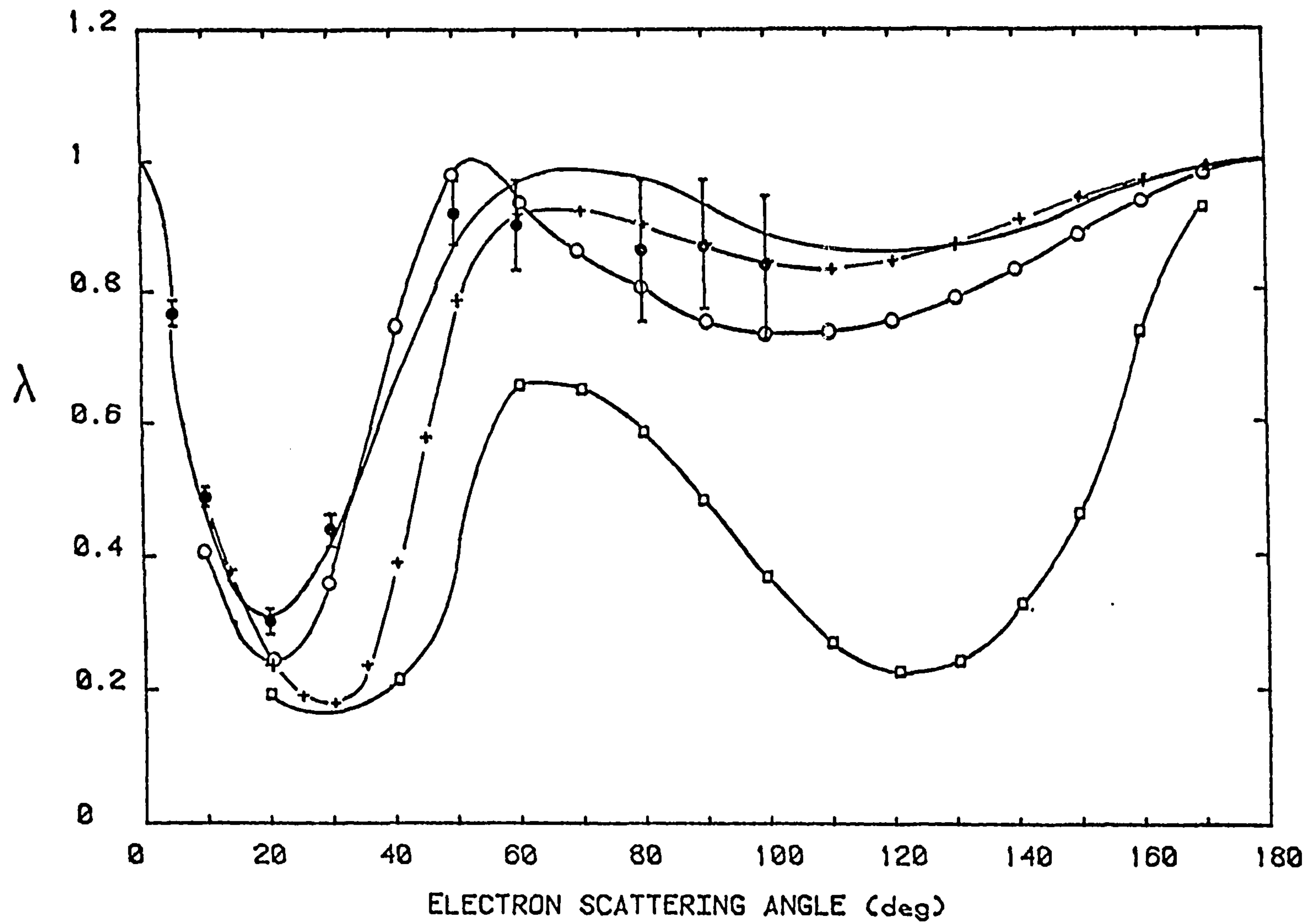

Fig. 21. Calculations of the variation of λ with electron scattering angle compared to the present data. ▬▬, calculation of Ref. 25 ; —+—, calculation of Ref. 30 ; —□—, calculation of Ref. 32 ; —o—, calculation of Ref. 31 .

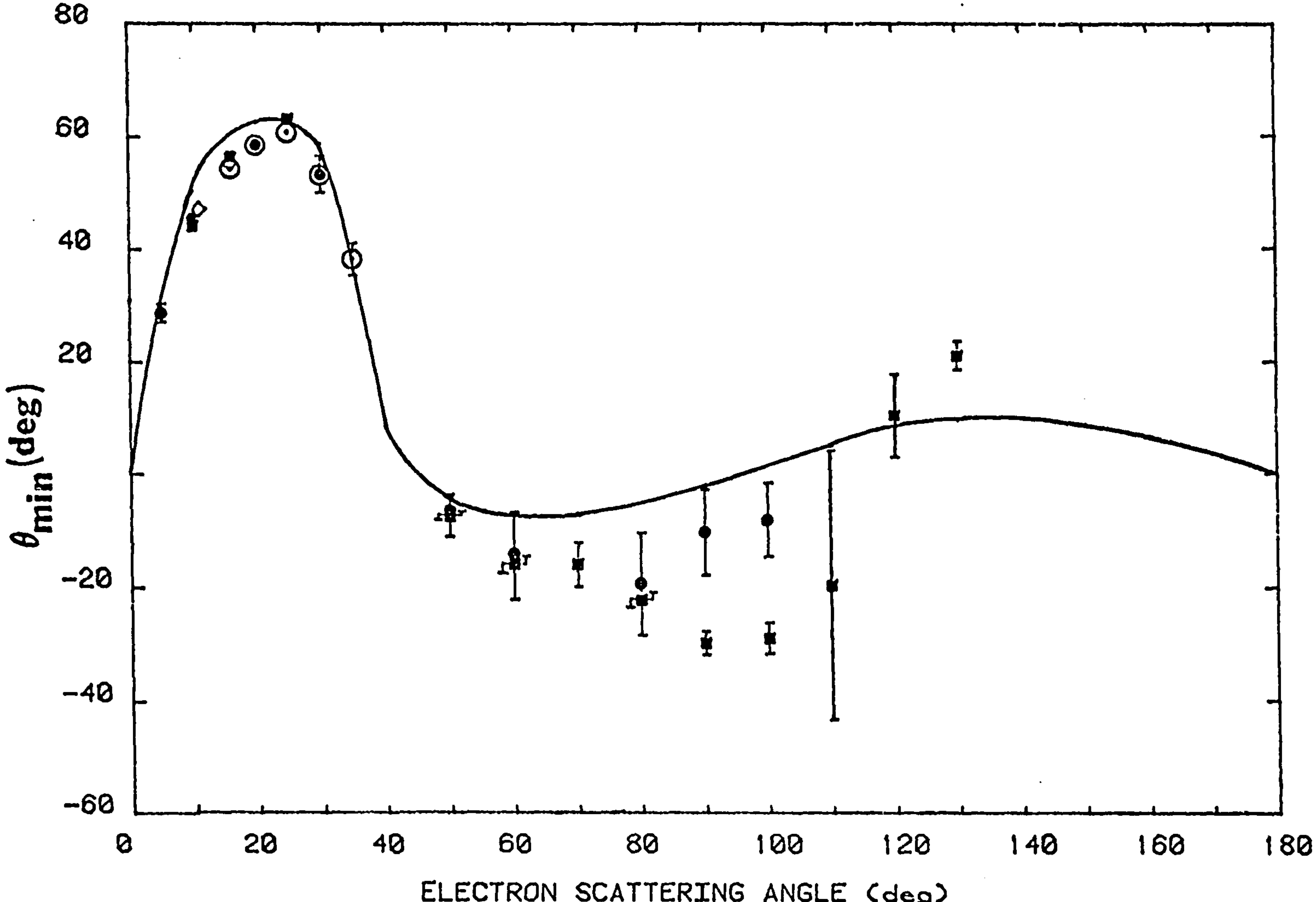

Fig. 22. Variation of θ_{min} with electron scattering angle. Full curve, calculation of Ref. 31.